Helical Instabilities in Magnetized Cylindrical Liner-Plasmas

by

David A. Yager-Elorriaga

A dissertation submitted in partial fulfillment
of the requirements for the degree of
Doctor of Philosophy
(Nuclear Engineering and Radiological Sciences)
in The University of Michigan
2017

Doctoral Committee:

Professor Ronald M. Gilgenbach, Co-Chair
Professor Yue Ying Lau, Co-Chair
Professor Brian E. Gilchrist
Matthew R. Gomez, Sandia National Laboratories
Assistant Research Scientist, Nicholas M. Jordan
Associate Professor Ryan D. McBride

David Alexander Yager-Elorriaga

dyager@umich.edu

ORCID iD: 0000-0001-6110-1700

ACKNOWLEDGEMENTS

Professor Gilgenbach has said two things that have particularly stuck with me throughout graduate school. The first, asked of me many times when designing the cylindrical liner system, was "*what about the sausage and kink instabilities?*" After almost two years, I finally have an answer: this thesis. The second was said to me as a prospective student during my visit to the University of Michigan, where Professor Gilgenbach told me that *his students always come first*. The depth of this statement really struck me after a particularly serious accident—Professor Gilgenbach put my health before anything else, gave me all of the time I needed to recover, and never once tried to rush my thesis during the long months that followed. Every meeting with him began with concern for my wellbeing, and concluded with me giving him my assurances that I would not push myself too hard. Of all of the exceptional qualities Professor Gilgenbach has as an advisor, it is this emphasis on his students' well-being that impressed me the most. Of course, I am also thankful for all of the science I learned from him; in particular, for his guidance on how to become an experimentalist and on how to write a journal article (start with the figures!). I would not be where I am today without the support of Professor Gilgenbach.

Professor YY Lau has also said and taught me a great many things that I will take with me as I move forward in my career; for these, I am profoundly grateful. The work in this thesis would not have had such a strong theoretical underpinning if it were not for Professor Lau and his insightful mind. I would especially like to thank Professor Lau for his deep concern for my health and wellbeing, for his relentless support, for our long and interesting conversations, and of course for our great memories at happy hour. I feel very lucky to have such good advisors.

I would also like to thank Professor Gilchrist, Dr. Matt Gomez from Sandia National Laboratories, Dr. Nick Jordan, and Professor Ryan McBride for joining my committee. I am especially thankful for Matt's help in obtaining the set of Helmholtz coils, without which none of the main conclusions in this thesis would have been possible. Our journal discussions were extremely helpful and gave me a broader picture of the HEDP and ICF fields. Anytime I needed advice or had a question, Matt always gave me thoughtful, informative responses. I was very lucky to have Matt on my committee, and I am looking forward to working with him at Sandia. I would also like to thank Nick for all of his advice throughout my time at Michigan. I often complicated the interpretations of various issues and phenomena that arose, and Nick would find a way to take things back to the basic principles, starting from what we know and what we do not know. Perhaps the most important lesson I learned from Nick was on how to how to give presentations (I had everything backwards). I am also thankful for all of Ryan's help. His experiences, insight, and advice have been invaluable to me. I hope to collaborate with him as we swap places between Sandia and Michigan.

Outside of my committee there are two people that have significantly contributed to the work in this thesis. Professor Peng Zhang and I hammered out the details of higher order *m* modes and spent hours interpreting the experimental results and discussing the best way to present them. Dr. Matt Weis also helped with interpreting my various experimental results, thoughtfully answered my *many* questions regarding the theoretical aspects of plasma instabilities, and helped me successfully run HYDRA.

Graduate school would not have been the same without Drs. Sonal Patel and Adam Steiner. Most of what I first learned about working in the lab was from Sonal and Adam, along with Dr. David Chalenski. Outside of the lab, our adventures have taken us all over Ann Arbor. These adventures include Dave Simon, Geoff Greening, Steve Exelby, Patrick Wong, and recently Paul Campbell, Drew Packard, Stephanie Miller, Abhi Jassem, and Foivos Antoulinakis. I am amazed at how, after spending all day working together in lab, we still chose to spend our lunch breaks, evenings, and

weekends together. I think this says something special about our advisors, Ann Arbor, and of course all of you.

I am particularly thankful for the many undergraduates and masters students (now some of them are graduate students themselves) that have helped me on various LTD projects over the years: Alex Rhodes, Andrew Denniston, Ashwin Rao, Cay Wagner, Daniel Nunez, Derek Hung, Drew Packard, Jeff Woolstrum, Jeremy Policht, Juan Riquezes, Julio Diaz, Karl Stimmel, Mackenzie Roman, Mike Hua, Ryan Leon, Stu Daudlin, Sunny Tummala, and Tanner Jones. The lab would have felt empty without you guys! I would also like to thank Mark Perrault for all of his help these past years—he has helped turn many of my ideas into reality.

Outside of our lab, I am indebted to the ABZ team at Sandia National Laboratories for lending our lab a set of Helmohltz coils, to Dr. Marty Marinak and Dr. Kyle Peterson for their help in obtaining HYDRA, and to Dr. Tom Awe for his advice on optical imaging systems. I am also grateful for my experiences with planar wire arrays and x-ray diagnostics during our collaboration with the University of Nevada-Reno group under Dr. Alla Safronova and Dr. Victor Kantsyrev, and for our fun summers with Dr. Mike Weller, Veronica Shlyaptseva, Dr. Ishor Shrestha, Chris Butcher, and Max Schmidt-Petersen.

Finally, I would like to give thanks to all of my family for their encouragement and support. I am truly lucky to have such amazing parents that support me in all of my endeavors, whatever they may be, and for introducing me to the world beyond our small town and encouraging me to travel it. I am also lucky to have such amazing little siblings for whom I am grateful for their support and for all our little rivalries and alliances throughout the years. I would also like to give a special thank you to “the cat” Pepino, who supported me by squeaking and chirping at the birds by the window for all of my thesis writing. Last but not least, I would like to thank the most important person in my life, my wife Kimberly Pflug, for her endless love and support, especially when I needed it the most, and for helping me figure out the truly important things in life.

None of the work here would have been possible without our sponsors. This research was supported by the DOE through award DE-SC0012328, Sandia National Laboratories contract DE-NA0003525, and the National Science Foundation. D.Y.E. was supported by an NSF fellowship under grant number DGE 1256260. The fast framing camera was supported by a DURIP, AFOSR Grant #FA9550-15-1-0419. Sandia is a multimission laboratory managed and operated by National Technology and Engineering Solutions of Sandia, LLC., a wholly owned subsidiary of Honeywell International, Inc., for the U.S. Department of Energy's National Nuclear Security Administration under contract DE-NA0003525.

TABLE OF CONTENTS

LIST OF FIGURES

LIST OF TABLES

LIST OF APPENDICES

ABSTRACT

A Z-pinch is formed by driving a large axial current through a cylindrical liner, generating an azimuthal magnetic field so that the resulting Lorentz force implodes the system to high energy density conditions. During the implosion process, the magneto-hydrodynamic (MHD) sausage and kink instabilities may couple to the acceleration-driven magneto Rayleigh-Taylor (MRT) instability. These instabilities are particularly relevant to magnetized target fusion schemes such as the magnetized liner inertial fusion (MagLIF) concept being pursued at Sandia National Laboratories, where a Z-pinch driver is used to generate thermonuclear conditions by imploding a magnetized and preheated fusion fuel within a cylindrical liner.

This thesis presents an experimental investigation of helical features that appear in magnetized, ultrathin foil-plasmas driven in a Z-pinch configuration by the 1-MA linear transformer driver at University of Michigan. Three types of cylindrical liner loads were designed to produce: (1) pure MHD modes (defined as being devoid of the acceleration-driven MRT instability) using a non-imploding geometry, (2) pure kink modes using a non-imploding, kink-seeded geometry, and (3) MRT-MHD coupled modes in an unseeded, imploding geometry. For each of these configurations, the effects of axial magnetic fields were determined using external Helmholtz coils that generated relatively small fields of B_z = 0.2-2.0 T (compared to peak azimuthal fields of 30-40 T). The resulting liner-plasmas and instabilities were imaged using 12-frame laser shadowgraphy and visible self-emission on a fast framing camera. A tracking algorithm was developed to trace self-emission minima in order to carefully identify the azimuthal mode number.

When no axial magnetic field was applied, the unseeded imploding and non-imploding liners were found to develop an azimuthally symmetric sausage instability. Applying an axial magnetic field excited helically oriented instabilities, which are

demonstrated to be a manifestation of discrete eigenmodes. The pitch angle of the helix is governed by the simple equation $\phi = m/kR$, from implosion to explosion, where m, k, and R are, respectively, the azimuthal mode number, axial wavenumber, and radius of the helical instability. Thus, the pitch angle increases (decreases) during implosion (explosion) as the plasma radius became smaller (larger). It was found that one (or at most two) discrete helical mode(s) developed for magnetized liners, with no apparent threshold on the applied B_z for the appearance of helical modes; increasing the axial magnetic field from zero to $B_z = 0.5$ T changed the relative weight between the $m = 0$ sausage and $m = 1$ kink modes. Further increasing the applied axial magnetic fields excited the higher order $m = 2$ helical mode, consisting of two intertwined helices. Finally, the importance of seeding when compared to the intrinsic instability modes was investigated using the kink-seeded support structure. It was found that the seeded kink instability overwhelmed the intrinsic instability modes of the plasma, despite the magnitude and orientation of the applied axial magnetic field. The experimental results in this thesis are corroborated with the Weis-Zhang-Lau analytic theory on the effects of radial acceleration on the classical sausage, kink, and higher m modes.

CHAPTER 1
INTRODUCTION

A fast Z-pinch is created by driving a large axial current through a cylindrical conductor, so that the self-generated Lorentz force implodes the system to create high energy density conditions. Z-pinches are particularly efficient at compressing matter; the external pressure that implodes the column (arising from the Lorentz force) increases inversely with the square of the radius during the implosion process. Z-pinch systems find applications in the production of x-ray and neutron radiation through gas puffs [SPI85, COV07], wire arrays [SPI88, SAN96, MAT 97, SAF16], and dense plasma foci [MAT65, SCH12], and in the production of thermonuclear fusion through magnetized target fusion schemes [KIR95, INT04, SLU10]. The x-rays produced from Z-pinches themselves find use in indirect drive inertial confinement fusion [CUN06], x-ray opacity measurements [BAI15], and fundamental atomic and astrophysics [BAI02, BAI03].

The high currents involved in Z-pinches typically result in a phase transition of the imploding matter to the plasma state. The large accelerations and inherent cylindrical geometry of Z-pinches render them unstable to a variety of instabilities characteristic to both acceleration-driven materials and current-driven plasmas. These include the magneto Rayleigh-Taylor instability of an accelerating interface [CUR60, HAR62, BUD90, SIN10, MCB12, ZIE12, WEI14, WZL15] and the traditional sausage and kink instabilities of a current-carrying plasma column [BEL06]. These instabilities proved disastrous for the early approaches to thermonuclear fusion in the 1950s, which used a Z-pinch configuration to compress and confine a fusion fuel inside of a linear discharge tube [BIS58]. External magnetic fields directed along the axis of the pinch were applied, which stabilized the axisymmetric instability modes such as the sausage instability; however, helical modes such as the kink instability remained unstable [BUR58]. A

similar phenomenon arises in the tokomak, where the kink mode remains a threat while the sausage mode is completely stable.

Modern approaches to fusion using magnetized target fusion schemes, such as the Magnetized Liner Inertial Fusion (MagLIF) program on the Z Machine at Sandia National Laboratories [SLU10, CUN12, MCB13, GOM14, GOM15], have demonstrated promising results by imploding and confining a fusion fuel inside of an initially solid cylindrical liner using a Z-pinch configuration. In MagLIF, the fusion fuel is laser pre-heated and axially pre-magnetized, and the liner is imploded with ~20 MA of current from the Z Machine. The laser preheat is required to raise the initial fuel temperature so that thermonuclear conditions may be achieved upon adiabatic compression of the fuel by the liner. The axial magnetic field is flux-compressed in the fuel during the implosion, so that upon stagnation it is sufficiently large to confine fusion generated alpha particles and limit thermal conduction losses to the liner walls. In 2014, Gomez et al. demonstrated that both the pre-heat and axial magnetic field are required for MagLIF; fuel temperatures as high as 3 keV and deuterium-deuterium thermonuclear fusion yields in excess of 10^{12} neutrons were obtained. Note that MagLIF is a hybrid between magnetic confinement fusion (MCF) and inertial confinement fusion (ICF). Thus, it might be subjected to instabilities common in MCF (e.g. kink-like) and instabilities in ICF (e.g. Rayleigh-Taylor). The experimental study of the coupling between these instabilities is the main motivation for this thesis.

Indeed, a main concern for MagLIF is the magneto Rayleigh-Taylor instability, which grows in the liner and feeds through to the fusion fuel [LAU11], limiting confinement and attainable gains. In 2012, studies of MRT by McBride et al. on the Z Machine at Sandia National Laboratories using unseeded, imploding cylindrical liners with no pre-applied axial magnetic field found instability structures that aligned themselves along roughly horizontal planes [MCB12, MCB13]. In this fashion, the interchange of the azimuthal magnetic field and plasma minimizes magnetic field line bending, favoring the axisymmetric structure. In 2013, these studies were repeated with the inclusion of a relatively weak axial magnetic field of 7 T by Awe et al., who found

multiple, intertwined helical structures develop in the liner that *opened up* (increased in pitch angle) as the liner imploded (see Figure 1.1), despite the puzzling fact that the external magnetic field lines tightly *wound up* (decreased in pitch angle) as the azimuthal magnetic field rapidly increased beyond 1000 T [AWE13, AWE14].

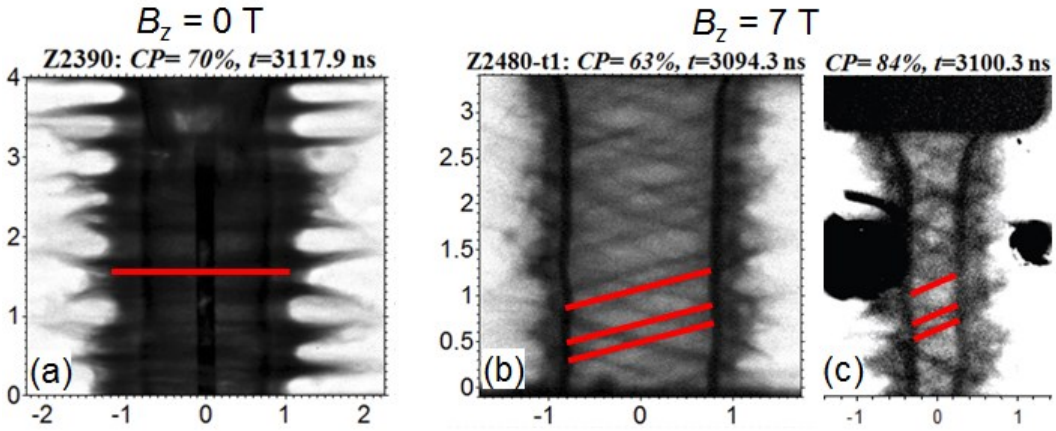

Figure 1.1. X-ray radiography of instability structures in imploding MagLIF liners. (a) Axisymmetric instability modes develop when no axial magnetic field is applied. (b) Helically oriented instability structures develop when an axial magnetic field of B_z = 7 T is applied. (c) The helical structures increase in pitch angle (open up) as the liner implodes. Images reproduced from Awe et al., *Physical Review Letters* **111**, 235005 (2013).

There is a striking resemblance in the origin and persistence of the helical structures observed in Awe's experiments [AWE13, AWE14], and the origin and persistence of spiral structures in disk galaxies. The latter gives rise to the well-known *winding dilemma* in astronomy [SHU82, COM87, BER14], a puzzle on the persistence of observed spiral structures in disk galaxies despite the strong differential rotation of stars and matter in the galaxy, analogous to the persistence of helical features in Awe's experiments despite the *winding up* of the external magnetic field during the implosion. The appearance of the spiral pattern in disk galaxies was quoted by Feynman [FEY64] as an outstanding problem, who also strongly suggested that it is a gravitational

phenomenon. The *winding dilemma* was resolved if one envisioned it as a wave phenomenon, the central theme in the Lin-Shu density wave theory [LIN64]. In this theory, density waves propagate through the background gas of the galaxy, stimulating the creation of stars that illuminate the bright spiral arms. The stars maintain a strong differential rotation about the galaxy axis but the density wave does not; therefore, the spirals do not *wind up* as time progresses. If the density wave has an azimuthal mode number m and a radial wavenumber k, the pitch angle of the spiral density wave at a radius R from the galaxy axis is then $\phi = \text{atan}\,(m/kR) \sim m/kR$ for $m << kR$, and this pitch angle persists despite the strong differential rotation of matter in disk galaxies. Discrete spiral modes of density waves were later found [LAU76, LAU78] and compared with observation [SHU82, BER14].

The resolution of the *winding dilemma* in disk galaxies via the use of discrete spiral modes motivated an interpretation of the helical features in Awe's experiments via the use of discrete *helical* modes. This was first proposed by Weis, Zhang, Lau et al. in 2015 [WZL15]. In this interpretation, the helical structures arise due to discrete, non-axisymmetric eigenmodes, and persist despite the rapid increase and dominance of the azimuthal magnetic field; they are thus very similar to the discrete spiral modes that were used to explain the persistence of spiral arms in disk galaxies. This thesis provides a systematic experimental study of discrete helical modes in magnetized liner-plasmas, both seeded and unseeded, imploding and non-imploding, and with and without an external axial magnetic field.

In order to investigate these helical structures, we used the 1-MA linear transformer driver at the University of Michigan. We first developed a technique to fabricate ultrathin liners with wall thicknesses of 400 nm [YAG15]; such an extremely thin liner permitted an appreciable acceleration and thus the sausage and helical modes could couple to the MRT instability. As a result, helical features similar to those observed in Awe et al. arose when a pre-imposed axial magnetic field was applied [AWE13, AWE14]. The nature of these helical features was investigated in detail in this thesis.

Experiments studying the physics of Z-pinch plasmas and associated plasma instabilities have been performed on university-scale pulsed power machines with peak current capabilities in the megaampere range [ZIE10, ZIE12, GOM10, BLE12, VAL14, SHL14, BUR15, ATO16]. These facilities have the advantages of a relatively low cost per shot and high repetition rate compared to large-scale experiments such those performed on the Z Machine at Sandia National Laboratories, allowing for increased flexibility in designing and performing physics experiments. However, metallic liner-plasma implosions are difficult to study on small-scale experiments because the maximum attainable current is often insufficient to implode initially solid liners of reasonable geometry. These experiments typically focus on imploding wire arrays or the physics of non-imploding liners, such as the initiation of plasma and instabilities on the liner surface or the precursor plasma formed inside of the liner. To achieve an implosion with a relatively low current of ~1 MA (compared to ~20 MA on the Z Machine), a liner with sub-micron thickness is required, and this enabling technique becomes a key contributor to this thesis research [YAG15].

In Chapter 2, the theoretical background of magneto hydrodynamic (MHD) and acceleration-driven (MRT) instabilities is presented. The coupling of the MHD modes (such as the sausage and kink instabilities) to MRT is discussed. The three-region, sharp boundary, ideal MHD analytic model developed by Weis, Zhang, Lau et al. is presented. This model, together with equilibrium profiles from 1-D HYDRA simulations [MAR01, KON09] is used to analytically calculate instability growth rates for a cylindrical liner-plasma with arbitrary acceleration and axial magnetic field. It is then used extensively to interpret the experimental results of this thesis.

In Chapter 3, the experimental configuration is presented, including an overview of the 1-MA Linear Transformer Driver at the University of Michigan and its suite of diagnostics, including a 12-frame shadowgraphy and self-emission imaging system. In the second section of this chapter, the incorporation of two Helmholtz-like coils that are used to axially pre-magnetize the thin-foil liner loads is presented.

In Chapter 4, non-imploding liners using ultrathin aluminum foils were experimentally investigated [YAG16a]. By minimizing the acceleration of the liner, pure sausage and helical instabilities (defined as being devoid of MRT) were investigated. These experiments were configured in an unseeded (Section 4.1) or a kink-seeded (Section 4.2) geometry, and the modes were identified by carefully connecting the self-emission features on the face of the liners to the instability bumps that were observed on the edges of the liner. For the unseeded geometry, it was found that, with no applied axial magnetic field, an azimuthally symmetric sausage instability developed. When an axial magnetic field was applied, a higher order helical mode developed, consisting of two intertwined helical structures. These helical structures spiraled in the same sense of rotation as the global magnetic field. For the kink-seeded geometry, it was found that the seeding dominated the intrinsic instability modes that arose in Section 4.1, despite the orientation of the applied axial magnetic field. In other words, once the helical mode was seeded, it persisted throughout the discharge.

In Chapter 5, the liners were allowed to implode by modifying the liner support structure. Appreciable accelerations were obtained, enabling the sausage and helical modes of Chapter 4 to couple to the acceleration-driven MRT instability. It was found that the pitch angle of the helical instabilities increased during the implosion phase and decreased during the subsequent explosion stage (after the liner has stagnated and rebounded from the central support structure). These helical striations are interpreted as discrete, non-axisymmetric eigenmodes that persist from implosion to explosion *despite the winding up of the external magnetic field*. Their helical pitch angle obeys the simple relation $\phi = m/kR$, for $m << kR$, where m, k, and R are the azimuthal mode number, axial wavenumber, and radius, respectively [YAG16b]. These results are consistent with Awe's helices, which were observed to increase in helical pitch angle during the implosion of the liner as a discrete helical eigenmode [WZL15]. Here, we add new insights to the nature of helical modes, outlined as follows [YAG16b]. We found that: (a) there is only one, or at the most two, dominant unstable eigenmodes for the axial magnetic field values tested (0.2 – 2.0 T), (b) there does not appear to be a sharp

threshold on the axial magnetic field for the emergence of the non-axisymmetric helical modes, and (c) higher axial magnetic fields yield higher azimuthal modes.

Finally, in Chapter 6, the conclusions of this work and suggestions for future research are presented and discussed.

CHAPTER 2
THEORETICAL BACKGROUND

Z-pinches are a particularly simple plasma confinement configuration. A current is driven through a cylindrical plasma column, generating an azimuthal magnetic field. The resulting self-generated Lorentz force is directed radially inward, and may be used to implode or confine the plasma. An equivalent description of the Lorentz force is attained through the concept of magnetic pressure, where $P_{mag} = B^2/2\mu_0$, where B is the magnetic field and μ_0 is the permeability of free space. For a conducting plasma, the magnetic pressure behaves similarly to kinetic pressure and is useful for understanding the dynamics and stability of a Z-pinch plasma.

When the external magnetic pressure is equal to the total internal pressure in a plasma column, a radial equilibrium will result, as shown in Figure 2.1(a-b). This equilibrium is unstable to perturbations in the plasma-vacuum interface. For the sausage instability shown in Figure 2.1(a), the plasma boundary is displaced radially inward by an azimuthally symmetric perturbation from the equilibrium. The current flowing in the system is unchanged; due to the decrease in radius, however, the magnetic field and associated magnetic pressure have now increased and will exceed the internal plasma pressure (assumed to be unchanged during the perturbation). The perturbed plasma boundary will therefore be driven further radially inward and a feedback process results which enhances the perturbation. Therefore, the system is unstable to azimuthally symmetric perturbations, which will continue to develop until confinement is lost.

For the kink instability in Figure 2.1(b), the plasma is perturbed from its equilibrium position by a small helical bend or kink. The magnetic pressure on the right side of the plasma boundary increases due to the crowding of magnetic field lines, whereas the magnetic pressure on the left side of the plasma boundary decreases due to

the spreading out of magnetic field lines. Subsequently, a net pressure arises across the plasma column which will drive the plasma further away from the equilibrium. Thus, the system is unstable to kink or helical perturbations.

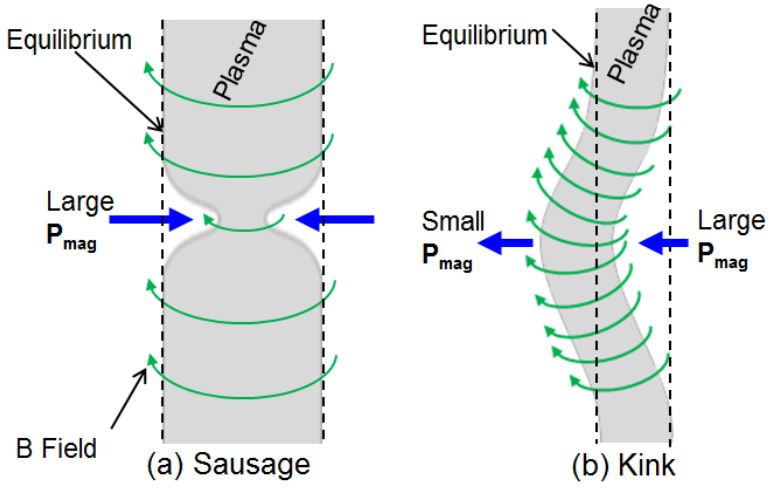

Figure 2.1. Traditional (a) sausage and (b) kink instabilities. The plasma is perturbed from its equilibrium state, resulting in an increased magnetic pressure which enables the sausage or kink structure to continue developing.

The sausage and kink instabilities may be described by wavelike perturbations in cylindrical geometry with amplitude $A \sim \exp(i\omega t + im\theta - i2\pi z/\lambda)$, where m is the azimuthal mode number and $\lambda = 2\pi/k$ is the axial wavelength of the instability (k is the axial wavenumber). These perturbations result in the following dispersion relation for a plasma column with a constant density [WEI15],

$$\omega^2 = \frac{k^2 B_z^2}{\mu_0 \rho} + \frac{(\boldsymbol{k}\cdot\boldsymbol{B})^2}{\mu_0 \rho} b_1 - \left(\frac{k^2 B_\theta^2}{\mu_0 \rho\,(kR)}\right) b_2, \tag{2.1}$$

where $\boldsymbol{k} = k\hat{\boldsymbol{z}} - (m/R)\hat{\boldsymbol{\theta}}$ is the instability wavevector and the b-terms are real and positive, given by

$$b_1 = \left(\frac{I_m'(kR)}{I_m(kR)}\right),\ b_2 = b_1 \times \left(-\frac{K_m(kR)}{K_m'(kR)}\right). \tag{2.2}$$

In Equations (2.1) and (2.2), $\boldsymbol{B}$ is the total magnetic field vector, B_z and B_θ are magnetic field components in the axial and azimuthal directions, respectively, ρ is the mass density of the plasma, R is the equilibrium radius, μ_0 is the vacuum permeability, m is the azimuthal mode number, and I_m and K_m are the modified Bessel functions of order m of the first and second kind, respectively (the prime denotes differentiation with respect to the argument). When ω^2 is negative, an imaginary value for ω results, which may be expressed as $\omega = \pm i\gamma$. Here, γ is real-valued and positive, and is defined as the growth rate of the instability; the amplitude of perturbations will grow exponentially in time following $A \sim \exp(\gamma t)$. When $m = 0$, Equation (2.1) describes the growth rate for the azimuthally symmetric sausage instability. When $|m| = 1$, Equation (2.1) describes the growth rate for the helical kink instability. When $|m| > 1$, Equation (2.1) describes the growth rate for multiple intertwined helical perturbations (see Section 2.1).

Equation (2.1) has three terms. The first two terms are stabilizing terms due to the magnetic tension of the azimuthal and axial magnetic field lines. The $(\boldsymbol{k} \cdot \boldsymbol{B})^2$ term may be expanded to obtain

$$(\boldsymbol{k} \cdot \boldsymbol{B})^2 = (kB_z - (m/R)B_\theta)^2, \tag{2.3}$$

From this equation, we see that the axial magnetic field tends to reduce the overall growth rate[1] and that the azimuthal magnetic field tends to be stabilizing for higher order azimuthal mode numbers[2] (e.g. modes with $m > 0$). The third term is the driving term for the instability and arises solely due to the azimuthal magnetic field (i.e., to the axial current). It is scaled to the Alfven speed, $V_A = (B_\theta^2/\mu_0\rho)^{1/2}$, and is inversely proportional to the plasma radius—for a given current, a smaller radius increases the growth rate both directly and indirectly by increasing B_θ, which scales as ~$1/R$. It is important to note that the last term of Equation (2.1) vanishes as $R \to \infty$ (fixing B_θ). Thus, there is no current-driven instability (and therefore no sausage and helical instabilities) in the planar geometry of a stationary plasma. This is a well-known result in

[1] The exception arises when $\boldsymbol{k} \cdot \boldsymbol{B} = 0$, in which case the second term of Equation (2.1) vanishes.
[2] Similarly, when $\boldsymbol{k} \cdot \boldsymbol{B} = 0$, the second term of Equation (2.1) vanishes despite the value of m and B_θ.

ideal magneto-hydrodynamics (see, e.g. [LAU11]). Also, note the overall dependency of growth rate on density, which scales as $\gamma \sim 1/\rho^{1/2}$, indicating that the instabilities that develop in plasmas will typically have a much larger growth rate when compared to those in a solid liner or rod.

When the external magnetic pressure exceeds the total internal pressure in a plasma column, the plasma will radially implode, pinching along the **z** axis. The resulting acceleration is directed radially inward and is equivalent to an effective gravity in the plasma frame that is directed radially outward. In the frame of the plasma, this scenario corresponds to a heavy fluid (plasma) suspended above a light fluid (magnetic field, or possibly a lower density plasma) and is therefore unstable to the magneto Rayleigh-Taylor instability (MRT), as shown in Figure 2.2. For this instability, wavelike perturbations continue to develop as the heavy fluid descends in the effective gravitational field, reducing the potential energy of the system. The magnetic field provides a stabilizing tension, depending on its orientation when compared to the wavevector of the instability perturbations. This is best understood by examining the MRT growth rate for planar geometry [HAR62, RYU00, LAU11, WEI14],

$$\gamma^2 = kg - (\boldsymbol{k} \cdot \boldsymbol{B})^2/\mu_0\rho, \tag{2.4}$$

where g is the effective gravity the plasma-vacuum interface experiences, and is equal in magnitude (but opposite in direction) to the acceleration in the laboratory frame. The maximum stabilization arises when the magnetic field is oriented parallel to the perturbation wavevector, as shown in Equation (2.4). For a sufficiently large magnetic tension, the MRT growth rate will be imaginary and therefore completely stabilized. The perturbations will then oscillate, following the dependency $A \sim \exp(i\gamma_R t)$, where γ_R is the absolute magnitude of γ in Equation (2.4). Note when $g = 0$, this scenario is equivalent to the dispersion relation for Alfven waves, which arise from the magnetic tension aspect of magnetic field lines in plasmas.

It is important to note that, in general, the most unstable mode is one that satisfies $\boldsymbol{k} \cdot \boldsymbol{B} = 0$, either from Equation (2.1) or Equation (2.4). Thus, there is the general notion

that the most unstable helical mode that should develop is the one in which the mode pattern is aligned with the external magnetic field. This notion is apparently inconsistent with Awe's seminal experiments [AWE13, AWE14], whose resolution is one of the main purposes of this thesis [YAG16a, YAG16b].

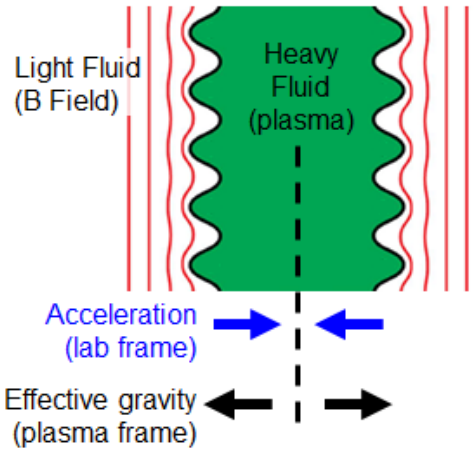

Figure 2.2. Magneto Rayleigh-Taylor instability in an imploding cylindrical plasma. The plasma and magnetic field are analogous to the heavy and light fluids in the classical Rayleigh-Taylor instability. An acceleration vector directed radially inward in the laboratory frame is equivalent to an effective gravity directed outward in the moving frame of the plasma-vacuum interface. An axial magnetic field provides a stabilizing tension for the axisymmetric mode, as its field line is bent.

2.1 Instability Mode Descriptions

The physical picture of sausage and helical modes may be understood from their perturbations, which take the form $\exp(im\theta - i2\pi z/\lambda)$, where m is the azimuthal mode number (which may be positive, negative, or zero), and λ is the axial wavelength of the instability. In this description, we take the axial wavevector $k = 2\pi/\lambda$ to be always positive. The axisymmetric $m = 0$ mode and the helically oriented $|m| = 1$ mode are commonly referred to as the sausage and kink instabilities, respectively. For the $|m| = 1$ mode, an azimuthal variation of 2π traces a constant perturbation a distance of one axial wavelength, resulting in a single helical structure. For $|m| > 1$, an azimuthal variation of 2π traces a constant perturbation a distance of $|m|$ axial wavelengths, resulting in a structure consisting of $|m|$ intertwined helices. In this thesis, all $|m| \geq 1$ modes are collectively referred to as helical modes, with the following sign convention for m. A helix is assigned a positive (negative) azimuthal mode number $+m$ ($-m$) if this helix is in the same (opposite) sense of rotation as the global magnetic field, which has a nonzero axial magnetic field B_z in addition to azimuthal magnetic field B_θ. The sense of rotation is determined as follows. The spirals of the plasma helices and global magnetic field have an azimuthal component (which may be clockwise or counterclockwise) and an axial component (which may be up or down). The azimuthal component of the plasma helix is ambiguous and therefore assigned the same direction of the global magnetic field. Then, if the axial components are parallel (anti-parallel), the plasma helix and magnetic field have the same (opposite) sense of rotation and thus the sign of the mode is positive (negative). Note that for the positive m mode, the plasma helix need not be perfectly aligned with the global magnetic field; however, it must have the same sense of rotation as the global magnetic field. A helical mode with no sign attached to the azimuthal mode number (m) is used to indicate that there is no axial magnetic field.

In this convention, the $-m$ modes tend to be more stable than the $+m$ modes, because the former have a higher degree of magnetic field line bending (i.e., $(\boldsymbol{k} \cdot \boldsymbol{B})^2$ has a larger value), a well-known stabilizing influence for MHD modes. Figure 2.3 shows physical representation of the $m = 0$, $m = \pm 1$, and $m = +2$ modes. *In short, the positive*

sign is used when the terms kB_z and mB_θ/R are of the same sign, while the negative sign is used if they are of the opposite sign (see Equation (2.3)). Note the signs of k and m in the terms kB_z and mB_θ/R dictate the direction of the plasma helix spiral, while the signs of B_z and B_θ dictate the direction of the global magnetic field spiral [YAG16a].

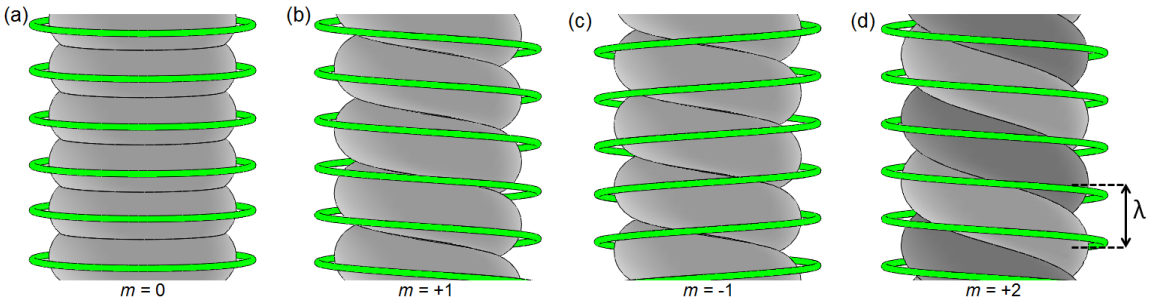

Figure 2.3. Physical picture of instability structures with azimuthal mode number (a) $m = 0$, (b) $m = +1$, (c) $m = -1$, and (d) $m = +2$. Also shown is the axial wavelength λ, defined as the distance between adjacent instability structures. The global magnetic field is represented by the thin green line. A positive m (negative m) mode indicates the plasma helix rotates in the same (opposite) sense as the global magnetic field. The $m = +1$ and the $m = -1$ mode consist of a single helix, whereas the $m = +2$ mode consists of two intertwined helices (shown as dark and light gray in (d)). Note that in (d), when the light (or dark) helix traces an azimuthal angle of 2π, the axial distance advances by 2λ.

2.2 Discrete Helical Modes

Consider a discrete helical mode of the form $\exp(i\omega t + im\theta - ikz)$ that has developed in the plasma, which undergoes an implosion and subsequent explosion, such as the $|m| = 2$ helical mode in Figure 2.4. If the helical mode persists during this process (with an approximately constant wavevector, k), then the helical pitch angle ϕ will dynamically vary, increasing in angle during the implosion process (as the plasma radius decreases) and decreasing in angle during the explosion process (as the plasma radius increases). The striation angle is then solely a function of the plasma radius and wavelength, and is determined as follows. For $|m| > 1$, an azimuthal variation of 2π traces a helical striation a distance of $|m|$ axial wavelengths. Thus a total distance of $l = 2\pi R$ is traced in the **r-θ** plane (corresponding to a single circumference) while a distance of $h = m\lambda$ is traced axially. The 3-D helical pitch angle is therefore given by the following equation

$$\phi = \arctan[m\lambda/2\pi R] = \arctan[m/kR] \sim m/kR, \tag{2.5}$$

where m is the azimuthal mode number, k is the instability wavevector ($k = 2\pi/\lambda$) and R is the plasma radius. The approximation in the last term of Equation (2.5) assumes $|m| \ll kR$, a condition usually satisfied. The projected 2-D striation angle in the Cartesian **y-z** plane is similarly determined. For an azimuthal variation of π, the net distance traced horizontally (in the **y** direction) is given by $l = 2R$ (corresponding to the diameter) while the net distanced traced vertically (in the **z** direction) is $h = m\lambda/2$. Thus the 2-D striation angle (shown in Figure 2.4) is given by

$$\phi_{2D} = \arctan[m\lambda/4R] \sim m\pi/2kR. \tag{2.6}$$

Therefore, the 3-D striation angle may be obtained by multiplying the 2-D striation angle by a factor of $2/\pi$ [ATO16]. This factor is useful for measuring 3-D helical self-emission striations from their 2-D projection onto an imaging device.

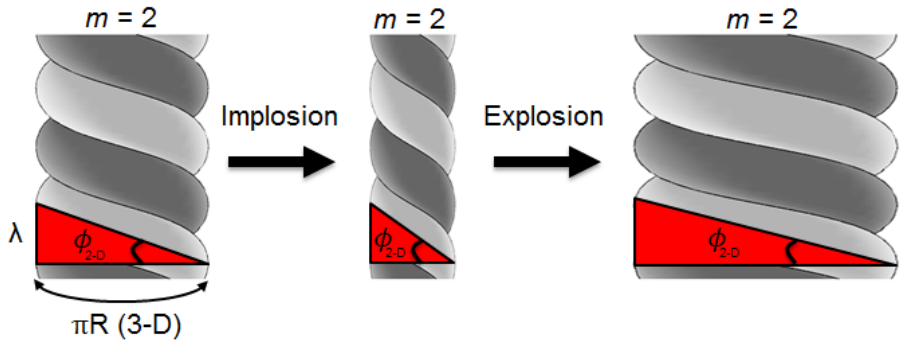

Figure 2.4. Discrete $|m| = 2$ helical mode undergoing an implosion and subsequent explosion. The 3-D striation angle varies dynamically according to $\phi = m/kR$, where m is the azimuthal mode number, k is the axial wavevector, and R is the radius of the plasma at which the helical mode is formed. The 2-D striation angle in the figure is the projection of the 3-D helical structure onto the 2-D Cartesian **y**-**z** plane.

2.3 Weis-Zhang-Lau Instability Growth Rate Theory

In an accelerating cylindrical liner, sausage and helical modes may couple to the magneto Rayleigh-Taylor instability when the liner undergoes radial acceleration. The general dispersion relation for this scenario was calculated analytically by Weis, Zhang, Lau et al. for an arbitrary axial magnetic field using linear perturbation theory, ideal MHD, and a three region sharp boundary model [WZL15]. While the majority of the experimental data in this thesis was taken at a time when the instabilities have grossly developed (likely beyond the direct applicability of perturbation theory), the Weis-Zhang-Lau (WZL) theory may still be used to: (1) understand instability development that has occurred earlier in time when the instability amplitudes were small, and, in particular, to (2) determine the effects of axial magnetic fields on the various *m*-modes [WZL15, WEI15].

An overview of the three region model is shown in Figure 2.5. Sharp boundaries separate Regions I, II and III, which describe the regions outside of the liner, the liner, and inside of the liner, respectively. Each region has an associated axial magnetic field and density; however, for the following equations it is assumed the axial field is constant in each of the three regions, and that the density of the liner in Region II far exceeds the density of any plasma in Regions I and III. The azimuthal field is restricted to Region I only.

2.3.1 Instability Coupling

The coupling of the sausage and helical modes to the MRT instability may be defined using the equilibrium condition for the liner, given by the following equation,

$$g\rho_{02}\Delta = \left[P_I + \frac{B_z^2+B_\theta^2}{2\mu_0}\right]_{\mathrm{I}} - \left[P_{III} + \frac{B_z^2}{2\mu_0}\right]_{\mathrm{III}}, \tag{2.7}$$

where g is the effective gravity experienced by the liner, ρ_{02} is the liner density, Δ is the liner thickness, and P_I and P_{III} are the kinetic pressure in Regions I and III. The first term in brackets on the right side of the equation represents the net pressure just outside of the liner ($\boldsymbol{P_{outside}}$ in Figure 2.5), the second term in brackets represents the net pressure on the

inside of the liner ($\boldsymbol{P_{inside}}$ in Figure 2.5). Using this equation, we may define instability coupling:

- Pure MRT mode: $|g|$ is maximized, $\boldsymbol{P_{inside}} = 0$ (implosion)
- Pure MRT mode: $|g|$ is maximized, $\boldsymbol{P_{outside}} = 0$ (stagnation and explosion)
- Pure sausage/helical mode: $g = 0$, $\boldsymbol{P_{outside}} = \boldsymbol{P_{inside}}$
- Coupled ($g > 0$): $0 < \boldsymbol{P_{inside}} < \boldsymbol{P_{outside}}$ (implosion)
- Coupled ($g < 0$): $0 < \boldsymbol{P_{outside}} < \boldsymbol{P_{inside}}$ (stagnation and explosion)

The two cases for pure MRT and coupled modes are explicitly listed because of their unique characteristics. When $g > 0$, the outer interface of the liner is MRT unstable while the inner interface is MRT stable; however, instability ripples may feed-through to the inner surface [LAU11, WZL15]. When $g < 0$, which typically occurs during stagnation and the subsequent explosion, the inner surface of the liner is now unstable to the MRT instability. During a strong deceleration, $|g|$ may be very large and cause the inner surface of the liner to become extremely unstable. This scenario is particularly relevant to MagLIF liners [WEI15, WZL15]. The outer interface of the liner is now MRT stable but remains unstable to the sausage and helical modes. The effect of the negative gravity is to reduce the overall instability growth rate on the outer interface. If $|g|$ is sufficiently large, then the outer interface may even become stable to the sausage and helical modes, and thus perturbations will oscillate. A similar effect was observed in simulations of the imploding stage of a MagLIF liner, where small ripples oscillated on the MRT-stable *inner* surface of the liner due to the effects of a positive gravity [WEI15].

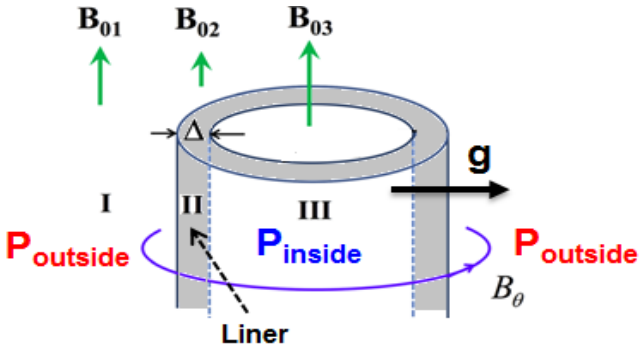

Figure 2.5. Three region sharp boundary model of an accelerating liner with arbitrary axial magnetic field used to define instability coupling and calculate analytic growth rates for MRT-coupled sausage and helical modes. The effective gravity g is determined by the total pressure difference between Region I ($\mathbf{P_{outside}}$) and III ($\mathbf{P_{inside}}$).

2.4 Weis-Zhang-Lau Dispersion Relation

The Weis-Zhang-Lau (WZL) dispersion relation is used in Chapter 4 and Chapter 5 to calculate instability growth rates using parameters from the experiments. The dispersion relationship for perturbations of the form exp(*iωt+imθ-ikz*) is given by the following equations [WZL15],

$$A\omega^4 - B\omega^2 + C = 0, \tag{2.8}$$

$$A = (X_1X_2 + 1)/(X_3^2k^2aR), \tag{2.9}$$

$$B = b_1 + b_2, \tag{2.10}$$

$$C = k^2V_{02}^2(k^2V_{02}^2A + b_2) + k^2V_{03}^2\left(\frac{I_{|m|}}{I'_{|m|}}\right)\left(-\frac{k^2V_{02}^2X_2}{X_3} + |k|g'\right) + k^2gg'. \tag{2.11}$$

In Equations (2.8) – (2.11), *a* and *R* are the liner's inner and outer radius, respectively, $k = 2\pi/\lambda$ is the perturbation wave number for axial wavelength λ, ρ_0 is the liner density and $V_{02,03} = (B_z^2/\mu_0\rho_0)^{1/2}$ is the Alfven speed contribution from the axial field in Regions II and III, respectively. The *X* terms are given by the following equations,

$$X_1 = K_{|m|}\hat{I}'_{|m|} - I_{|m|}\widehat{K}'_{|m|}, \tag{2.12}$$
$$X_2 = \hat{I}_{|m|}K'_{|m|} - \widehat{K}_{|m|}I'_{|m|}, \tag{2.13}$$
$$X_3 = \hat{I}'_{|m|}K'_{|m|} - \widehat{K}'_{|m|}I'_{|m|}. \tag{2.14}$$

The *b* terms are given by the following equations,

$$b_1 = 2k^2V_0^2A, \tag{2.15}$$
$$b_2 = -[(X_1/X_2)|k|g' + (X_2/X_3)|k|g]. \tag{2.16}$$

Finally, the g' term is given by the following equation

$$g' = g + (1/\mu_0\rho_0R)[B_\theta^2 + (\widehat{K}_{|m|}/\widehat{K}'_{|m|}|k|R)(-mB_\theta + kRB_z)^2], \tag{2.17}$$

where $I_{|m|} = I_{|m|}(|k|a)$, $\hat{I}_{|m|} = I_{|m|}(|k|R)$, $K_{|m|} = K_{|m|}(|k|a)$, and $\widehat{K}_{|m|} = K_{|m|}(|k|R)$.

For these equations, I_m and K_m are, respectively, the modified Bessel functions of order m of the first and second kind, where a prime denotes differentiation with respect to their arguments. The effective gravity in the liner frame is g, so that the liner acceleration in the laboratory frame is $-g$ and thus in the *opposite* direction of the liner acceleration. The growth rate is taken as the most unstable mode with the largest negative imaginary part of the four eigenvalues of ω in the dispersion relation (Equation (2.8)). When the liners demonstrate an approximately constant velocity expansion, g may be set to zero and the dispersion relationship reduces to the pure sausage and helical modes for a cylindrical liner of finite thickness.

The instantaneous equilibrium profile will be inferred from the 1D HYDRA code [MAR01, KON09] and will be used in the dispersion relation, Equation (2.8), as was similarly done in [WEI14, WEI15, WZL15].

CHAPTER 3
EXPERIMENTAL CONFIGURATION

The experiments were performed on the Michigan Accelerator for Inductive Z-Pinch Experiments (MAIZE), a Linear Transformer Driver (LTD) at the University of Michigan. MAIZE is capable of delivering 1-MA of current into a matched load at ±100 kV charge [GIL09, KIM09, MAZ10]. For the inductive liner loads utilized for the work in this thesis, the charge was limited to ±70 kV in order to reduce voltage on the capacitors and insulator, resulting in peak currents ranging from 500-600 kA. A cross-section of the LTD is shown in Figure 3.1, which includes the energy storage, transmission lines, and load hardware. The basic component of the LTD is known as a *brick*, which consist of a capacitor-switch-capacitor connected in series, as shown in Figure 3.2. The MAIZE LTD consists of 40 bricks arranged in an annulus and connected in parallel. The power from the bricks is delivered to the load hardware (discussed in Section 3.1.1) using a coaxial-to-radial-to-triplate transmission line. Two ferromagnetic cores are situated between the bricks and the coaxial transmission line, and are essential components of an LTD, creating a high impedance path around the outer casing of the conducting capacitor housing. As this path is connected electrically in parallel to the load, the high impedance of the cores is necessary to direct the majority of the current to the load and not around the LTD casing. This design allows for extremely compact, scalable pulsed power machines, where multiple LTD cavities may be arranged in series and parallel, increasing the overall power of the device. This concept has motivated the design of a petawatt-class pulsed power machine using LTDs as the basic component [STY07, STY15].

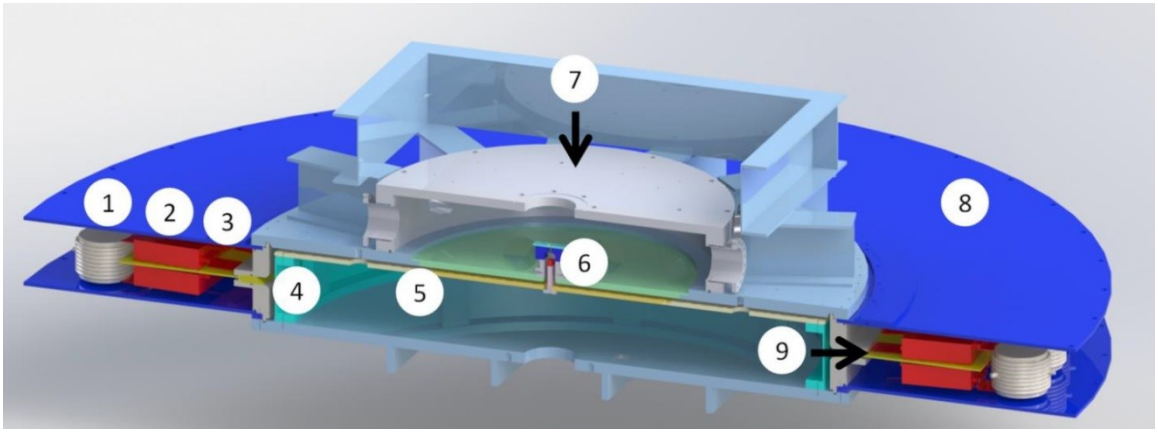

Figure 3.1. MAIZE Linear Transformer Driver, showing: (1) spark gap switch, (2) 40 nF capacitor, (3) iron core region (core not pictured), (4) coaxial transmission line section, (5) radial transmission line, (6) load region, (7) vacuum chamber, (8) oil chamber, and (9) high voltage insulator. The conducting outer ring (not pictured) connects the top and bottom blue plates in order to completely enclose the oil chamber.

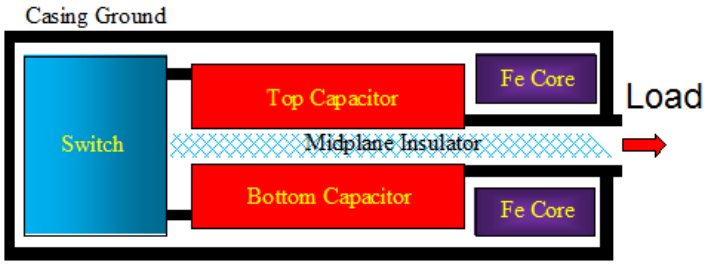

Figure 3.2. Linear transformer driver *brick*, consisting of two capacitors and one switch. The two iron cores create an inductive path around the casing and direct the majority of the current to the load. The MAIZE LTD consists of 40 bricks arranged in parallel. Image reproduced from [ZIE10].

3.1 Experimental Hardware

3.1.1 Load Hardware

Two types of load hardware were designed and are shown in Figure 3.3. Both designs are similar, consisting of a transmission line that is connected directly to the triplate and delivers power to the liner load. The transmission line and load hardware are located in a 1-m-diameter vacuum chamber. The liner loads consist of a 400 nm thick aluminum foil cut into a rectangular shape and wrapped around a dielectric support structure, which may be modified to investigate non-imploding, kink-seeded, or imploding plasmas. The liner loads are discussed in Section 3.1.2, below. The original load transmission line design is shown in Figure 3.3(a) and consists of two 4 cm wide return current plates. The large width significantly reduces the current density in the return current plates and therefore their contribution to the global magnetic field at the load region. This hardware was designed to demonstrate the feasibility of imploding an initially solid cylindrical liner using a sub-megaampere current pulse. The upgraded design is shown in Figure 3.3(b) and consists of a coaxial transmission line, where the liner load is connected to the inner coaxial conductor. The coaxial hardware was designed to enable the use of two Helmholtz-like coils, which slide around the outer coaxial conductor, as shown in Figure 3.4, and are capable of generating an axial magnetic field of up to 5.5 T for our system. The axial magnetization system is described in detail in Section 3.3 and Appendix A. The triplate system is connected to the coaxial transmission line using three adaptors, fabricated from aluminum. The effects of aluminum adaptors, when compared to stainless, were investigated using the ANSYS Maxwell model described in Section 3.3.2, and were found to negligibly perturb the axial magnetic field in the liner region.

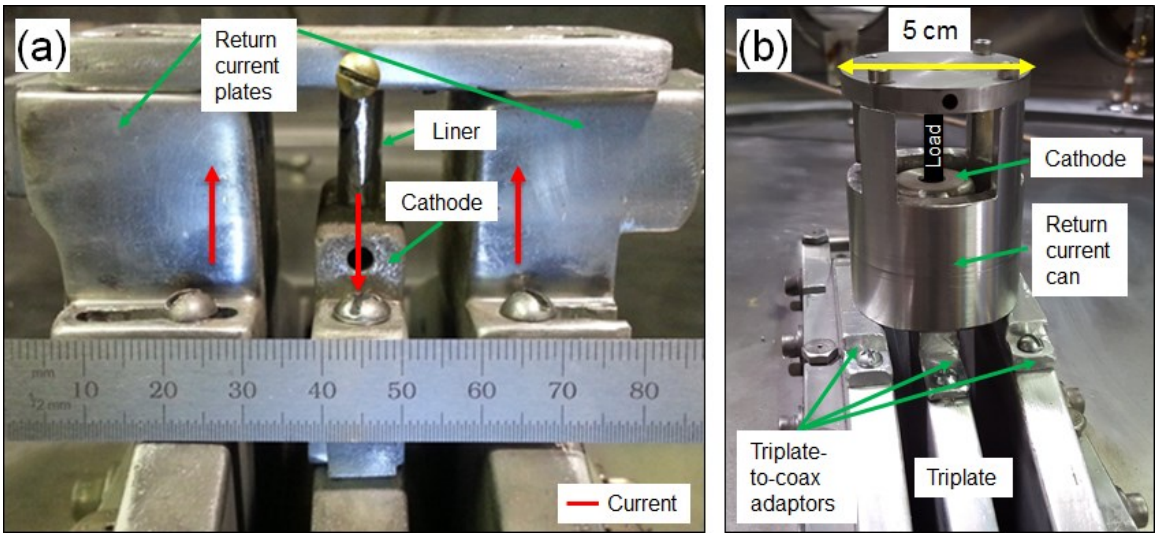

Figure 3.3. (a) Original load hardware. The liner load is situated between two return current plates, and is fixed to the anode and slides into the cathode during vacuum pumpdown. (b) Upgraded load hardware for use in magnetized liner experiments. The Helmholtz coils and housing slide around the coaxial transmission line.

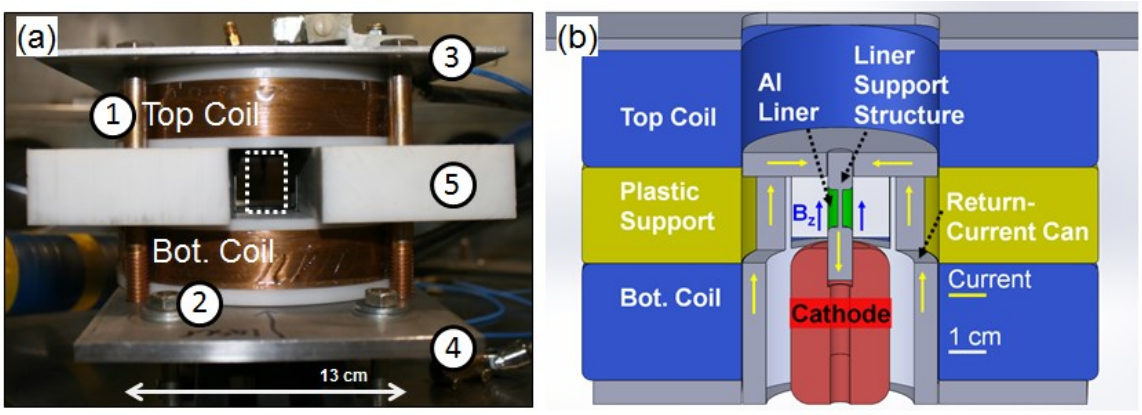

Figure 3.4. Coil hardware. In (a), four 3/8 in. bolts (#1) connect plate #3 to plate #4, holding the coils in place. Four 1/4 in. bolts (#2) connect plate 4 (and therefore the entire coil structure) to the triplate. The coils are separated by a 2.54 cm plastic support (#5), which consists of four pieces that are machined to fit around coaxial load transmission line. (b) Magnetized load hardware configuration. The coaxial transmission line delivers power to the Al liner. The Helmholtz coils pre-impose an axial magnetic field of $B_z = 0.2 – 5.5$ T.

3.1.2 Liner Loads

Three types of liner loads were fabricated to investigate non-imploding, kink-seeded, and imploding cylindrical liner-plasmas. Each liner load has a unique support structure, which consists of a center dielectric region and two conducting end-caps, as shown in Figure 3.5. The support structure is required to support the ultrathin foil liners [YAG15]. When the chamber is placed under vacuum, atmospheric pressure compresses the AK gap of the radial transmission line by 1.2 mm, so that the liner load and load-transmission line must account for this varying anode-cathode (AK) distance. The simple solution to this problem was to create ~7 mm diameter holes in the anode and cathode load transmission line structures, so that the liner and its support structure are able to slide during vacuum pumpdown. By fixing the liner load to the cathode or anode with a single set-screw, the unfixed end is able to slide into the opposing electrode. Without this sliding system, the 400 nm liner would be destroyed during vacuum pumpdown.

The two end-caps are fabricated by wrapping a rectangular strip of 100 μm-thick aluminum tape (25 μm-thick aluminum and 75 μm-thick non-conducting adhesive) around a cylindrical dielectric rod (6.35 mm diameter, 3.4 mm height). The center dielectric region is designed to be 1 cm and may be unmodified for non-imploding liners, screw-threaded for kink-seeded liners, or have a reduced diameter for imploding liners. For the kink-seeded structure, the aluminum tape is placed directly around the ends of a 3.4 mm length 1/4-20 in. imperial threaded rod. For the imploding geometry, the diameter is reduced to 1-2 mm on a table-top lathe, which enables the liner to implode over a distance of 1-2 mm.

The final configuration is formed by wrapping a 400 nm-thick aluminum foil cut into a rectangular strip (1.5-cm by 2.2-cm) around the support structure, making contact with the aluminum tape on both ends. The length of the rectangular strip is cut slightly longer than the circumference of the support structure to ensure that there is an overlapping region and not a gap. At this point, wrinkles in the foil are smoothed by carefully adjusting the foil position of contact on the support structure. The thin-foil naturally adheres to the metallic support structure and therefore does not require an

adhesive to make electrical contact. The assembled liner is then loaded into the LTD so that the aluminum tape on the support regions makes electrical contact with the anode and cathode. Due to the slightly larger diameter of the anode and cathode holes when compared to the assembled liner, the contact is not initially expected to be azimuthally continuous. This imperfect contact may be responsible for large axially directed non-uniformities in the self-emission observed in the liner early time, which are reduced later in time (likely as plasma from the 25 μm thick aluminum tape ablates and fills the anode and cathode holes).

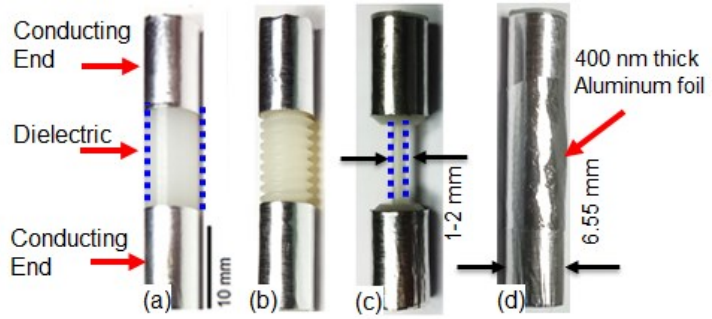

Figure 3.5. Liner load support structures. The center dielectric region is: (a) unmodified, for unseeded non-imploding liners, (b) threaded, for kink-seeded non-imploding liners, and (c) reduced diameter, for unseeded, imploding liners. The final configuration is shown in (d) and is identical for all liner loads, consisting of a 400 nm thick aluminum foil wrapped around the support structure, forming electrical contact at the conducting ends.

3.2 Diagnostics

3.2.1 B-dot Loops

The current was measured using four B-dot loops situated in the anode plate of the radial transmission line at a radius of 44 cm. The basic principle behind the B-dot diagnostic may be understood as follows. A time-changing magnetic field is generated perpendicular to the flow of a time-changing current in the transmission line. This field diffuses through a loop of wire, inducing a voltage that is proportional to the derivative of the current, following Faraday's Law of Induction. The loop of wire is typically oriented so that the normal vector of the area of the loop is parallel to the magnetic field to maximize the induced voltage signal. For the experiments in this thesis, only one of the radial transmission line B-dots produced a reliable signal for current measurements. Therefore, all current traces in Chapter 4 and Chapter 5 were measured using this B-dot. B-dots with larger area and multiple loops are currently being developed to increase the signal-to-noise ratio in order to improve our current measuring capabilities.

3.2.2 Laser System Overview and Stability

The laser backlighter used for these experiments was a 2-ns pulse-length, frequency-doubled Nd:YAG laser for shadowgraphy and interferometry at 532 nm. The two beam-paths used are shown in Figure 3.6 and Figure 3.7. The first beam-path, used for the original experiments, split the beam into four paths/delays to image the plasma at 20 ns intervals. One of the four beam paths incorporated an air wedge interferometer, which provided simultaneous images of shadowgraphy and interferometry. The beams intersected the load on the same horizontal plane at 1.3 ± 0.2 degree intervals, giving a total angular spread of the four beams of 3.9 degrees. The shadowgraphs are captured using Canon Rebel XTi and XSi cameras. The resolutions for all beam paths are measured at better than 100 μm/line pair using a 1951 USAF resolution target. Neutral-density filters and 532 nm line-filters are used to limit plasma self-emission on the shadowgraph images.

The second beam-path, shown in Figure 3.7, incorporated both laser backlighting and self-emission using a 12-frame intensified CCD camera, gated at 10 ns. To successfully incorporate the laser with the framing camera, a beam-splitting system was devised that splits the single 2-ns laser pulse to generate 12+ beams that are superimposed in space but delayed temporally. This was accomplished by using a 3.05 m length resonating cavity with two 95%/5% beam splitters, corresponding to a 10 ns delay between pulses. The first beam splitter allowed the laser pulse to enter the cavity, and the second beam splitter directed the train of pulses through the target chamber and to the imaging system. Due to the two beam splitters, the intensity of each subsequent pulse is reduced by ~10%. The framing camera collected the 2 ns backlit image in addition to plasma self-emission (filtered at 532 nm, no neutral density) over the 10 ns framing-camera window. This system allowed the tracking of individual features from the same angle of incidence in both shadowgraphy and self-emission with 12-frames over a 110 ns window. For both systems, a 2.36 mm thick plastic shield was placed between the load and vacuum window ports to protect the windows from load debris.

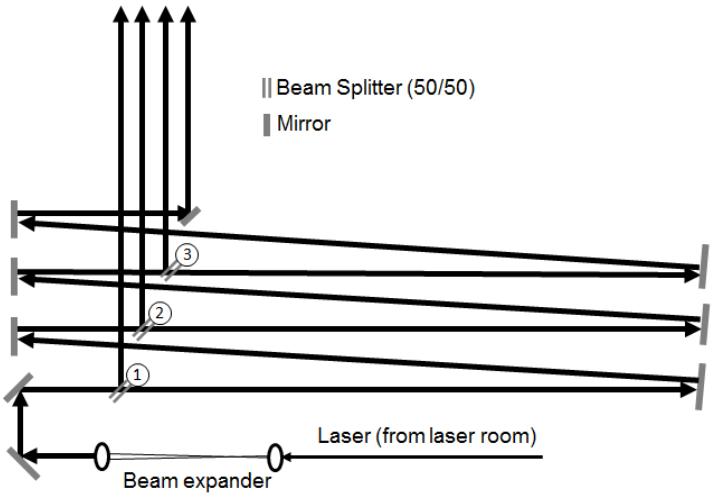

Figure 3.6. Optical system used to generate four beams (not drawn to scale). The incident pulse (2 ns pulse length, 532 nm wavelength, 50 mJ) is split consecutively at three locations using the beamsplitters identified in the figure. The path difference and therefore temporal delay is approximately the same for the four beams (20 ns). The beams intersect the load on the same horizontal plane at 1.3 $\pm$ 0.2 degree intervals, giving a total angular spread of the four beams of 3.9 degrees.

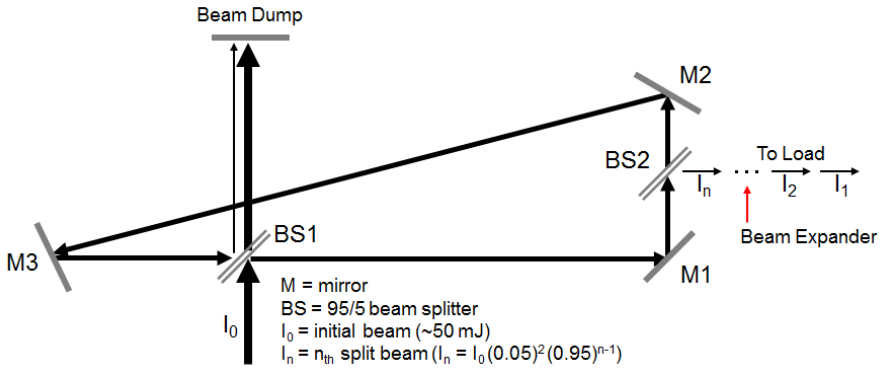

Figure 3.7. Optical system used to generate 12+ superimposed beams (not drawn to scale). The incident pulse (2 ns pulse length, 532 nm wavelength, 50 mJ) is passed through beam splitter BS1 so that a small fraction of the beam is trapped between the resonating cavity formed by mirrors M1, M2, and M3. Beam splitter BS2 directs a sequence of pulses to the target chamber. The 2 ns length pulses are delayed temporally by 10 ns due to the 3.05 m resonating cavity length. The beam is expanded after exiting BS2 and before traveling to the load. The resonating cavity M1-M2-M3 is conditionally stable.

The stability of the resonating cavity may be determined using a ray transfer matrix analysis [SIL04]. The transfer matrix is determined by multiplying the matrices of the elements in the optical cavity, and can be expressed as a two-by-two matrix,

$$T = \begin{bmatrix} A & B \\ C & D \end{bmatrix} \tag{3.1}$$

Once the transfer matrix has been determined (see below), the stability of the system is given by the condition,

$$0 \leq \frac{A+D+2}{4} \leq 1 \tag{3.2}$$

Note the B and C components do not enter the stability criterion. For the planar system, the total transfer matrix T is simply the transfer matrix T_d for propagation of light in free space over a distance d, given by

$$T = T_d = \begin{bmatrix} 1 & d \\ 0 & 1 \end{bmatrix} \tag{3.3}$$

where d = 3.05 m is the distance traveled by a ray of light in the optical cavity (note the planar mirrors do not require matrix elements). The A and D components yield $(A + D + 2)/4 = 1$, which indicates the planar mirror system is shown in Figure 3.7 is conditionally stable. This means, assuming perfect alignment, the laser beam will eventually expand beyond the size of the mirrors due to its inherent divergence. Small misalignments from the optical axis will cause the beam to eventually miss one of the mirrors. This was the case for the experimental setup, which only trapped ~12 beams.

A new, stable system was devised (and is currently implemented) using concave mirrors (focal length f = 0.5 m) to produce a stable cavity with a 15 ns inter-beam delay. This system is shown in Figure 3.8, and includes the 355 nm ultraviolet beam path. The total transfer matrix now requires the concave mirrors to be included. The concave mirror matrix component is given by

$$M = \begin{bmatrix} 1 & 0 \\ -1/f & 1 \end{bmatrix} \tag{3.4}$$

so that the total transfer matrix is

$$T = M.T_1.M.T_2 \tag{3.5}$$

where $T_1 = \begin{bmatrix} 1 & d_1 \\ 0 & 1 \end{bmatrix}$, $T_2 = \begin{bmatrix} 1 & d_2 \\ 0 & 1 \end{bmatrix}$, and d_1 = 1.003 m and d_2 = 3.569 m are the distances between the concave mirrors traveling along the resonating cavity. Note the total distance $d = d_1 + d_2$ = 4.572 m corresponds to approximately 15 ns delays between beams. Carrying out the matrix multiplication yields matrix components A = -6.138 and D = 4.169, so that $(A + D + 2)/4$ = 0. 0078 satisfies the stability condition in Equation (3.2). To minimize beam deformation by the concave mirrors, the reflection angles must be kept small, as shown in Figure 3.8. Note that it may be possible to use the system in Figure 3.7 and include two lenses in the resonating cavity. For lenses with focal length f = 0.5 m and keeping the same distances d_1 and d_2 as the concave mirror cavity, the ray transfer matrix for this system is identical to Equation 3.5.

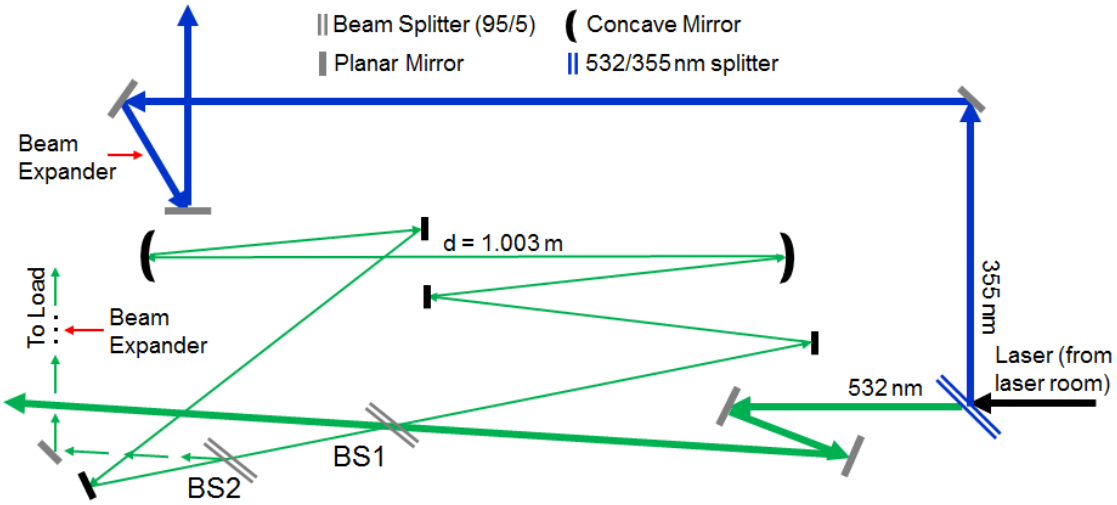

Figure 3.8. Stable optical system used to generate 12+ superimposed beams at 532 nm and a single beam at 355 nm (not drawn to scale). The incident pulse is passed through the 532/355 nm splitter, separating visible and ultraviolet components. The 532 nm beam is then passed through beam splitter BS1 so that a small fraction of the beam is trapped between the resonating cavity formed by the mirrors in black. Beam splitter BS2 directs a sequence of pulses to the target chamber. The 2 ns length pulses are delayed temporally by 15 ns due to the 4.572 m resonating cavity length. For stability, the distance between the concave mirrors is d = 1.003 m. The small reflection angles on the concave mirrors are required to minimize beam deformation. The locations of the beam expanders are identified using red arrows.

3.2.3 Laser Deflection and Shadowgraphy

When laser light is incident upon plasma, the rays of light will refract due to the plasma index of refraction. The plasma index of refraction is determined by the electron density, and can be estimated using the dispersion relation for simple plasma oscillations. The trajectory of the light rays thus primarily depends on the first and second derivative of the electron density in the plasma, and may be investigated using a variety of techniques, including laser deflection, Schlieren, shadowgraphy, and interferometry. The equation for laser deflection is determined by the first derivative in the index of

refraction, which yields a deflection angle θ given by the following equation

$$\theta = \frac{1}{n_0}\int_0^L \nabla n \, ds, \tag{3.6}$$

where L is the distance a light ray travels through the plasma, and n and n_0 are the indices of refraction of the plasma and vacuum, respectively. Using the dispersion relation for a plasma wave, this equation may be expressed in terms of the electron density n_e,

$$\theta \sim L \, \nabla n_e \left(\frac{\lambda^2 e^2}{8\pi^2 c^2 m_e \varepsilon_0}\right), \tag{3.7}$$

where λ is the laser wavelength, e and m_e are the electron charge and mass, respectively, c is the speed of light and ε_0 is the vacuum permittivity. The maximum gradient in electron density for our system may then be estimated as follows. The distance the laser light travels through the plasma is ~5 mm, the length from the plasma to the imaging lens is 2 m, the diameter of the lens is 5 cm, and the wavelength of the laser light is 532 nm. Using Equation (3.7), the maximum electron density gradient that is capable of being collected by the lens is ∇n_e =2*10^{19}/(cm^3-mm). Density gradients above this value will be completely deflected outside of the imaging system and leave behind a dark region on the CCD. This dark region is typically referred to as the shadowgraph of the plasma, despite the shadowgraphy effect being due to the second derivative of the index of refraction (and therefore the second derivative of the electron density).

The shadowgraphy effect may be understood as follows. First, consider an object with a constant gradient in the index of refraction. Let us suppose that ∇n is sufficiently small to be collected by the imaging system. Rays of laser light will be uniformly shifted by an angle according to Equation (3.7) and therefore uniformly illuminate the CCD, producing no variation in the intensity of light incident upon the CCD. Now, suppose that there is a second derivative in the index of refraction, i.e. a derivative in ∇n. Rays of light will now be deflected non-uniformly, resulting in both bright and dark regions on the

CCD depending on whether the rays overlap or not. The change in light intensity I imaged on the CCD obeys the equation [HUD65]

$$\frac{\Delta I}{I} = D\int_0^L \left(\frac{\partial^2}{\partial x^2} + \frac{\partial^2}{\partial y^2}\right) \ln[\mathrm{n}(x,y,z)]dz, \tag{3.8}$$

where D is the distance from the plasma to the lens and L is the distance a ray of light travels through the plasma. This equation shows the dependency of bright and dark spots on the second derivative on the index of refraction due to the shadowgraphy effect. This method is useful for studying objects with sharp derivatives in gradients, such as the boundary of a shock front or plasma. However, the primary effect resulting in the plasma shadow appears to be due to the first derivative of the index of refraction and therefore due to laser deflection outside of the imaging system. This conclusion is determined by examining the interferometry data (which depends on constructive and destructive interference of two beams of light due to variations in phase, rather than the deflection of light rays) in Chapter 5, Section 5.1.1, which showed a density gradient of $\nabla n_e \sim 10^{19}/(\mathrm{cm}^3\text{-mm})$ at the very edge of the plasma, near the limit of density gradients that our system can support. Two additional effects to consider are: (1) the absorption of laser light by the plasma, which would also directly result in a shadow of the plasma, and, (2) the effects of neutral atoms, which deflect laser light in the opposite direction than that by electron gradients.

3.2.4 Laser Interferometry

When laser light travels through a plasma and emerges, its phase is changed due to the index of refraction of the plasma. This change in phase can be used to calculate the index of refraction by combining the phase-shifted light with a beam of laser light that has not been phase shifted. This process results in bright and dark fringes that are due to constructive and destructive interference of the two beams. The analysis for extracting electron density from an interferogram is presented in Chapter 5.

One particularly common interferometry configuration is the Mach-Zehnder interferometer. For this configuration, a laser beam is split into two beams referred to as the reference beam and the probe beam. The probe beam is passed through the phase object (i.e. the plasma) and undergoes a shift in phase, while the reference beam passes through an adjacent region and is not shifted in phase. These two beams are subsequently combined using a beam-splitter in order to generate the interference pattern.

The interferometer used to obtain the electron density in Chapter 5 was an air-gap interferometer [PIK01]. For this type of system, the laser beam is split into two beams *after* having passed through the plasma (and a small region adjacent to the plasma), and having been collected by an imaging lens. This is accomplished using two right-angle prisms, arranged so that the focal point of the beam is situated in the air-gap between the prisms, as shown in Figure 3.9. The two beams, referred to as A and B (shown in red and blue in the image), are incident upon a CCD camera where their interference may be recorded. The two prisms are configured with a small, adjustable angle, which allows the separation of the two beams on the CCD to be controlled. For this technique, it is essential that the beam is offset from the center of the plasma **z-**axis, so that it consists of two portions, referred to as the: (1) reference and (2) phase-shifted regions. The reference region of beam A is then combined with the phase-shifted region of beam B, generating an interferogram. In order to obtain the fringe shift information (from which the electron density may be extracted), a post-shot interferogram is required to obtain a set of reference fringes. The reference interferogram is recorded after the shot when the liner is completely destroyed, enabling reference fringes that would otherwise be blocked by the liner to be recorded and compared to those of the imploding liner. An advantage to this technique is that the phase-shifted region of beam A simultaneously generates a shadowgraph on the CCD. In addition, the method generally results in a cleaner interferogram, as the reference beam and phase-shifted beam both experience nearly the same variations in phase as they travel through the vacuum windows, Lexan debris shield, and any other refractive objects in the optical path to the CCD. These variations are cancelled upon interference. Finally, this method is simple to configure and focus,

requiring only two right-angle prisms situated at the focal point of the imaging lens. Differences in path length of the reference and phase-shifted portions are inherently minimal, which may not be the case in Mach-Zehnder interferometry.

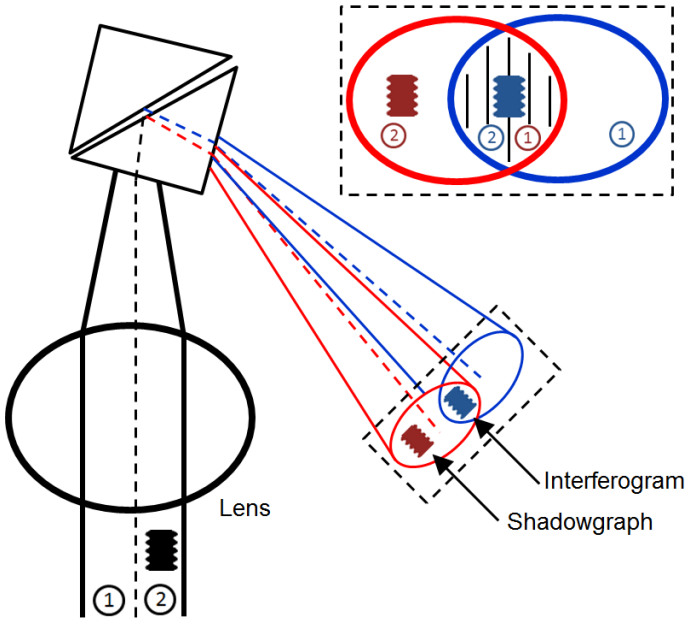

Figure 3.9. Air wedge interferometer configuration. The beam axis (dashed line) is offset so that two regions are generated. Region 1 is unshifted in phase, and region 2 is shifted in phase as it propagates through the plasma. The beam is focused to a point between the two right angle prisms. The two prisms, separated by a small gap, split the single laser beam (black) into two beams (red and blue). Region 1 (unshifted) of the red beam is combined with region 2 (phase shifted) of the blue beam to generate an interference pattern on the image collector. Region 2 (phase shifted) of the red beam is used to generate a shadowgraph. Note: the colors indicate the color of the beam in the diagram and are not related to the wavelength of the laser. The dashed box indicates an image collecting device.

3.3 Implementation of Axial Magnetic Fields

3.3.1 Coil Design and Power Delivery

A set of Helmholtz coils consisting of two 80-turn coils was used to pre-impose axial magnetic fields of 0.2 – 2.0 T. The coils were fabricated by Sandia National Laboratories [ROV14], and are the same coils utilized on the Z Machine to magnetize MagLIF experiments. The pulsed power system used to drive the coils is the same system used to drive the axial magnetic field on the Michigan Electron Long Beam Accelerator (MELBA), and consists of a 5 kV, 1.2 mF capacitor bank with an ignitron triggering system. The LTD is triggered at the maximum magnetic field value in the pulse, which occurs ~2 ms after the start of coil current. The coil current pulse is extremely long when compared to the LTD current pulse, which allows the axial magnetic field to fully diffuse through the load hardware (Section 3.3.2), and provides a constant-value axial magnetic field throughout the ~400 ns experimental window. Coil diagrams, operating procedures and magnetic probe calibration are presented in Appendix A.

3.3.2 Hardware Design and Magnetic Field Diffusion

The coil hardware consists of a coaxial transmission line (3.81 cm ID outer conductor and 2.54 cm OD inner conductor) that feeds the power to the load, as shown in Figure 3.4, above. Four return current posts at the liner load height enable a wide area for imaging of the plasma. The top plate that connects the liner to the return current posts has various holes machined in order to allow diagnostic access to the liner region and situate a fiducial screw for image alignment and scaling. The load hardware was designed to accommodate the Sandia Helmholtz coils, which slide directly around the outer coaxial region of the transmission line. Two stainless steel plates comprise the coil housing and are required to counteract the extreme $\boldsymbol{J} \times \boldsymbol{B}$ forces that are generated during coil operation. The coils are separated by a 2.54 cm plastic spacer, as seen in Figure 3.4, which enables laser imaging access to the load region. The coil housing is bolted directly to pre-existing holes in the radial transmission line anode plate.

The axial magnetic field diffusion into the load region was investigated using the transient field solver in ANSYS Maxwell. The simulation geometry shown in Figure 3.10 included the triplate, aluminum triplate-coaxial adaptors, coaxial transmission line, liner load, top disc, return current posts, coil housing, and a portion of the radial transmission line. The circuit code PSpice was used to calculate the expected current trace (details are presented in Appendix A), which was used to drive the two 80-turn Helmholtz coils in Maxwell. For these simulations, the material of the coaxial transmission line, top disc, and return current posts (shown in blue in Figure 3.10) was varied. The two materials investigated were aluminum and stainless steel, which were chosen because of their common use in parts manufacturing. For these simulations, the default conductivities of $3.8 \cdot 10^7$ S/m and $1.1 \cdot 10^6$ S/m were used for aluminum and stainless steel, respectively. The results of the simulation are shown in Figure 3.11, which shows a snapshot of the magnetic field profile at peak current (1.6 ms). As shown in the figure, the magnetic field value is significantly reduced when using aluminum hardware. The magnetic field in the load region was 2.7 T, compared to 5.0 T for the stainless hardware. The fundamental reason for this discrepancy is the lower conductivity for stainless steel, which permits a faster magnetic field diffusion time. These simulations motivated the manufacture of stainless steel hardware for the coaxial region. The material of the triplate-to-coaxial adaptors was also varied from aluminum to stainless; however, no differences were found in the magnetic field value at the load region. This permitted the adaptors to be manufactured from aluminum, which is easier to machine.

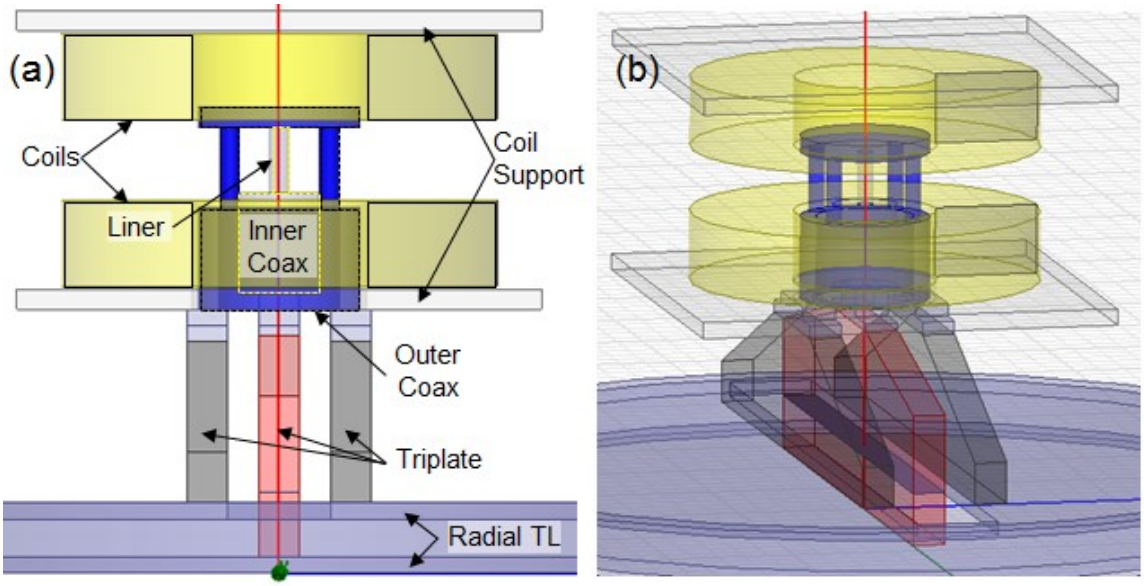

Figure 3.10. ANSYS Maxwell simulation geometry for investigating the diffusion of the axial magnetic field from the coils to the load region.

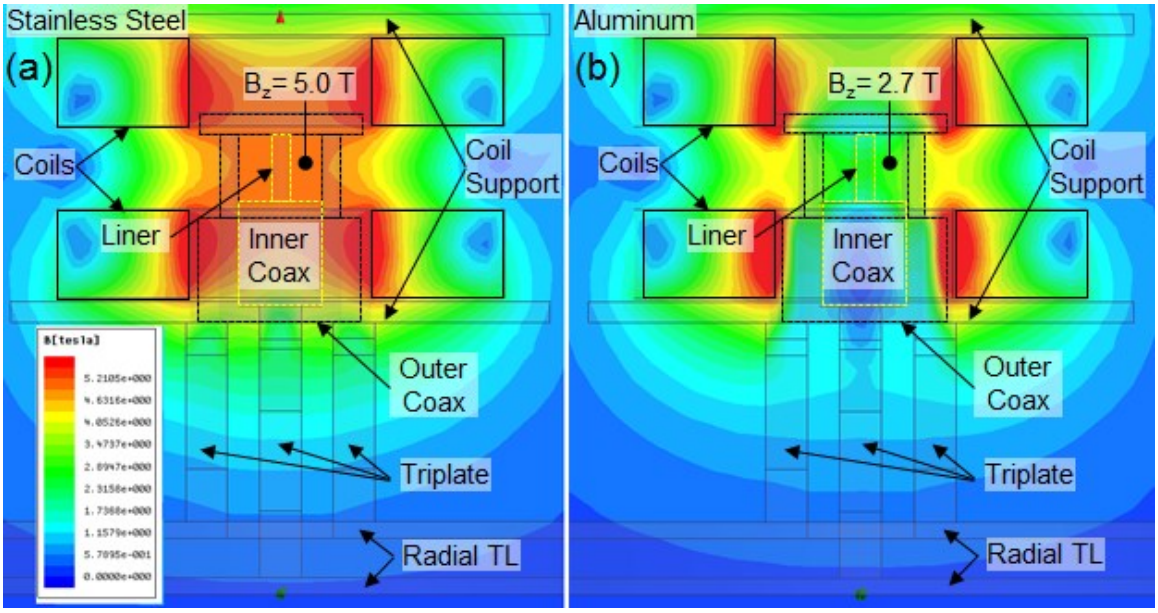

Figure 3.11. ANSYS Maxwell simulations for investigating the diffusion of the axial magnetic field from the coils to the load region. Magnetic field profiles are shown for (a) stainless steel hardware and (b) aluminum hardware. The magnetic field in the load region is significantly larger for stainless steel hardware when compared to aluminum.

CHAPTER 4
EXPERIMENTAL RESULTS FOR NON-IMPLODING LINERS

This chapter presents the results of an investigation of the effects of axial magnetic fields on current-driven instabilities, namely the sausage ($m = 0$), kink ($m = 1$), and helical ($m \geq 1$) instabilities, *in the absence of interface acceleration* in order to minimize the effects of the acceleration-driven Rayleigh-Taylor instability. To minimize the liner-plasma interface acceleration, the 400 nm aluminum liner was directly placed around a non-conducting support structure. When the LTD is discharged, the current runs primarily through the highly conductive aluminum, ionizing it and forming a dense plasma ($n > 10^{19}/\text{cm}^3$) sufficiently hot to emit light in the visible spectrum. The current generates an azimuthal magnetic field and thus a magnetic pressure which exerts a radially inward force on the liner-plasma. However, due to the dielectric support structure, the plasma cannot implode; rather, it expands with a nearly constant velocity as more energy is deposited in the plasma from the LTD generator. It is important to mention that if the radius of the dielectric support structure were reduced (while maintaining the liner radius fixed), the magnetic pressure would be sufficient to implode the liner-plasma. In this scenario, the current-driven MHD instabilities may couple to the magneto Rayleigh-Taylor instability. This geometry and its important consequences are explored in Chapter 5.

In addition to preventing the liner-plasma from imploding, the internal support structure presents the interesting possibility of setting an internal spatial boundary condition, which may be used to seed instabilities in the plasma at a given axial wavelength and azimuthal mode number. In Section 4.1, the support structure was a straight-cylindrical plastic rod and used to analyze the natural instability modes that arise with and without an externally applied axial magnetic field. With no axial magnetic field,

the $m = 0$ sausage instability developed. Adding a relatively small axial magnetic field of 1.1 T resulted in an $m = +2$ helical mode, where the plasma helices spiral in the same sense of direction as the external, global magnetic field (see Section 2.1 for the definitions of the $\pm m$ modes). In Section 4.2, the internal support structure was modified to seed the kink ($m = 1$) instability by using a threaded-cylindrical plastic rod. By seeding the kink instability, we were able to fix the axial wavelength and azimuthal mode number in order to isolate the effects of the axial magnetic field. It was found that the seeded mode persisted despite the orientation of the applied axial field, and that the negative mode, where the plasma helices spiral against the global magnetic field, was the more stable configuration.

To improve our understanding of these non-imploding systems, the arbitrary Lagrangian-Eulerian (ALE) code HYDRA [MAR01, KON09] was used. It was found that the liner does not ablate into a uniform density plasma, but rather distributes itself into a Gaussian-like density profile whose thickness increases from 400 nm to ~200 μm over the course of 200 ns. Profiles for density, temperature, magnetic field, and current density were simulated. In order to corroborate the experimental results with analytic theory, we used the Weis-Zhang-Lau three-region ideal MHD model to calculate analytic growth rates to show that these current-driven MHD modes may indeed grow in the absence of MRT for the experimental parameters. These calculations indicate there is a window in time when all MHD modes are completely stabilized, with higher order m modes becoming the first to de-stabilize.

4.1 Experimental Results for Unseeded, Non-imploding Liners

We performed twelve shots using the straight-cylindrical, unseeded configuration, using three values for the axial magnetic field (B_z = 0, +1.1, -1.1 T) and two imaging techniques: (1) combination of self-emission and 532 nm laser shadowgraphy at 10 ns intervals, and (2) only self-emission at variable timing intervals. A summary of the experimental shots is presented in Table 4.1. The primary advantage of the first technique is that the shadowgraphy boundary may be determined *in addition* to the self-emission features, which give information about structures on the face of the plasma. The shadowgraphy boundary is typically observed as a thin, dark band located between the self-emitting region and the laser backlighting region (see Figure 4.1 in Section 4.1.1) and is thus useful for defining the plasma boundary, which may subsequently be used to measure the plasma radius and instability amplitude. The self-emission features may then be used to trace bright and dark bands horizontally across the face of the plasma in order to connect instability bumps and necks. However, the disadvantages are that the timing interval is limited to 10 ns (corresponding to the laser pulse interval timing) and that the laser backlighter intensity for subsequent images is reduced as the trapped beam loses energy in the resonating cavity. This latter effect can be seen in the images in Figure 4.1(a-c), which have a bright laser backlight in the early images, followed by a much darker backlight in the later images. A final disadvantage to consider is that the resonating cavity must be aligned and synchronized to the framing camera intervals; a nontrivial task in itself.

Using only the plasma self-emission offers a great advantage by providing flexibility in timing, which enables observation of the liner-plasma any time there is sufficient self-emission light to be recorded by the ICCD fast framing camera. In addition, because there is no laser backlight, a computerized algorithm can quickly and effectively trace the plasma self-emission boundary.

In order to directly compare instability amplitude and plasma dynamics from shot-to-shot, it is important that the current traces be nearly identical. This means that the overall magnetic field, and thus the driving term for the sausage and helical modes, must

be approximately equal (see Equation (2.1) in Chapter 2) to enable the effects of the axial magnetic field to be directly compared. Figure 4.2 shows the current traces and timings for the unseeded liner experiments, which are nearly identical for the shadowgraphy/self-emission shots in Figure 4.2(a) and slightly more varied in peak current and risetime for the self-emission only shots in Figure 4.2(b). Note the dip in the current traces, which occurs at 340 to 380 ns, marks the end of the useful current signal. The origin of this dip is not completely understood.

Table 4.1. Summary of experimental data for unseeded, non-imploding liners. (a) Shadowgraphy and self-emission combination diagnostic. (b) Self-emission only diagnostic. The growth rate is the measured using an exponential fit to the instability amplitude, $A = A_0 \exp[\gamma t]$, where γ is the growth rate and A_0 is the amplitude at the start of the current ($t = 0$) and characterizes the amplitude of the early-time structures that seeded the sausage and helical modes (see Section 4.1.2.A, below). The expansion velocity, V_{exp}, is fit using the mean plasma radius. Uncertainties are estimated from the standard error of fits.

(a) Shadowgraphy

Shot	B_z (T)	Mode	Growth Rate (1/μs)	E-Folding (ns)	A_0 (μm)	V_{exp} (μm/ns)	Image Timing (ns)	I_{max} (kA)
1189	0	Sausage (m = 0)	7.2±0.3	139±6	38±4	3.8±0.2	245-345	560
1209	0	Sausage (m = 0)	10.8±0.5	93±4	13±1	3.6±0.1	120-220	560
1206	-1.1	Helical (m = +2)	9.0±0.5	111±6	14±2	3.6±0.1	210-290	580
1208	-1.1	Helical (m = +2)	9.9±0.7	101±7	13±2	3.5±0.1	125-225	570
1190	+1.1	Helical (m = +2)	8.0±0.6	125±9	20±3	3.6±0.1	255-325	570

(b) Self-Emission

Shot	B_z (T)	Mode	Growth Rate (1/μs)	E-Folding (ns)	A_0 (μm)	V_{exp} (μm/ns)	Image Timing (ns)	I_{max} (kA)
1210	0	Sausage (m = 0)	11.9±0.3	84±2	4.4±0.5	2.8±0.1	175-325	560
1211	0	Sausage (m = 0)	12.8±0.3	78±2	2.6±0.2	3.0±0.1	170-320	540
1212	-1.1	Helical (m = +2)	8.9±0.2	112±3	4.2±0.3	3.1±0.1	245-345	590
1213	-1.1	Helical (m = +2)	7.7±0.3	130±5	7.2±0.7	2.8±0.2	190-390	580
1214	+1.1	Helical (m = +2)	8.5±0.7	118±10	7.3±1.7	3.1±0.1	225-350	580
1215	+1.1	Helical (m = +2)	6.9±0.5	145±11	10.2±1.6	3.0±0.2	215-315	570

4.1.1 Self-emission and Shadowgraphy Images

Figure 4.1 shows a series of six shots using three magnetic field configurations, B_z = 0 T, +1.1 T, and -1.1 T, for the combination shadowgraphy-self emission diagnostic (Figure 4.1(a-c)) and the self-emission only diagnostic (Figure 4.1(d-f)). For each diagnostic, the series shows three images taken at approximately the same time in order to directly compare features. Early in time (< 200 ns), the self-emission structures showed very large scale non-uniformities in the axial direction. This is particularly evident in the first row of Figure 4.1(d-f)). The sharp vertical line near the center of Figure 4.1(d) at t = 197 ns is due to the aluminum foil overlap. In the next image (t = 297 ns), this line completely disappeared, suggesting that the overlapping region of the liner merged. These early time images reveal additional large scale, vertical non-uniformities in self-emission (see the right side of Figure 4.1(d, t = 197 ns) and Figure 4.1(f, t = 191 ns) which show bright and dark bands in the axial direction. The likely origin is due to non-uniformities in current flow, perhaps exacerbated by the filamentation form of the electrothermal instability [PET12, PET13, PET14, ORE08, ROU08, STE16]. The non-uniformities in current flow are likely due to two imperfect contact regions: (1) between the 400 nm liner and the 25 μm aluminum tape, and (2) between the 25 μm tape and the anode and cathode sliding contact structures. These axially directed non-uniformities decreased over time, indicating that current flow became more uniform.

After the large scale vertical non-uniformities disappeared, the plasma self-emission revealed dark and bright striations that connected instability bumps and necks, respectively. These structures formed around 300 ns, and became clearer as time progressed and the instability structures grew to large amplitudes. Hereafter, the self-emission structures refer to these later time structures, and not the early time axially directed non-uniformities. While it is clear the self-emission structures are related to the instability peaks and valleys, the exact mechanism of their formation is not completely understood. One possible mechanism is that the bright striations form at the neck of the plasma where the plasma radius is smaller than the adjacent regions, resulting in a larger current density, localized heating, and increased light emission. In this scenario, the dark

bands form at the plasma bumps where there is more volume and less current density, resulting in less self-emission. A second mechanism may be due to the plasma opacity. Consider a hot, inner cylindrical shell of the liner-plasma that is self-emitting uniformly. The light from this region will be absorbed less in the plasma necks, where there is less mass, and more in the plasma bumps, where there is more mass. In this fashion, less light is transmitted through the liner-plasma in the thicker bumps, and more light is transmitted in the thinner necks.

The dark and bright striations were found to be azimuthally correlated for the unseeded, unmagnetized liner images shown in Figure 4.1(a,d). As the interface acceleration was minimal (see Section 4.1.2.C) and the instability amplitude tended to grow exponentially, these structures are attributed to the current-driven, axisymmetric $m = 0$ sausage instability. As time evolved, the smaller instability structures ($\lambda \sim 0.9$ mm) merged to form larger wavelength instability structures ($\lambda \sim 1.4$-1.6 mm), retaining their axisymmetric nature throughout the merging process. Adding a relatively small axial magnetic field of 1.1 T (compared to the peak azimuthal field of ~30 T) in the *positive* or *negative* **z** direction destroyed the azimuthal symmetry and resulted in both smaller amplitude instability bumps and helically oriented self-emission striations (Figure 4.1(b,c,e,f)) with similar wavelengths ($\lambda \sim 0.8$ mm) to the smaller structures of the unmagnetized liner that appeared at earlier times (for example, compare $t = 256$ ns in Figure 4.1(a) with $t = 334$ ns and $t = 309$ ns in Figure 4.1(b) and Figure 4.1(c)). Comparing the self-emission features of the unmagnetized case to the magnetized case shows that the contrast of the dark and bright striations was reduced when the axial field was applied; a result which may be attributed to the smaller amplitude of the instability structures. The amplitude of the instability structures for the magnetized liners also tended to grow exponentially, indicating these were helical instability modes (i.e. modes with azimuthal mode number $|m| \geq 1$). See Chapter 2 for a discussion on the sign of the azimuthal mode number and its implications. For both axial field configurations, the helices spiraled in the direction of the global magnetic field (i.e. $m > 0$). This was indeed expected as positive mode numbers have larger growth rates than negative mode numbers

because the plasma helices experience a smaller, stabilizing magnetic tension. In Section 4.1.2.D, these self-emission striations are analyzed, and show two intertwined helices form to generate the m = +2 helical mode.

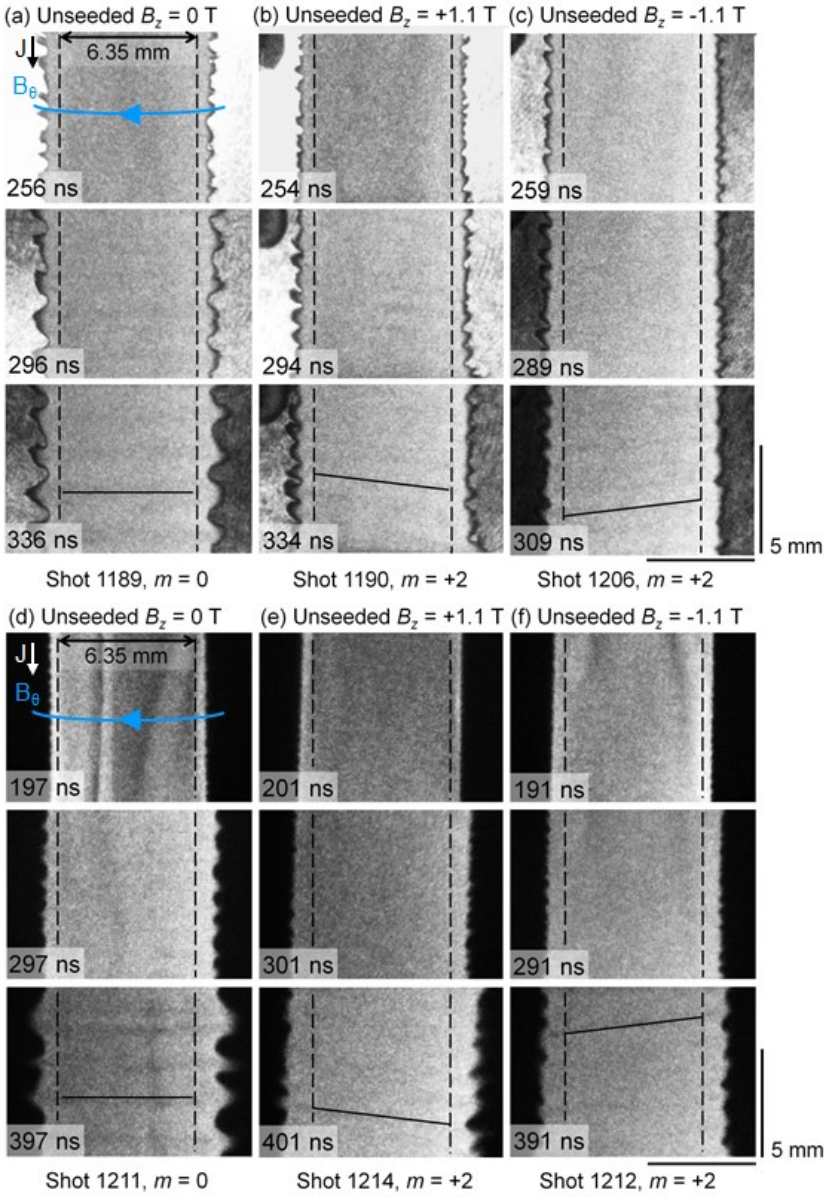

Figure 4.1. (a-c) Combination shadowgraphy and self-emission (filtered at 532 nm) and (d-f) self-emission only images for unseeded liners using axial magnetic field values of B_z = 0 T, +1.1 T, and -1.1 T. The dashed lines indicate the approximate position of the dielectric support structure, and the solid lines mark dark striation patterns, which connect bump-to-bump instability structures. The direction of the current density ***J*** and azimuthal magnetic field B_θ are indicated in (a) and (d).

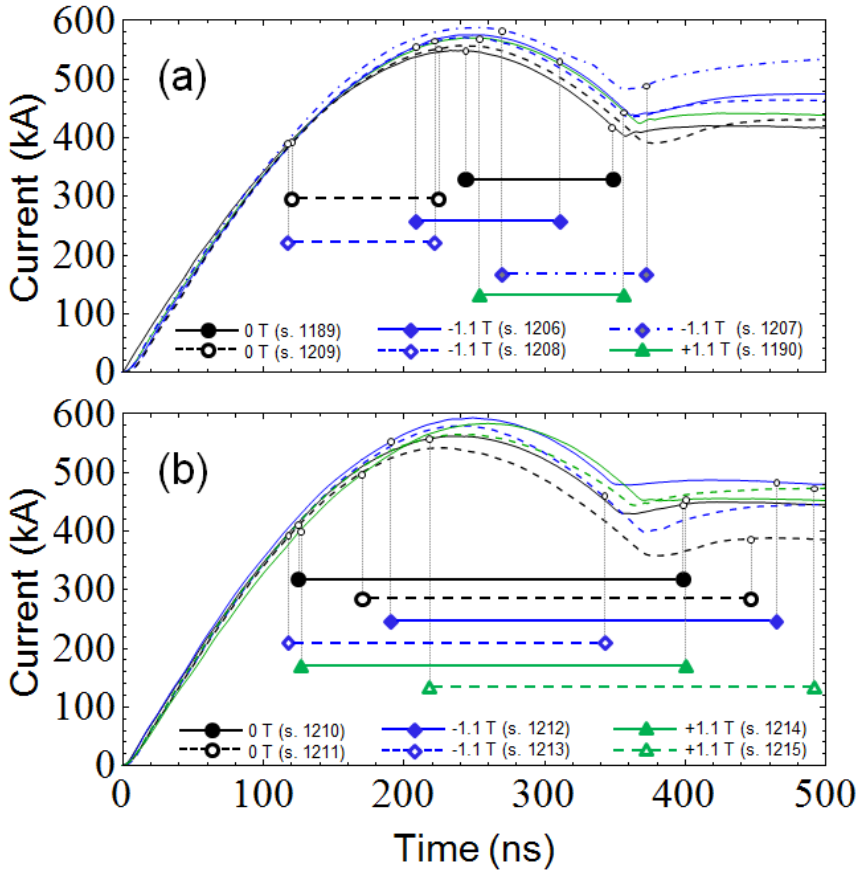

Figure 4.2. Current traces and image timings for: (a) combination shadowgraphy and self-emission, and (b) self-emission only. Symbols mark start and stop time of imaging window.

4.1.2 Instability Experimental Analysis

In this section we analyze the experimental amplitude of the instability structures that developed in the liner-plasma in order to measure and compare the exponential growth rates for the three magnetic fields tested (B_z = 0 T, +1.1 T, and -1.1 T). A summary of these results is presented in Table 4.1. In general, it was found that an axial magnetic field slightly reduced the growth rate early in time (before ~250 ns), but had little effect later in time (after ~250 ns). However, for all cases and for all times, the amplitude of the non-magnetized structures was larger than the magnetized structures.

This may be attributed to a combination of two factors: (1) a smaller growth rates for magnetized helical modes, when compared to the unmagnetized sausage mode (particularly early in time, when B_z is comparable to B_θ), and (2) an overall delayed onset of instability modes.

Appendix B describes the two algorithms used to trace the plasma boundary. They are briefly summarized here. The shadowgraphy images first require manual tracing, which is performed by modifying the image by marking a white line on the outer shadowgraphy boundary as shown in the sample image in Figure 4.3(a). The modified images are subsequently computer-read using the algorithm in Appendix B, which tracks the inner boundary of the marked white line, in order to obtain the plasma boundary (Figure 4.3(b), red line). The self-emission only images are directly computer-read using a separate algorithm that determines a characteristic brightness threshold for each image to trace the plasma boundary (Figure 4.3(c), white line).

The result of these algorithms is the plasma boundary as a function of vertical position, obtained for the left and right boundaries, one of which is shown in Figure 4.3(d). These boundaries are centered about the **z**-axis, which is determined using a pre-shot image. For each image, the mean of the left (right) plasma boundary gives the left (right) plasma radius, and the left (right) instability amplitude is obtained using the amplitude relationship for a sine wave, $A = \sqrt{2}\sigma$, where σ is the standard deviation in the radial position of the boundary. For the sample boundary in Figure 4.3(d), the black line represents the plasma radius as a function of axial position, the blue line represents the mean value, and the red lines mark the peak and trough of the instability measurement (note the distance between the red-lines is equal to twice the instability amplitude measurement). The final measurement is taken as the mean of the left and right radii and instability amplitudes; these are plotted in Figure 4.4 for the 12 shots reported here. The uncertainty is estimated by the difference in the left and right values; these are the error bars shown in the figures.

A. Instability Amplitude and Exponential Growth Rates

Figure 4.4(a) and (b) show plots of the instability amplitude as a function of time, measured using (a) shadowgraphy, and (b) self-emission only. The shadowgraphy data had larger amplitudes when compared to the self-emission only, which is simply because the shadowgraphy boundary is at a larger radius than the self-emission boundary. This explains the larger initial amplitudes, A_0, for the shadowgraphy data when compared to the self-emission only data in Table 4.1. Despite this, the two methods resulted in very similar growth rates (see Figure 4.5 and Table 4.1), which indicates that the self-emission only method may be more useful for quantitative instability analysis due to its flexibility in timing. On the other hand, the shadowgraphy images present a more detailed image of the plasma boundary (particularly early in time, when self-emission is low), which aids in identifying instability structures which, along with the self-emission striations, may be used to determine the azimuthal mode number.

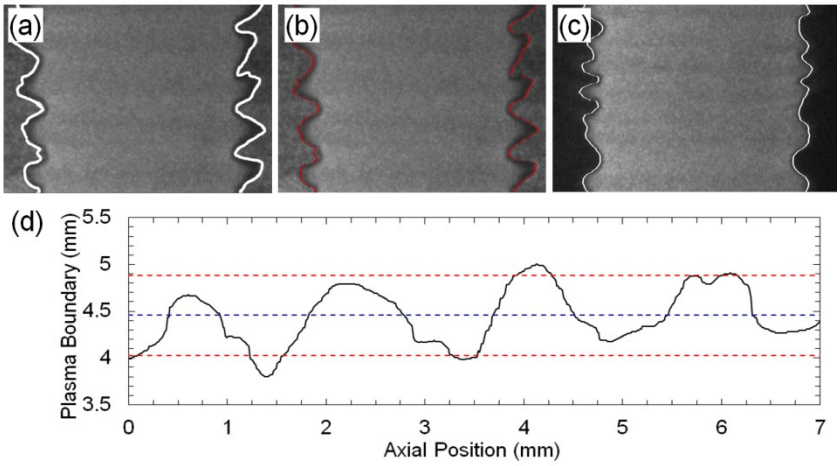

Figure 4.3. (a) Identification of shadowgraphy boundary. The white line is manually determined by tracing the outer shadowgraphy line. (b) The result of the computerized algorithm (red line) used to read-in the boundary in (a). (c) The result of the computerized algorithm (white line) for the self-emission only boundary, tracking the line corresponding to 40% of the characteristic maximum brightness. (d) A sample boundary showing the radial position of the plasma as a function of the axial position (black), the mean plasma radius R_{mean} (blue), and the peak and valley instability amplitude lines (red), corresponding to $A_{max,min} = R_{mean} \pm \sqrt{2}\sigma$, where σ is the standard deviation of the plasma boundary.

The experimental data show that an axial magnetic field reduces the overall instability growth. In all cases, the unmagnetized data had larger amplitude instability structures (see the black data points in Figure 4.4(a,b)). An important factor to consider here is the apparent amplitude reduction for a helically oriented structure when imaged from a line of sight that is perpendicular to the helical z-axis (as in this experiment). However, for the small helical pitch angles (~4 degrees with respect to the horizontal), this reduction is likely to be small. To measure the instability growth rate, we fit only the exponentially growing regions (identified on a semi-log plot) using the equation $A = A_0 \exp(\gamma t)$, where A is the instability amplitude at time t, A_0 is the fitted amplitude at $t = 0$ (corresponding to the start time of the current), and γ is the instability growth rate. The amplitude A_0 is not the true instability seed amplitude at $t = 0$, but rather a parameter that characterizes the amplitude of the structures that seeded the observed instability, as discussed in the end of this section. The fitted curves excluded data points that occurred during instability amplitude saturation in addition to data early in time that showed little change in image-to-image amplitude. For this discussion, we define saturation as any non-linear growth, which may be algebraic, constant, or decreasing in amplitude as a function of time. The non-linear growth typically begins when the ratio of instability amplitude to wavelength is no longer small [WEI15]. These growth rate data are summarized in Figure 4.5 and Table 4.1. From these fits, we see that the axial magnetic field reduced the instability growth rate when compared to the unmagnetized case (with the exception of the unmagnetized shot 1189, discussed below).

Shots with data after 300 ns showed saturation in the instability development. For the shadowgraphy case, amplitude data for both magnetized cases was reduced as shown in Figure 4.4(a), while for the self-emission only data, the saturation was characterized by an algebraically increasing instability growth (i.e. the amplitude growth is linearly proportional to time), as shown in Figure 4.4(b). This saturation occurs later in time for the magnetized liners (between 350 and 400 ns) than for the unmagnetized liners (~325 ns), which may be attributed to the smaller ratio of instability amplitude to axial wavelength for the magnetized liners. Note that this saturation likely explains the slightly

smaller growth rate for the $B_z = 0$, $m = 0$, shot 1189 data, which was captured later in time (t = 245-345 ns) when the saturation process has already begun.

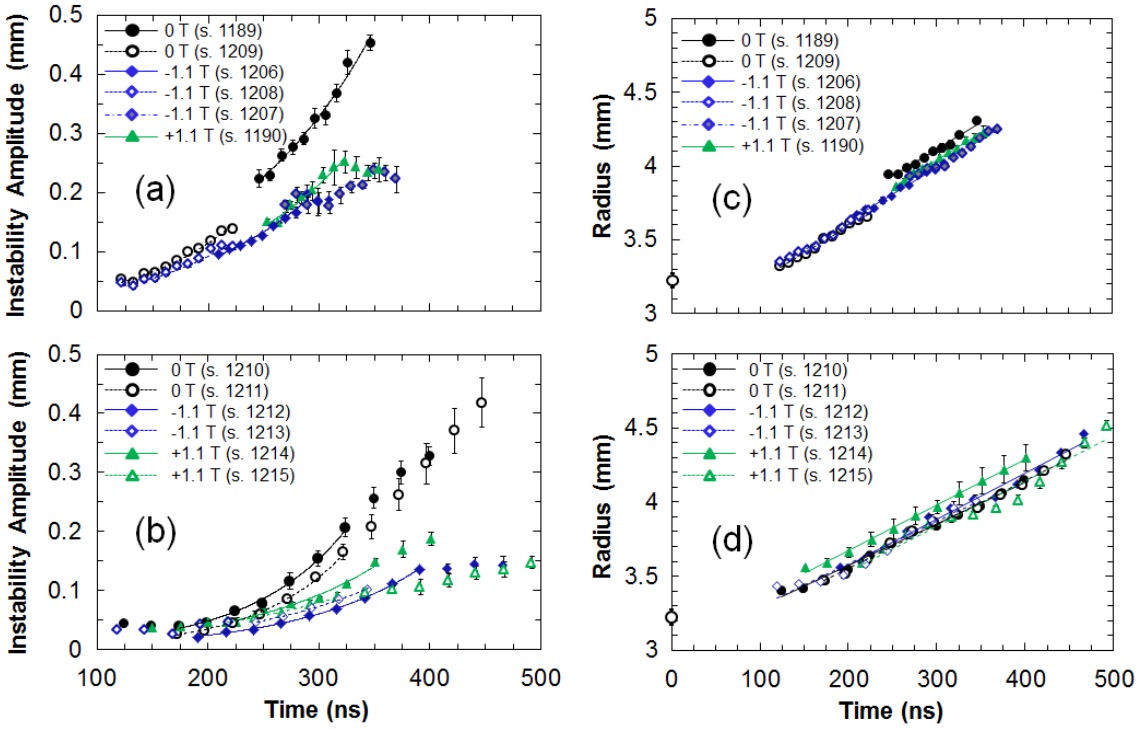

Figure 4.4. Instability amplitudes for: (a) shadowgraphy/self-emission diagnostic and (b) self-emission only diagnostic. The plots show exponential curves, fit only to the exponentially increasing time periods (identified on a semi-log plot), which are used to identify the instability growth rate γ and initial instability amplitude A_0. In (c) and (d), the mean plasma radius is shown for (c) shadowgraphy/self-emission diagnostic and (d) self-emission only. The initial liner radius is shown at $t = 0$. The data are fit using a linear regression in order to quantify the expansion velocity. Initial amplitude, growth rate, and expansion velocity are summarized in Table 4.1.

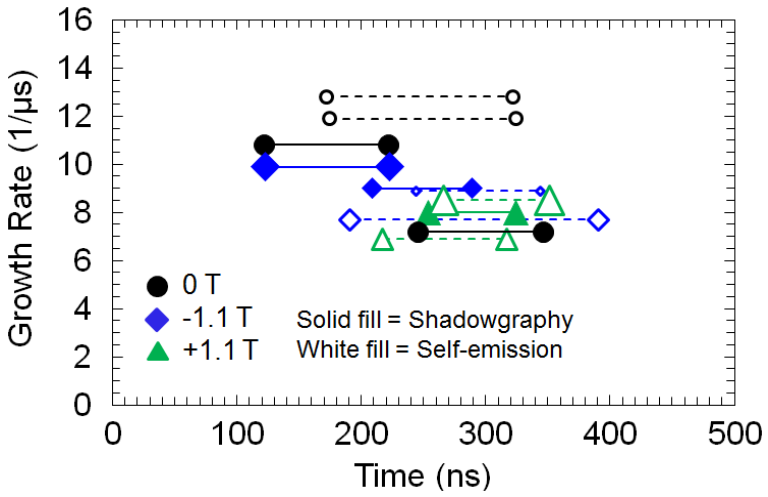

Figure 4.5. Summary of experimental growth rates, measured using an exponential fit to the data in Figure 4.1. Symbols show start and stop times of measurement window. Standard error of fit (68%) is given by size of symbol. The solid fill and solid lines indicate shadowgraphy/self-emission diagnostic, and the white fill and dashed lines indicate self-emission only.

Changing the direction of the axial magnetic field from -1.1 T (parallel to current) to +1.1 T (anti-parallel to current) did not have a significant effect on the instability amplitude or the instability growth. Despite small differences in instability amplitude and growth rate (which may be due to differences in the current pulse and therefore the magnetic field which ultimately drives the instabilities), the effect of the sign of the axial magnetic field (when no instability seeding is present) is not completely resolved. Using an ideal MHD model, there should be no difference in growth between an axial field that is parallel or anti-parallel to the direction of current flow. However, more complicated MHD models may include a Hall term (pp. 47 of [BEL06]), which incorporates a $\boldsymbol{J} \times \boldsymbol{B}$ term in the generalized Ohm's law that is dependent on the direction of current. To completely resolve this issue, larger axial magnetic fields could be used to enhance the Hall term and a smaller radius support structure could be implemented to enhance the instability growth rate. Also, a direct measurement of the current flowing in the liner would be required in addition to the present measurements which utilize B-dots in the transmission line at a 44 cm radius (from the center of the load). This could be

accomplished using micro B-dots positioned inside the return can, near the liner, or with a Rogowski coil The currently used method does not measure arcs or current losses in the transmission line that may occur within the 44 cm B-dot radius. Finally, a Hall-effect MHD code (such as the Perseus code at Cornell University [SEY11]) could be used to predict any differences in instability growth due to the parallel or anti-parallel orientation of the axial magnetic field compared to the current flow.

The initial amplitude data for the fitted growth rates, summarized in Table 4.1, were very similar despite the applied axial magnetic field. This was an unexpected result, as the theory (see Section 4.1.4) shows that adding an axial magnetic field delays the onset time of all instability modes. This delayed onset would have manifested itself as a reduced initial amplitude A_0 in the exponential fit $A = A_0\exp(\gamma t)$. For example, suppose the instabilities start growing at $t = t_s$ with an amplitude of A_{ts}. Setting the relationship for this delayed onset $A = A_{ts}\exp[\gamma(t - t_s)]$ equal to the fit relationship, we see that

$$A_0\exp(\gamma t) = (A_{ts}\exp[-\gamma t_s])\exp[\gamma t] \quad (4.1)$$

$$A_0 = A_{ts}\exp[-\gamma t_s] \quad (4.2)$$

Therefore, the measured amplitude should give us some indication of when the instabilities started growing (assuming the instabilities start growing from perturbations with a similar amplitude, A_{ts}); however, the measured A_0 were all very similar, which indicates the instabilities started growing at around the same point in time. Looking at Figure 4.4(a) and (b), the instability growth begins around 125 ns (for shadowgraphy, which captures low density, non-self-emitting bumps) and around 175 ns for self-emission only. The approximately identical start time for each measurement (despite the applied axial field value) indicates that there was not a *measurable* delayed instability onset time. Note that the theoretical growth rate curves for magnetized liners, which are calculated in Section 4.1.4 below, exhibit a delayed instability onset time—*this may indicate that the instability was seeded by an additional mechanism which governs the early time instability development.* The leading theory for this mechanism is the

electrothermal instability, which develops striations that grow perpendicular to the current flow [PET12, PET13, PET14, ORE08, ROU08, STE16].

B. Persistence of Exponential Growth

A particularly interesting feature of Figure 4.4 is the persistence of an exponential instability amplitude growth for over 300 ns despite: (1) the linear theory being applicable only for "small amplitude perturbations", (2) the (temporary) saturation in growth of instability features (saturation causes the growth rate to depart from an exponential dependence), and (3) the merging of instability bumps (see Figure 4.1(a-c), for example, in addition to the analysis below), which results in a time-changing wavelength. To study this process, the instability wavelength was determined using a method similar to a "zero crossing" method. For this method, the N axial positions where the plasma boundary is equal to the mean plasma boundary are identified. Then, a periodic structure is assumed in order to obtain $N-2$ wavelength measurements, as outlined in Figure 4.6. The final measurement is taken as the mean of these values. For this analysis, the "zero crossing" method was chosen because of its simplicity for extracting a single measurement of wavelength and its greater fidelity at large wavelength values, when compared to a Fourier analysis.

For this analysis, we focus on shot 1189 (B_z = 0 T, Figure 4.1(a)), where the instability bumps on the left side of the liner merged with an adjacent bump at approximately the same time, giving an approximately constant $\lambda(z)$. The values of instability wavelength (for the left side only) are plotted as a function of time in Figure 4.7(a), and show a discrete jump between 266 ns and 286 ns, where the wavelength increased from λ = 0.9 mm to λ = 1.4 mm after synchronous merger events. Figure 4.7(b) shows enlarged images for the four frames indicated in Figure 4.7(a). The images show a detailed process of the merging of two, smaller wavelength instability structures into a single, larger instability structure.

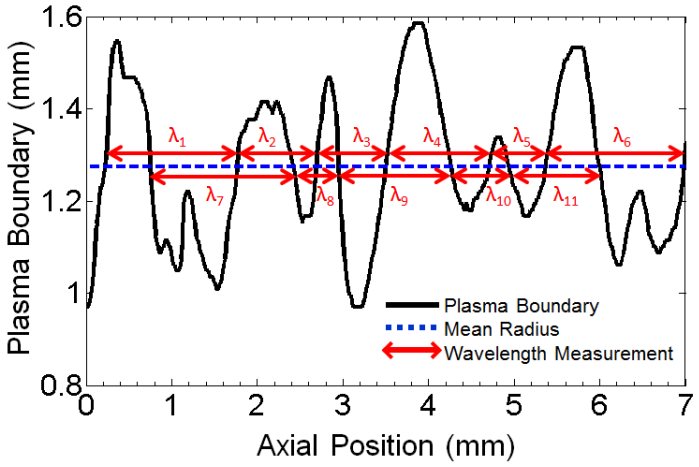

Figure 4.6. Method to measure wavelength. The final measurement is the average of all wavelengths determined using the "mean-crossing" of the plasma boundary.

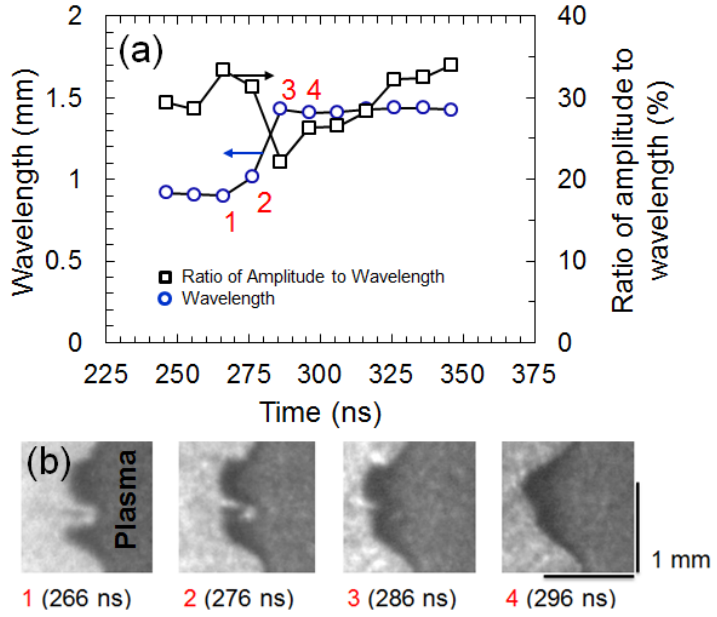

Figure 4.7. (a) Characteristic wavelength and ratio of amplitude to wavelength for the $m = 0$ sausage mode in shot 1189 ($B_z = 0$ T, Figure 4.1(a), left boundary only). (b) Detailed process of instability bumps merging. Data points marked in red in (a) correspond to frames in (b). The data show that during the merging process, a rapid increase in wavelength is accompanied by a rapid decrease in the ratio of amplitude to wavelength, which allows the subsequent instability growth to remain closer to the "linear theory", albeit with a smaller growth rate when compared to the linear growth rate of the smaller wavelength (e.g., see Equation (2.1)).

Using these data, the mechanism for the *persistence* of exponential growth may be understood as follows. The linear perturbation theory is characterized by exponential growth in perturbations where the ratio of instability amplitude to wavelength is small. This is because upon linearization, higher order terms may be neglected in order to solve for the dispersion relation. When the amplitude is no longer small, these terms cannot be ignored and a non-linear solution must be obtained. In Figure 4.7(a), we plot the ratio of instability amplitude to wavelength as a function of time (using values for the left side of the liner only). Before the merging process ($t < 266$ ns), this ratio increases to ~35%. At this point, the growth of these modes has saturated (i.e., initiated non-linear growth); however, this saturation does not last long due to the merging of instability structures. During this process, the amplitude remains nearly unchanged, but because the wavelength rapidly *increases*, the ratio of amplitude to wavelength rapidly *decreases*, so that the linear theory becomes applicable again. After this point ($t > 286$ ns), the wavelength remains constant, but the amplitude continues to grow exponentially until it reaches the saturation value ($A/\lambda \sim 35\%$, where A is the instability amplitude). After this time, we predict that: (1) non-linear growth would ensue and/or (2) an additional merging would occur, subsequently re-enabling linear growth.

We envision the following mechanism for the *process* of mode merging. As smaller features of wavelength $\lambda_1 = 0.8$ mm saturate in instability growth, they provide a seed for the larger wavelength instability mode with $\lambda_2 = 1.5$ mm $\sim 2\lambda_1$. This can be seen by examining the power spectrum before and after merging, as shown in Figure 4.8 (determined from the fast-Fourier transform). Both spectra show strong values at λ_1 and λ_2, however, the largest component for the $t = 266$ ns spectrum is at the smaller wavelength, while the largest component for the $t = 296$ ns spectrum is at the larger wavelength. *This indicates that the smaller wavelength λ_1 mode is cannibalized by the larger wavelength λ_2, which subsequently develops.*

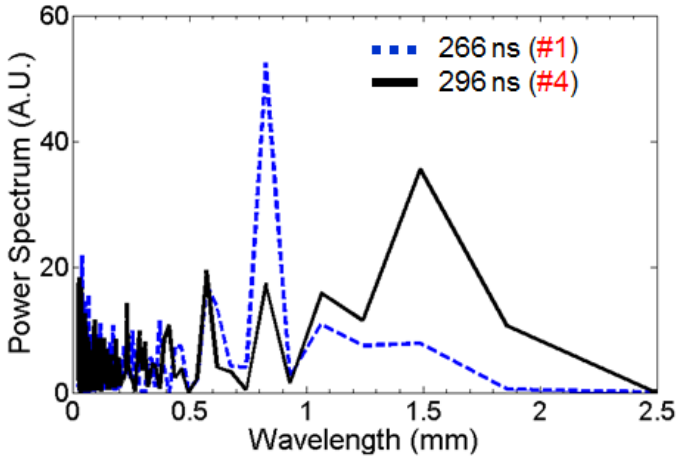

Figure 4.8. Power spectrum of wavelengths determined using an FFT algorithm for shot 1189 (B_z = 0 T, left boundary only) for t = 266 ns (blue, data point #1 in Figure 4.7) and for t = 296 ns (black, data point #4 in Figure 4.7). Both spectra show peaks at λ = 0.8 mm and λ = 1.5 mm, with the dominant peak shifting from λ = 0.8 mm at t = 266 ns to λ = 1.5 mm at t = 296 ns.

C. Plasma Expansion

During the imaging time period, the plasma expanded throughout the discharge with an approximately constant velocity, as indicated by the plot of mean radius versus time, shown in Figure 4.4(c-d). For each shot, the entire dataset was fit using a linear regression with uncertainties estimated by the standard error. These results are summarized in Table 4.1 and indicate that the plasma-vacuum interface acceleration, and therefore MRT growth (defined in this thesis as acceleration-driven) was likely to be small. Using the self-emission-only diagnostic enabled analysis of the plasma radius over a much longer window in time (~100 ns to ~500 ns), when compared to the shadowgraphy diagnostic. The data in Figure 4.4(d) show that early in time (t < 125-150 ns) the radius has a small parabolic expansion, corresponding to a positive radial acceleration and thus an MRT-stable interface, which could potentially be responsible for the observed reduction in instability growth: for t = 100-175 ns, the instability amplitude did not grow significantly. On the other hand, if these early-time structures are the result of an additional instability mechanism (such as the electrothermal instability), this

apparent zero-growth region could be due to the inclusion of the exponentially decaying term, which changes the instability amplitude relation from exp[γt] to cosh[γt] (see Ref. [SIN11]).

Shot 1215 showed the strongest deviation from the constant-velocity expansion, starting later in time around 325 ns (Figure 4.4(d)). This was accompanied by a reduction in the instability growth rate, as seen in Figure 4.4(b). A possible explanation is that, after a short period of deceleration from t = 325 ns to 350 ns (corresponding to an MRT-unstable interface), the interface obtained an outward acceleration for t > 350 ns (corresponding to an MRT-stable interface) which results in a reduction, and possibly complete stabilization, of the MRT-sausage coupled growth rate. The reason for this interface acceleration is not completely understood, but may be due to arcing in the transmission line, which could cause changes the plasma-magnetic field pressure balance. The situation is further complicated by an apparent failure in the B-dots around 375 ns, where the current departs from its sinusoidal shape (Figure 4.2). This corresponds to a shorting of the B-dot signal (the B-dots measure the time derivative of the current; if the B-dot signal is zero then a constant-value current trace will result). The current measurements could be improved by using magnetic field probes situated near the plasma (e.g. a Rogowski coil inside the return current can, or micro B-dots positioned near the liner) to measure the liner current, as opposed to current in the transmission line at a radius of 44 cm from the load center. Perhaps the best solutions to these problems are to: (1) limit the plasma analysis to early times, or (2) use a smaller radius support structure, which would increase instability growth rate because of the smaller plasma radius and larger azimuthal magnetic field.

Previously, we proposed that the axial magnetic field may be delaying or reducing the plasma expansion early in the current pulse, when the axial magnetic field is appreciable compared to the azimuthal magnetic field [YAG16a]. This was because the data (shot 1189 and shot 1190 in Figure 4.4(c)) showed that the plasma radius was slightly smaller when adding an axial magnetic field, while having little effect on the expansion rate. However, this effect was not reproducible; in fact, in subsequent

experiments the plasma seemed to expand at approximately the same rate and with the same radius, independent of the axial magnetic field value used. A more likely explanation is jitter in the shot timings (the framing camera has an inherent ~5 ns jitter) and in identifying the start time of the current pulse. These combined effects could potentially shift the entire shot 1189 dataset to a later time, moving it closer to the other datasets. This timing uncertainty could also explain why the shot 1214 data appeared to have a larger radius than all other shots in Figure 4.4(d).

D. Azimuthal Mode Numbers

The azimuthal mode number was studied by analyzing the self-emission striations and their relationship to the instability bumps, as shown in Figure 4.9 and Figure 4.10. For these images, the central region was contrast-enhanced and overlaid on the original image. The locations of the dark striations (which connect instability bumps) were then determined using an algorithm that tracked self-emission minima across the face of the plasma. Pixel values in the image were locally averaged over 10-20 pixels to avoid tracking small feature noise. The positions of these minima are tracked horizontally across the plasma, moving pixel-by-pixel, and are marked in white in Figure 4.9 and Figure 4.10. Due to the weak signal, not all of the striations could be tracked completely across the plasma; the top striation in Figure 4.10(a,b), for example, could only be tracked across one fourth of the liner circumference.

Once the measured self-emission minima are determined, their signal may be compared to the signal expected from an $|m| = 0$, 1, or 2 mode. In order for a signal to agree with the projection of a helical mode, the bump-to-bump projection requires that the pitch angle with respect to the horizontal is the same for the front and back sides of the plasma, where the front side represents the side of the plasma facing the ICCD framing camera. For these projections, solid lines indicate the required projections on the front side of the plasma, and dashed lines (for helical modes) show the required connection on the back side to generate the projected mode.

In Figure 4.9, the $B_z = 0$ T self-emission minima are compared to the projection from the $m = 0$ mode, showing overall agreement, indicating the observed mode is the $m = 0$ sausage mode. In Figure 4.10(a), the self-emission minima are first compared to the $m = +1$ mode, marked in red in the image. This mode corresponds to a single plasma helix. On the front side of the plasma, we see that the projections (solid red lines) agree with the measured self-emission minima. To complete the single helix on the back side of the plasma, bump #2 must connect to bump #3, bump #4 must connect to bump #5, and so forth. However, these connections violate the requirement that the pitch angle on the front and back sides of the plasma is conserved; the striations on the back side have a helical pitch angle of nearly zero degrees, which do not agree with the tilted striations on the front side. Therefore, this mode is rejected. The self-emission minima are then compared to the $m = +2$ mode, as shown in Figure 4.10(b), which corresponds to two intertwined helical structures; these are marked in green and black in the image. Here again, the striations on the front side of the plasma agree with the projections. On the back side, we see that the conservation requirement has been satisfied; the dashed lines have nearly identical helical pitch angles to the pitch angles on the front side. Therefore, we interpret this structure as the $m = +2$ helical mode. Once more, we emphasize that for these data we do not have a simultaneous measurement of self-emission on the back face of the plasma, this identification of the $m = +2$ mode comes from careful consideration that: (1) striations connect bump-to-bump features on the back face of the plasma, and (2) the angles of the measured striations on the front side of the plasma are similar to those on the back side.

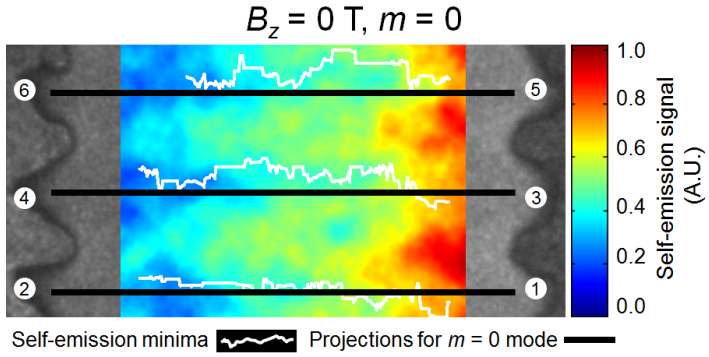

Figure 4.9. Contrast enhanced, false color image of shot 1189 (B_z = 0 T, t = 336 ns) showing the agreement between the projection of the m = 0 mode and the self-emission minima (white lines).

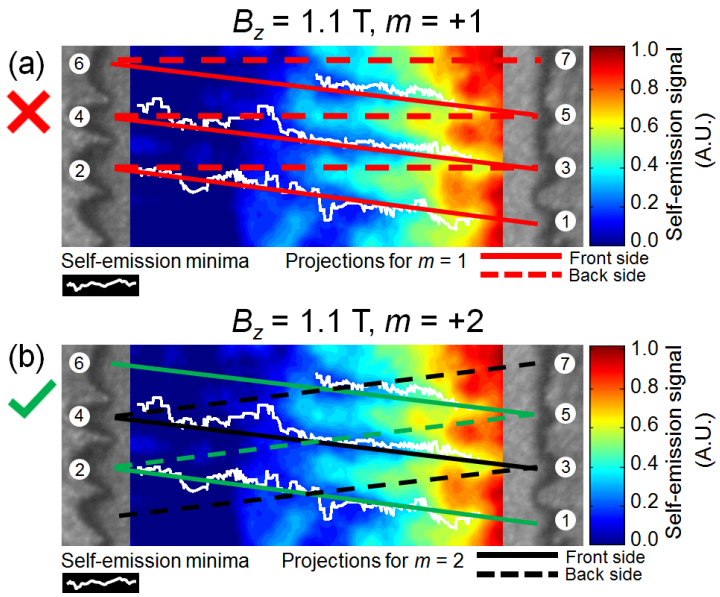

Figure 4.10. Contrast enhanced, false color image of shot 1190 (B_z = 1.1 T, t = 314 ns) showing (a) the disagreement between the projection of the m = +1 mode (red lines) and the self-emission minima (white lines) and (b) the agreement between the projection of the m = +2 mode (green and black lines) and the self-emission minima. For (a), the m = + 1 projection does not satisfy the requirement that the striation angles be conserved on the front and back sides of the plasma (the pitch angle on the back side of the plasma is nearly zero).

To conclude this section, we discuss the implications of the merging of instability structures for helical modes. Previously, we have seen that mode merging enables the $m = 0$ sausage mode to continue growing in an exponential regime. For helical modes, the merging of instability structures has an additional subtle, yet very important consequence. Consider a plasma that has developed an instability with azimuthal mode number $m = 6$ and axial wavelength $\lambda = 0.2$ mm. This corresponds to 6 intertwined helices where the spacing of adjacent bumps is 0.2 mm. Suppose this mode saturates, and adjacent helices merge in pairs to generate a longer wavelength structure of $\lambda = 0.4$ mm. Since each of the six helices has merged with an adjacent helix, the new structure consists of three intertwined helices, e.g. the $m = 3$ mode. Note that the pitch angle of the helix, m/kR, remains the same after the merging, as both m and k are reduced by a factor of two. Furthermore, we conjecture that this process does not require an even mode number; for example, the $m = 3$ mode above may further evolve so that two of the helices merge and one helix does not, or all three helices merge to form a single helix. Note that this type of argument may be applied to any helical mode with $m > 1$; however, a single helix cannot merge into a sausage instability structure without extreme deformation of the global plasma.

In Figure 4.10(b), we have seen that once the helical striations are detectable, the $m = +2$ mode was identified. By enlarging a small region of the image, we may compare the structure at $t = 254$ ns that generated the $m = +2$ structure at $t = 314$ ns. This was done in Figure 4.11, which shows four bumps merging into two bumps; since the latter was identified as the $m = +2$ mode, this gives evidence that the early time structures ($t < 254$ ns) were the $m = +4$ mode. As we shall see below in Section 4.1.4, the $m = +4$ mode has the largest growth rate at $t = 125$ ns, when the instability structures first begin to grow.

A possible caveat to this interpretation is that the $m = +4$ mode is not clearly identified by 254 ns (Figure 4.1(b) and Figure 4.11(a)). Due to the lack of self-emission striations, the small wavelength instability features cannot be connected across the face of the plasma. An alternative interpretation is that by 254 ns, the general form of the $m = +4$ mode has developed: the instability bumps have developed in a tilted pattern, but have

not linked completely in the azimuthal direction. By 314 ns, the dominant m = +2 mode links these incomplete helix-like structures to generate two intertwined helices.

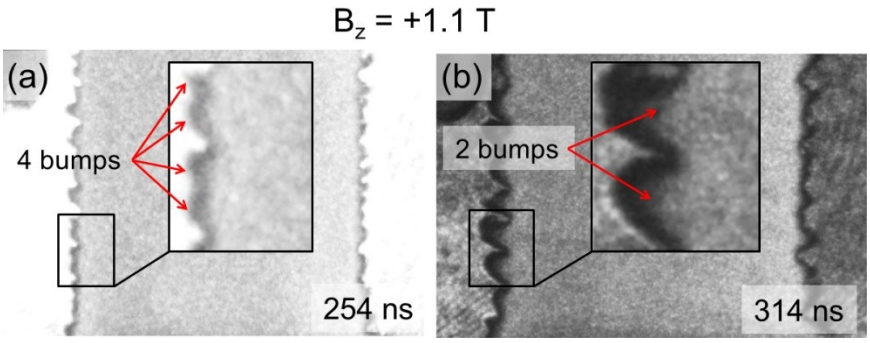

Figure 4.11. Evidence of helical mode merging for shot 1190. The boxed regions show 4 bumps at 254 ns (a) that merge to form 2 bumps at 314 ns (b). This may be interpreted as the m = +4 mode merging to generate the m = +2 mode. However, while the m = +2 mode may be identified using self-emission structures, the m = +4 mode cannot due to a low signal-to-noise ratio.

4.1.3 HYDRA Simulations

A. Problem Setup

The arbitrary Lagrangian-Eulerian fluid code HYDRA [MAR01, KON09] was used to model non-imploding liners via the resistive magneto-hydrodynamics package. The simulation was performed in cylindrical geometry, using 1-D in order to solve for the equilibrium profiles. The 400 nm-thick aluminum liner and inner rod were discretized into 200 and 50 zones, respectively. In attempt to realistically model the phase transitions of the materials, the equation of state, electrical conductivity, and thermal conductivity were incorporated using the SESAME tables [SES17]. To maintain reasonable simulation times (~3 hours), the inner rod material was set to aluminum with high resistivity, $\eta = 10^{13}$ ohm-cm (the EOS and thermal conductivity were still allowed to vary using the SESAME tables). This prevented the rod from carrying current, but enabled kinetic and magnetic pressure to develop between the foil and the inner rod, preventing an implosion

and resulting in a net outward motion of the foil. The foil was offset from the rod using three distances that covered the range of experimental values: 1 μm, 50 μm, and 100 μm. The offset is due to the conducting aluminum tape on the support structure end caps, which in the experiments is wrapped directly around the plastic rod and results in a maximum offset of 100 μm (equal to the thickness of the aluminum tape).

The current was driven by varying the magnetic field at the outer radius of the simulation boundary, using the LTD current pulse shape (base-to-peak risetime of 220 ns). The peak current was varied from 480 kA to 570 kA in order to capture possible current losses in the transmission line. As the magnetic field varies in time at the edge of the simulation, it must diffuse through the resistive aluminum, generating current in the axial direction. This induced current ultimately results in heating and ablation of the foil material.

Future simulations could be improved by incorporating the plastic EOS and conductivities for the inner material. An attempt was made; however, the simulation ran for 42 hours and reached 60 ns simulation time. Future simulations could identify the troublesome zones that caused this. During the 60 ns, it appeared that shocks and rarefactions were generated in the plastic rod and that the foil did not ablate (it remained at a thickness of roughly 400 nm).

B. Simulation Results

Figure 4.12 shows a plot of the plasma radius at a density of $n_{sim} = 10^{19}/cm^3$ for a variety of currents and offsets, identified in the figure. This value was found using an algorithm that searched for the condition $n > n_{sim}$, moving zone-by-zone from the outer boundary. This density was chosen in order to match the interferometry measurement of electron density at the edge of the liner, so that $n_{exp} = n_{sim}$. These plots were smoothed in order to reduce the abrupt changes in the plasma radius due to shocks, rarefactions, and ablated material in order to capture the overall expansion of the liner-plasma.

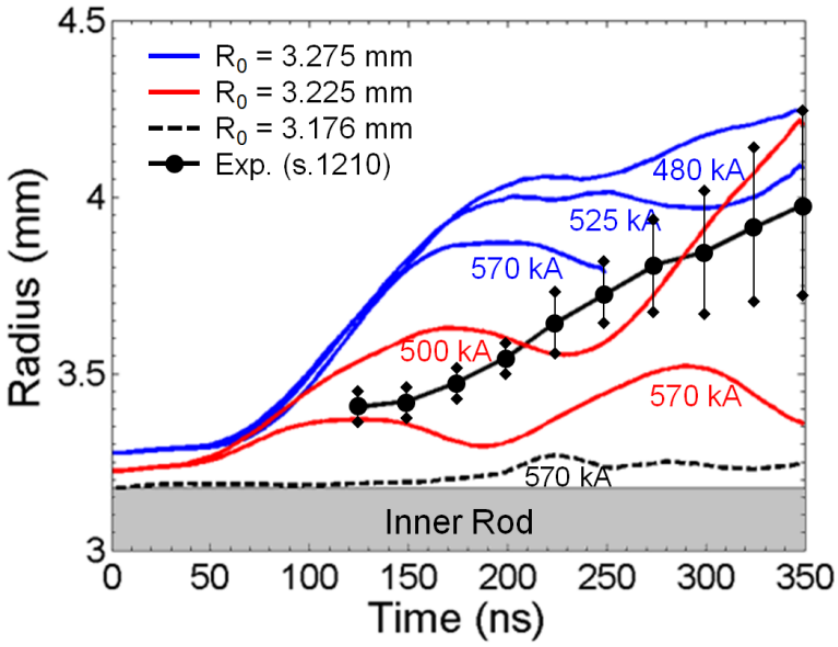

Figure 4.12. Simulated plasma radius (HYDRA) determined using the outer plasma radius that corresponds to a density of $10^{19}/cm^3$, for various initial foil radii and peak currents. The simulated radii are compared to the experimental data. Uncertainties in experimental data are calculated using the standard deviation of the plasma boundary.

The largest offset (100 μm, blue) tended to show the largest expansion. Early in time, the expansion showed a roughly constant velocity. Later in time, however, the radius showed a deceleration as the magnetic pressure became large. This deceleration was not readily observed in the experiment (black data), although the experiment does demonstrate small variations from a constant velocity expansion. Decreasing the offset to 50 μm resulted in a smaller radius plasma, with the larger current (570 kA) showing a smaller radius than the 500 kA simulation. Offsetting the foil 1 μm showed the plasma was not able to expand; it remained near the rod for the full simulation. This may be attributed to limitations in the simulation, where insufficient pressure builds between the foil and the rod, so that the total pressure at a larger radius than that of the bulk liner predominantly exceeds the total pressure at a smaller radius than that of the bulk liner. In addition, the rod material may play a role—if this were modeled using plastic, the rod may be able to expand, ablate, and develop pressure that lifts the liner from the surface.

Unfortunately, dielectric materials are difficult to model due to their complicated breakdown process.

Figure 4.13 shows profiles for the density, temperature, magnetic field, and current density for t = 50 ns, 100 ns, 150 ns, and 200 ns. To reduce figure clutter, only the 50 ns and 150 ns profiles are shown for Figure 4.13(d). The density profiles show that the majority of the liner remains roughly intact, expanding from 400 nm to to ~200 μm over ~200 ns. This region of the liner, which consists of a Gaussian-like density distribution with a dense core, is referred to as the "bulk" liner, and suggests the thin shell model of the Weis-Zhang-Lau analytic theory presented in Chapter 2 and utilized in Section 4.1.4, below, is applicable. This is in contrast to our initial expectation that the liner ablates and uniformly expands to form a rectangular-like density distribution to fill the gap between the observed outer radius and the inner rod. At the center of the bulk liner is a cold, ~1 eV plasma, with increased temperature (~10 eV) on the lower density edges. Figure 4.13(c) shows the azimuthal magnetic field has nearly fully diffused in the liner, with a large portion of the current flowing at a smaller radius than the bulk of the liner (Figure 4.13(d)). This was not expected when considering the skin effect, which tends to limit current to the outer radius, but may be understood by considering the vastly different electrical conductivities due to the large temperature and density variations.

Throughout the simulation, shocks and rarefaction are continuously observed as material is ablated. This is particularly evident in the Figure 4.13(d, t = 50 ns), which shows some of this very low density material ($n < 10^{18}/\text{cm}^3$) carrying current at radii larger than that of the bulk liner. The origin of the current spike at a radius of 3.9 mm is the curl of the magnetic field (Figure 4.13(c, t = 50 ns)), which arises as the magnetic field diffuses through the ablated low density mass. Typically, the ablated mass is ejected radially outward. For example, the spike at a radius 3.9 mm in Figure 4.13(d, t = 50 ns) is eventually lost to the outer simulation boundary.

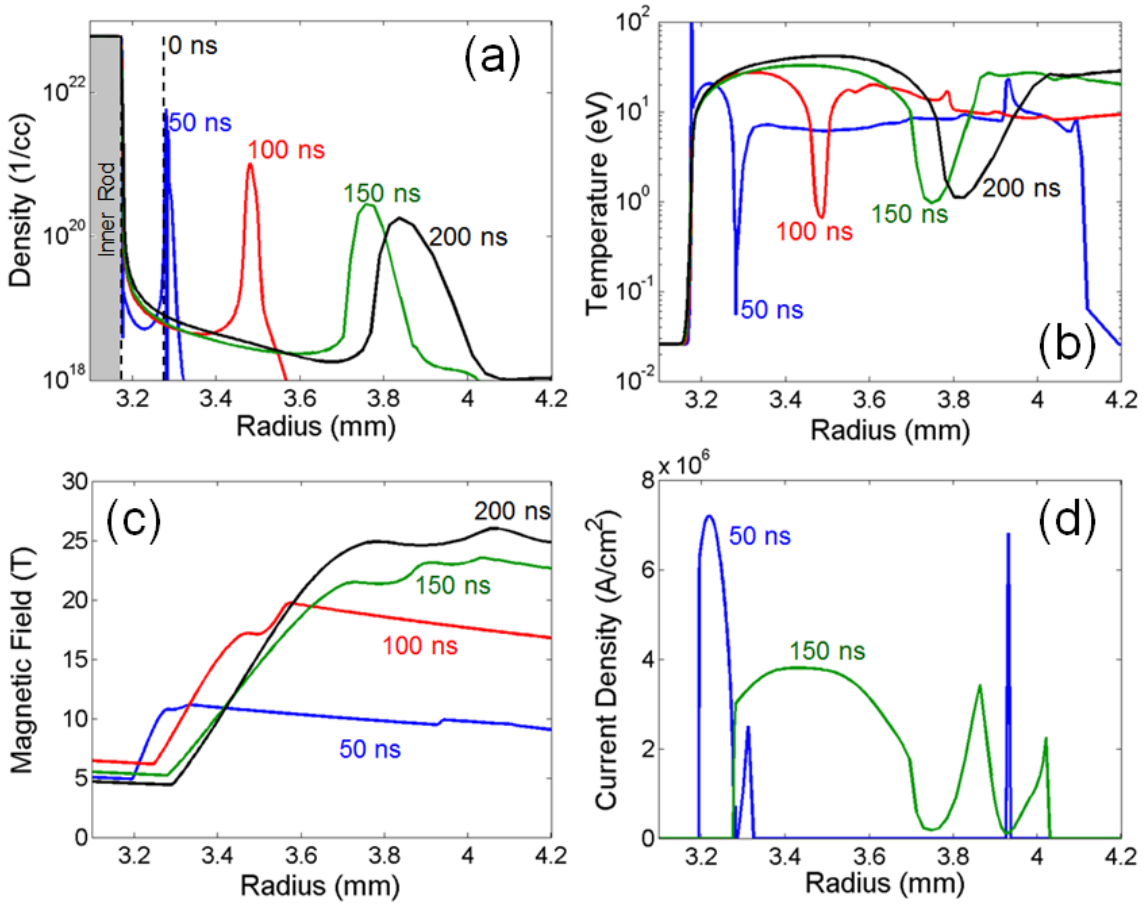

Figure 4.13. HYDRA profiles for (a) density, (b) temperature, (c) magnetic field, and (d) current density.

Figure 4.14 shows a snapshot of the total pressure (black curve), consisting of magnetic (blue curve) and kinetic (red curve) components. Inside of the bulk liner, total pressure is slightly larger than the total pressure on the outside of the liner. This pressure difference is ultimately responsible for driving the liner outward. Interestingly, the pressure in the bulk liner is lower than the pressure inside and outside, despite the bulk liner increasing in thickness. For this pressure profile, one would expect an overall compression of the liner. A possible explanation is that, for this snapshot, the fluid zones in the liner have obtained large velocity components from the ablation that occurred

earlier in time. These velocity components would be directed radially away from the center of the bulk liner.

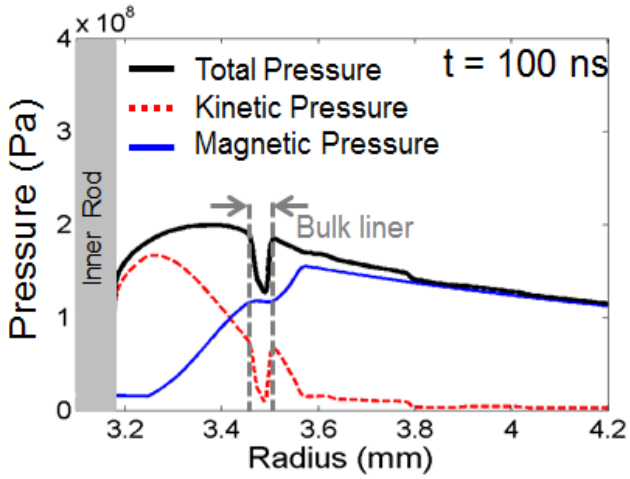

Figure 4.14. Total (black), kinetic (red), and magnetic (blue), pressure profiles for HYDRA simulation at t = 100 ns.

4.1.4 Application of Weis-Zhang-Lau Instability Theory

In order to study the development of helical modes, we used the Weis-Zhang-Lau (WZL) theory [WZL15, WEI15] to calculate the instantaneous theoretical sausage and helical growth rates using parameters measured or estimated from the experiment. While the instabilities appear to have developed beyond the direct applicability of the linear perturbation theory, we may still use the WZL theory to: (1) gain insight into the instability development early in the current pulse, and, (2) isolate the effects of axial magnetic fields for various azimuthal mode numbers.

Contour plots of the instantaneous growth rate as a function of time are presented in Figure 4.15 for azimuthal mode numbers ranging from m = -12 to m = +12. These calculations require values for the plasma radius, instability wavelength, plasma density, liner thickness, and instantaneous magnetic field. These values were either measured from the experiment or estimated using reasonable parameters. Despite the observation that the instability wavelength changes over time, its value was fixed at λ = 0.3 mm to

characterize the wavelength of instability structures that first appear. While this value could incorporate the time-changing effects observed in Section 4.1.2.B, this would primarily change the numerical values for growth rate and complicate the interpretation of the growth rate plots in Figure 4.15. Measured values include radius (fixed at 3.5 mm for ease of calculation) and magnetic field (determined from plasma radius and experimental current pulse, approximated by a sinusoidal function with 580 kA peak current and 250 ns base-to-peak risetime). The two parameters that were estimated and not directly measured were the liner thickness and plasma density; however, these parameters primarily affect the numerical scaling of the growth rate curve, shown in Figure 4.16. Figure 4.16(a-b) shows the effects of varying the plasma density over a range of 10^{18}/cm^3 to 10^{21}/cm^3, and Figure 4.16(c-d) shows the effects of varying the plasma thickness from 1 μm to 1 mm. The importance of these plots (beyond demonstrating the scaling of growth rate on density and thickness) is to show that using the true experimental density and thickness would only change the numerical value of the growth rates in Figure 4.15, and not their relative values for a given time. This important conclusion enables the various instability modes to be roughly compared when highly resolved measurements of the plasma density and liner thickness are unavailable.

Reasonable values for the plasma density and liner thickness were chosen as follows. The plasma thickness may be estimated from the difference between the plasma and support structure radius, which ranges from 0.6 – 1.3 mm. An additional estimate may be obtained from HYDRA (Figure 4.13(a)) which shows the liner thickness (Δ) expanding to ~200 μm over 200 ns. As the growth rates are extremely insensitive to liner thicknesses exceeding 0.1 mm (Figure 4.16 shows the Δ = 0.1 mm and Δ = 1 mm curves overlap), we set the thickness to 0.2 mm to characterize this range of thickness. For the plasma density, experiments on MAIZE using the same foils (in an imploding geometry, see Chapter 5) measured an electron density of $n_e \sim 10^{19}$/cm^3 at the edge of the plasma using interferometry. A second estimate for the plasma density may be determined by assuming the dark shadowgraph band is due to laser cutoff at the critical density, ~$4 \cdot 10^{21}$/ cm^3. Finally, HYDRA (Figure 4.13(a)) shows peak densities at the liner core

ranging from 10^{20}/cm^{3}to 10^{21}/cm^3, with densities at the edge of the bulk liner dropping to ~10^{18}/cm^3. Therefore, a reasonable density characterizing this range is $n \sim 10^{20}$/cm^3, corresponding to a mass density of $\rho = 4.5$ kg/m^3.

Figure 4.15 shows a plot of the analytic growth rate as a function of time for mode numbers of $m = -12$ to $m = +12$ for (a) $B_z = 0$ T and (b) $B_z = 1.1$ T. When there is no axial magnetic field, the dominant mode is the $m = 0$ sausage mode for all times, and the negative m modes have the same growth rate as the positive m modes. For these plots, recall that a positive m mode indicates a helix with spiral direction in the same sense as the global magnetic field spiral. These results are intuitively expected because the $m = 0$ mode requires no bending of the azimuthal magnetic field (even the $m = 1$ mode must bend the azimuthal field to develop), and because, in the absence of an axial magnetic field, a plasma helix spiraling up or down experiences the same magnetic tension. From this plot, we would expect the $m = 0$ mode to dominate, which was indeed the mode observed in the experimental images in Figure 4.1(a, d).

Figure 4.15(b) shows the dramatic effect of adding a relatively small axial magnetic field of 1.1 T (the peak azimuthal field for these calculations was 33 T). First, the regions of high growth rate shift to positive m modes; an intuitive consequence as these modes have a smaller magnetic tension when compared to their negative counterparts. We also see that there is a region of complete stability, where all azimuthal modes are stable for $t < 45$ ns. At $t = 46$ ns, the $m = +8$ and +9 modes are the first to destabilize. Interestingly, these modes destabilize before even higher order modes with $m > +9$. As determined in the experiment, the first detectable instability bumps are observed around ~120 ns. Using Figure 4.15(b), we see that at $t = 120$ ns, the $m = +4$ mode has the largest growth rate. Assuming that at $t = 120$ ns the MHD modes may develop, we would expect the $m = +4$ mode to dominate.

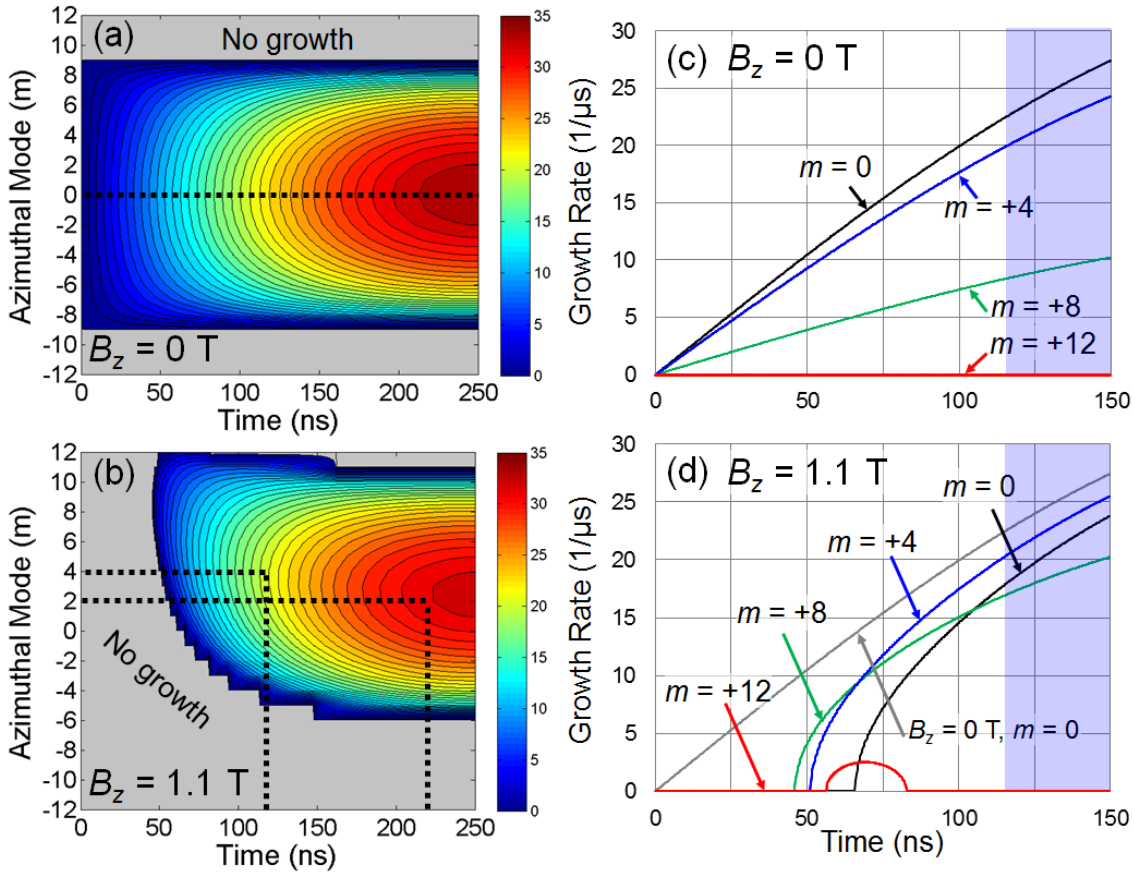

Figure 4.15. (a-b) Weis-Zhang-Lau analytic instability growth rate calculations for small wavelength perturbations (λ = 0.3 mm) for (a) B_z = 0 T and (b) B_z = 1.1 T. These calculations used a typical current pulse (580 kA peak current, 250 ns base-to-peak risetime), liner thickness of Δ = 200 μm and plasma density of $n = 10^{20}/\text{cm}^3$. The plot in (b) shows a region in time where all modes are stable. As time progresses, higher order modes de-stabilize. In (c-d), lineouts for various mode numbers are given for the early part of pulse (t < 150 ns) for (c) B_z = 0 T and (d) B_z = 1.1 T. The blue region shows the approximate time when instability bumps are first detected and begin to grow. In (c) the m = 0 sausage mode is always the most unstable. In (d), while the m = +8 is the first mode to destabilize, the m = +4 mode has the highest growth rate at t = 120 ns (when instability bumps are first resolvable), indicating this mode should develop first. To exclude coupling effects to MRT, these calculations did not include liner acceleration.

As we have seen in the experiments, the early-time instability bumps for the magnetized liners merge into a longer wavelength structure (see Figure 4.11). This merging of bumps (assuming well-defined helical modes) is necessarily accompanied by a reduction in azimuthal mode number. For example; the m = +4 mode consists of four intertwined helices; two adjacent bumps merging corresponds to two adjacent helices merging. Thus, if each bump merges with an adjacent bump, we would expect an m = +4 mode to convert to an m = +2 mode. Using the analysis in Section 4.1.2.D, the existence of the m = +2 mode was indeed confirmed. Looking even earlier in time and using Figure 4.15(b), it is possible that the m = +8 mode first arises at t = 46 ns and has already merged into the m = +4 mode by t = 120 ns, when instability bumps are first detectable. Looking much later in time (after the imaging window), if the m = +2 mode instability bumps saturate and merge, then the m = +1 mode would arise. In this scenario, the traditional kink mode (m = 1) will represent the final state of the non-axisymmetric modes. This predicted effect of an azimuthal mode number cascade is a direct result of instability saturation and merging. Note that this analysis neglects the contribution of the early time electrothermal instability (ETI) [PET12, PET13, PET14, ORE08, ROU08, STE16], which may set an initial value for the axial wavelength of the MHD modes. The effects of an applied axial magnetic field on the electrothermal instability are not completely understood; whether the incorporation of a pre-imposed axial magnetic field results in angled ETI striations (thus providing a seed to helical modes) remains an outstanding question.

Figure 4.15(c) and (d) show lineouts taken from specific modes in Figure 4.15(a) and (b). The purpose of these plots is to illuminate more subtle features not readily observed in the contour plots in Figure 4.15(a) and (b). For example, Figure 4.15(c) shows the relative strength of the growth rates for the m = 0, +4, +8, and +12 modes for B_z = 0 T. In Figure 4.15(d), the growth rate for these modes are computed for B_z = 1.1 T and compared to the B_z = 0 T, m = 0 mode. This comparison shows that even the mode with the highest growth rate for the magnetized liner has a smaller growth rate than the

unmagnetized liner; this was experimentally verified for early times in Figure 4.5 and Table 4.1.

Making a numerical comparison of the theoretical growth rate to the experimentally measured values is difficult because we do not have a measurement of the plasma density (thickness is rather insensitive, therefore the limiting factor is density). Despite this, we do see that early in time (t = 120 - 225) the ratio of experimental growth rates for B_z = 0 T to B_z = 1.1 T is (10.8±0.5)/(9.9±0.7) = 1.1±0.1. The theoretical ratio of growth rates for B_z = 0 T (m = 0) and B_z = 1.1 T (m = +4) at t = 150 ns was 27.3/25.3=1.08. Note that this small predicted decrease in growth rate was on the threshold of being experimentally detectable.

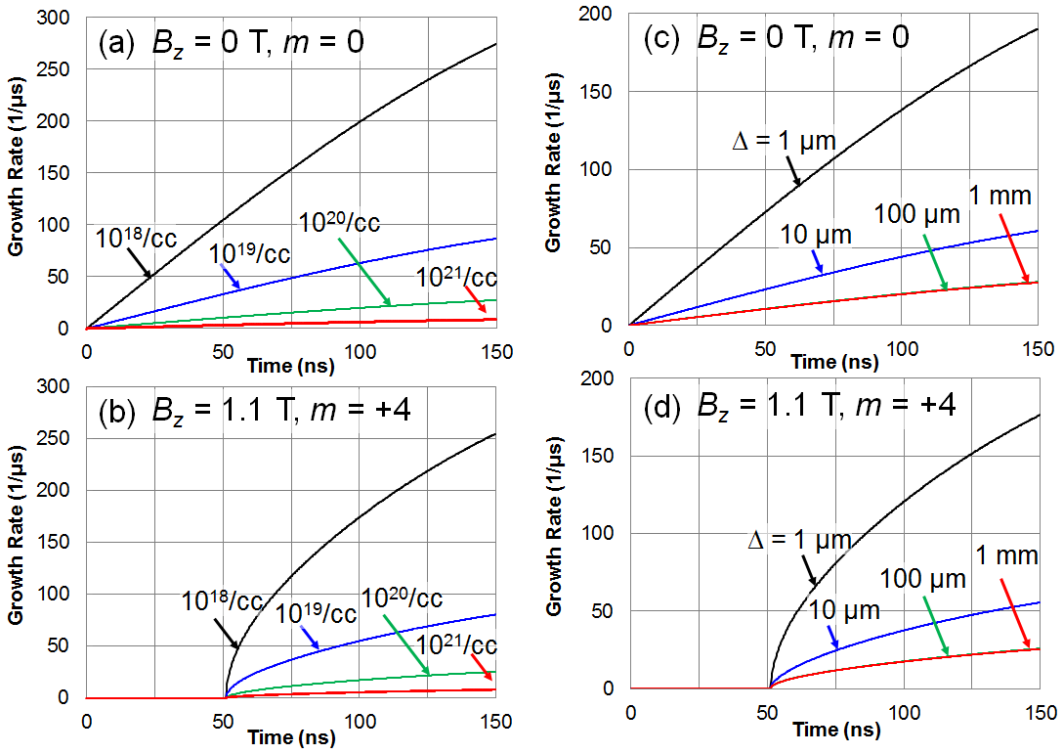

Figure 4.16. Scaling of WZL instability growth rate with (a,b) plasma density and (c,d) liner thickness for B_z = 0 T, m = 0, and B_z = 1.1 T, m = +4. For these calculations, R = 3.5 mm, I_{max} = 580 kA, base-peak risetime = 250 ns, λ = 0.3 mm, (a-b) thickness = 200 μm, and (c-d) $n = 10^{20}/cm^3$.

Perhaps the most useful aspect of the analytic growth rates is to reveal the possible dominant modes expected for a given axial magnetic field at a fixed set of parameters. As discerned from Figure 4.16, changing the density or thickness in these calculations will not change which modes are stabilized early in time, nor the relative scaling of modes for a given axial magnetic field. Therefore, the analytic growth rates may be used as a tool to examine the dominant mode as a function of time. This powerful tool was corroborated with the experimental results presented in this chapter.

4.2 Experimental Results for Kink-seeded, Non-imploding Liners

In Section 4.1 we saw that the addition of an axial magnetic field resulted in an $m = +2$ helical mode for the unseeded liners. This made it difficult to isolate the stabilizing effects of an axial magnetic field for a given mode, as larger axial fields could induce higher m modes. This motivated the design of the $|m| = 1$ kink-seeded support structure; in this manner, the same azimuthal mode and axial wavelength could be generated in order to directly compare the effects of axial magnetic fields. We performed a series of three shots using the screw-seeded support structure (5.65 mm mean diameter, 0.8 mm peak-to-valley amplitude, 1.27 mm axial wavelength; see Figure 3.5 in Chapter 3) using three values for the axial magnetic field ($B_z = 0$, +1.6 T, -1.6 T). These magnetic fields were chosen to compare the effects of seeding to the intrinsic instability modes, and to generate the neutral ($m = 1$), positive ($m = +1$) and negative ($m = -1$) modes in order to isolate the stabilizing effects of axial magnetic fields. It was found that *the plasma seeding is much more important than the intrinsic growth rate when determining the dominant instability mode that arises.* In addition, we observed that the negative mode, which must inherently bend the external magnetic field the most in order to develop, was the most stable of the three seeded modes. The positive mode, which includes an axial magnetic field but requires less field bending than the negative mode, initially had a smaller instability amplitude but higher growth rate when compared to the neutral mode (which has no axial field). A summary of the experimental shots is presented in Table 4.2. To directly compare the instability amplitude, it is important that the current traces be nearly equal. Figure 4.17 shows that the current traces agreed within 1% at peak current and within 6% at 350 ns, indicating that the instability development may be directly compared.

Table 4.2. Summary of experimental data for non-imploding, kink-seeded liners. The growth rate and expansion velocity (V_{exp}) are measured using a linear fit. Uncertainties are estimated from standard error of fits.

Shot	B_z (T)	Mode	Growth Rate (μm/ns)	V_{exp} (μm/ns)	Image Timing (ns)
1192	0	Neutral (m = 1)	2.2±0.2	5.2±0.3	192-292
1205	-1.6	Positive (m = +1)	3.5±0.2	5.5±0.5	204-304
1193	+1.6	Negative (m = -1)	1.4±0.3	4.6±0.3	225-325

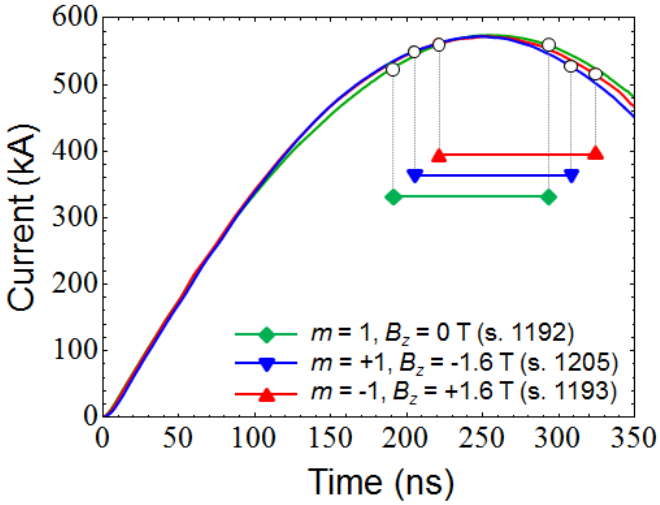

Figure 4.17. Current traces and shadowgraphy image timings for kink-seeded liners. Symbols mark start and stop time of imaging window.

4.2.1 Shadowgraphy Images

The twelve-frame shadowgraphy diagnostic enabled imaging of the kink-seeded liner plasmas over a 100 ns window. A series of images is shown in Figure 4.18, which shows the kink-seeded liners developed a helical instability structure at the seeded axial wavelength of λ = 1.27 mm, regardless of the magnetic field orientation. This indicates that the helical shape of the support structure was the dominant factor for determining the physical structure of instability, superseding the natural instability mode the plasma would develop in the absence of the seeded support (e.g. m = 0 when B_z = 0 T, m = +2 when B_z = 1.1 T). By fixing the plasma structure and varying the axial magnetic field, the

neutral, positive, and negative modes could be investigated. The shadowgraphy images in Figure 4.18 show that the axial magnetic field orientation (and therefore the sign of the mode) had an effect on the amplitude of the instabilities; an axial field of 1.6 T in the **–z** direction did not significantly change the amplitude of the structures when compared to the unmagnetized case, whereas reversing the direction of the field had a significant effect, resulting in a peak instability amplitude of nearly half the value. The helix in Figure 4.18(c), being a negative azimuthal mode, invokes more magnetic field bending and therefore reduces growth in amplitude. In general, the bright and dark self-emission striations demonstrated a higher contrast when compared to the unseeded liners; the striations for the $B_z = 0$ and $B_z = -1.6$ T liners were particularly clear, which may be attributed to their larger instability amplitudes when compared to the $B_z = +1.6$ T liner.

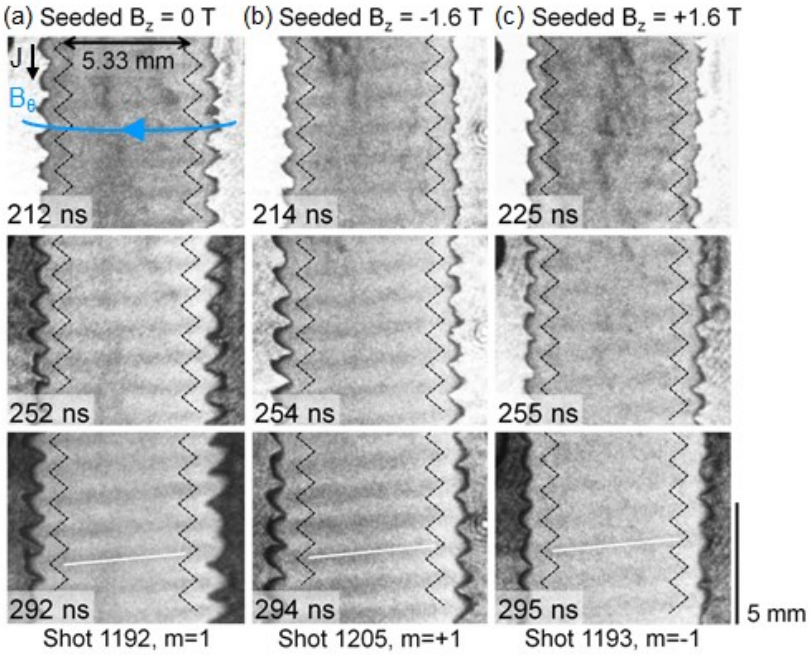

Figure 4.18. Combination shadowgraphy and self-emission (filtered at 532 nm) images for kink-seeded liners using axial magnetic field values of (a) $B_z = 0$ T, (b) -1.6 T, and (c) +1.6 T. The neutral ($m = 1$), positive ($m = +1$), and negative ($m = -1$) modes are seeded in (a), (b), and (c), respectively, where the orientation of the global magnetic field and plasma structure determine the sign of the mode. The dashed black lines indicate the approximate position of the dielectric support structure, and the solid white lines mark a sample dark striation, which connects bump-to-bump instability structures. The direction of the current density ***J*** and azimuthal magnetic field B_θ are indicated in (a).

4.2.2 Instability Experimental Analysis

The algorithm described in Section 4.1.2 and Appendix A was used to track the plasma boundary. As previously discussed, the instability amplitude A was characterized by the standard deviation σ in the radial position of the tracings using the amplitude relation for a perfect sine wave, $A = \sqrt{2}\sigma$. The radius and instability amplitude were then determined as a function of time by taking the mean of the left and right values, with uncertainties estimated using the difference between the left and right measurements. These results are presented in Figure 4.19.

The experimental data show that an axial magnetic field reduces overall instability growth early in time before peak current. For all cases, the amplitude tended to grow algebraically (as opposed to exponentially), which indicates that the observed growth had reached the nonlinear regime. The algebraic growth rate was quantified by fitting a linear regression to the linearly increasing regions of the amplitude in Figure 4.19(a). The measured growth rates are summarized in Table 4.2, where uncertainties are estimated using the standard error of the linear regression. For the data in Figure 4.19(a), the B_z = 0 and B_z = -1.6 T kink-seeded liners had instability structures that grew to nearly equal amplitudes at 270 ns. Before this time, however, the B_z = -1.6 T liner showed a reduction in instability amplitude. This demonstrates the stabilizing effects of axial magnetic fields early in time, when the ratio of the axial to azimuthal magnetic field was larger. Later in time, as this ratio decreases, the stabilizing effects on the positive mode are reduced. The negative mode (B_z = +1.6 T) showed the smallest instability structures overall and for all times, along with a saturation in growth beginning at 260 ns.

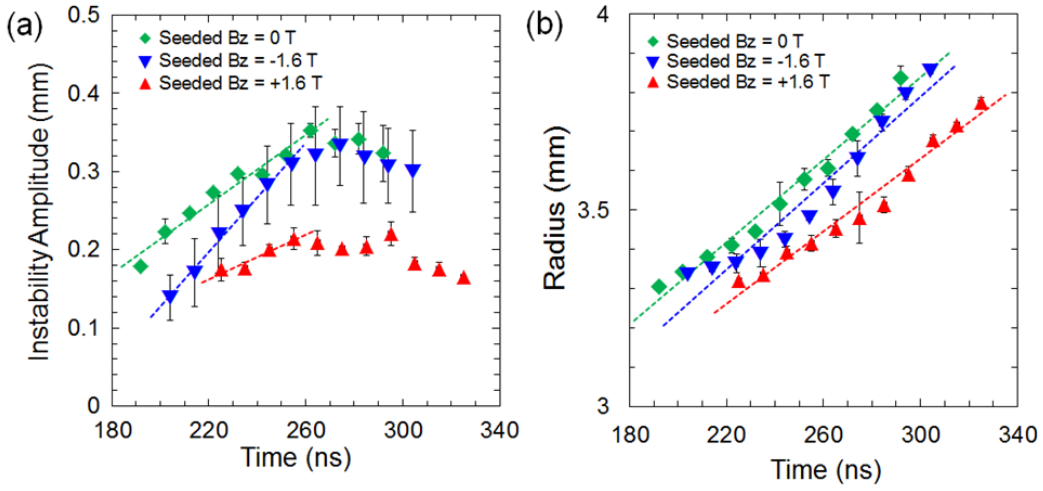

Figure 4.19. Experimental data for (a) kink-seeded instability amplitude and (b) mean plasma radius. The linear fits to the amplitude and radius are summarized in Table 4.2. To best characterize the growth rate, only the linear regions of amplitude were fit. The neutral, positive, and negative modes are represented by the green, blue, and red data, respectively.

Interestingly, it appears all modes reach a complete saturation, where the instability amplitude no longer grows (and even decreases), at approximately the same time (t = 260-270 ns). This is significant, because while the amplitude of the instability structures is different, the wavelength is the same, indicating that the ratio of amplitude to wavelength is different when comparing the neutral and positive modes to the negative mode. One would expect the negative mode to continue growing to the amplitude of the neutral and positive modes, but this was not the case. One possible scenario is that, in this highly non-linear stage, Alfven-like waves are being generated. In other words, the instability growth changes from $\sim\exp[\gamma t - ikz]$ to $\sim\exp[i\omega t - ikz]$, where γ and ω are real-valued. This corresponds to an oscillation in amplitude (at a given spatial location) and a shift in phase in the **z** direction. The experimental images in Figure 4.18(c) support this notion, as the instability peaks are displaced from their original value while maintaining the *same* amplitude, with a net wave-like motion in the –**z** direction (this is particularly evident for the right side of the liner in Figure 4.18(c), though less apparent on the left side). Even the linear theory predicts Alfven waves for sufficiently strong axial

magnetic fields, therefore, another possibility is that the axial magnetic field has somehow been enhanced (e.g. from a low density plasma surrounding the plasma that has been compressed or "pinched" about the liner during the early current rise).

The results of these experiments highlight the importance of the seeding in the excited kink mode. When the helix spiraled in the direction of the global magnetic field spiral (m = +1, Figure 4.18(b)) the instability amplitude was reduced early in time but reached the same amplitude as the unmagnetized liner by 270 ns, indicating the importance of the axial field early in time. Despite this, the growth rate was *larger* relative to the unmagnetized case, which may be understood by the following two effects: first, the axial magnetic field effects were reduced later in time as the azimuthal field peaked, and second, the growth rate was larger because the ratio of the amplitude to the wavelength was initially smaller than that of the unmagnetized case, indicating that the growth rate was perhaps closer to the linear perturbation regime (which is characterized by exponential growth in time). Inverting the direction of the axial magnetic field while maintaining the same direction of the seeded helix produced an m = -1 mode and demonstrated an overall mitigation of instability development. This dramatic difference is expected, as the helical structure was seeded with m = -1. This result demonstrates the importance of the sign of the helical mode; negative m modes are more stable because they require more energy to bend magnetic field lines. We emphasize that, despite the fact that the m = -1 mode is more stable, it still appears due to the seeding.

4.2.3 Plasma Expansion

During the imaging window, the plasma expanded throughout the discharge with an approximately constant velocity, as indicated by the plot of mean radius versus time, given in Figure 4.19(b). For each shot, the entire dataset was fit using a linear regression with uncertainties estimated by the standard error; these results are summarized in Table 4.2 and indicate that the plasma-vacuum interface acceleration, and therefore MRT growth, was likely to be small. The constant-velocity expansion assumption may be limited when considering the B_z = -1.6 T seeded liner, which underwent the most complex radial expansion. During the majority of the imaging period, the mean radius

appeared to show a small outward acceleration. This scenario is equivalent to a heavy fluid (plasma) accelerating a light fluid (magnetic field), and corresponds to an MRT-stable interface. This mildly stabilizing effect cannot overcome the intrinsic helical instability that resides in the non-imploding current carrying liner (which arose in Section 4.1).

For the seeded support structure, the initial spiral impression on the foil was negligible as the foil made minimal contact with the edges of the screw threads. During the discharge, the foil ablates and plasma fills the gaps, taking the shape of the screw pattern and therefore seeding the kink instability. In this scenario, it may be possible for regions of the foil to implode into the gaps of the support structure and develop MRT in the process. Any MRT growth would complicate the assertion that MRT is decoupled from the kink instability. However, the resulting MRT development is found to be much less important when compared to the deformation of the foil into the seeded structure. The maximum distance the mean foil interface can travel is s = 0.4 mm, equal to one half of the seeded support structure amplitude (the maximum distance a point on the foil can travel is 0.8 mm, but the *mean interface* of the resulting sinusoidal-like ripple would be displaced by 0.4 mm). For a constant acceleration, the MRT gain for a displacement s at the seeded wavelength (λ = 1.27 mm) is given by $G = \cosh[\sqrt{2ks}]$~4, where $k = 2\pi/\lambda$ is the instability wavenumber (see Appendix A in reference [WEI15]). For the foil to have obtained the maximum displacement, it must have completely deformed about the support structure, and therefore obtained a peak-to-valley amplitude of 0.8 mm in the process (equal to the support structure amplitude). For this amplitude to have been generated by MRT alone would require an initial perturbation of A_0 = 0.2 mm, which is unreasonable for two reasons: (1) we do not see such a perturbation on the pre-shot images, which can clearly resolve features exceeding 0.1 mm, and, (2) when the experimental images were taken (t > 200 ns, see Figure 4.19) we do not see an instability amplitude of 0.8 mm, but rather of A_1 ~ 0.2 mm. On the other hand, let us suppose that the amplitude A_1 at t ~ 200 ns was generated by MRT alone. This requires an initial

perturbation of A_0 = 0.05 mm (for G = 4); but again, in order for a displacement of s = 0.4 mm have occurred, the foil must have taken the shape of the seeded support structure, and in the process gained an amplitude of 0.8 mm, which is large compared to A_1. We therefore conclude that MRT plays little role during any initial implosion of the foil towards the support structure, and that the dominant instability development throughout the discharge is due to the kink instability.

4.2.4 Application of Weis-Zhang-Lau Instability Theory

In order to study the development of helical modes, we used the Weis-Zhang-Lau theory [WZL15] to calculate the instantaneous theoretical helical growth rates using parameters determined from the experiment (see Section 4.1.4). The result of these calculations are shown in Figure 4.20, where we compare the growth rate of the $m = \pm 1$ kink instability for axial fields of B_z = 0 T and B_z = 1.6 T using the seeded wavelength of 1.27 mm. This plot shows that the m = -1 mode is completely stabilized for 70 ns, and after this point has a reduced growth rate for the remainder of the pulse. The m = +1 mode is stabilized for a shorter period of time (50 ns), after which its growth quickly approaches the unmagnetized case. These calculations are consistent with the experimental observations that demonstrated that: (1) the m = -1 seeded liner had most stable structures, while the m = +1 seeded liner showed initially smaller structures that grew to amplitudes comparable to those in the m = 1 unmagnetized liner, and (2) the seeding is more important than the intrinsic instability for the appearance of the mode.

Similar to the discussion in Section 4.1.4, we note that the theoretical growth rate values should not be directly compared to the experimental values. However, we may still use the Weis-Zhang-Lau theory to study the overall trends and qualitative behavior of the stabilizing effects of axial magnetic fields. We can do this for the neutral, positive, and negative modes while holding all other parameters constant. These curves show the importance of the time varying ratio of axial to azimuthal field; initially it is large but later in time it is drastically reduced. Despite this reduction, the negative mode still has the smallest growth rate, indicating that the plasma structure and its relationship to the

external magnetic field must be accounted for when determining the growth of a particular mode.

Future work could investigate the development of seeded modes by looking earlier in time, in order to compare the ratios of exponential instability growth rates for the neutral, positive, and negative modes. These experiments could use 3-D printed support structures with higher order modes (such as $m = 2, 3\ldots$) while keeping the wavelength constant. This would enable an investigation of the differences between the various instability modes and further corroborate the analytic theory.

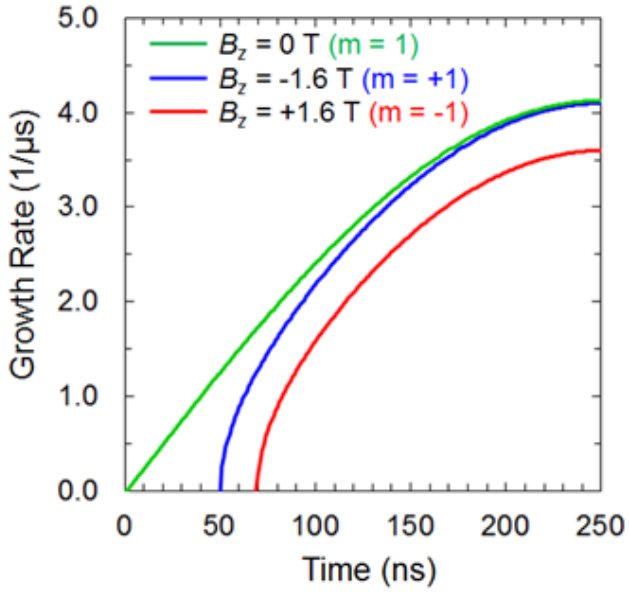

Figure 4.20. Weis-Zhang-Lau analytic instability growth rate calculations for seeded wavelength (λ = 1.27 mm) and neutral (m = 1), positive (m = +1), and negative (m = -1) azimuthal modes. Exponential growth rates are limited to linear perturbation theory and were calculated using known time-dependent experimental parameters (magnetic fields) and estimated parameters (liner thickness and density, estimated to be 500 μm and 4.5 kg/m^3). The growth rate is insensitive to thickness and scales with density as $\sim\rho^{1/2}$ so that a variation in these parameters will not change the relative amplitude of these curves for a given time. To exclude coupling effects to MRT, these calculations did not include liner acceleration.

CHAPTER 5
EXPERIMENTAL RESULTS FOR IMPLODING LINERS

In the previous chapter, the current-driven sausage and helical modes were investigated in the absence of the magneto Rayleigh-Taylor (MRT) instability by utilizing a non-imploding geometry. In this chapter, an imploding geometry is used to investigate the coupling of the MRT instability to the sausage and kink instabilities. This is accomplished by reducing the diameter of the central portion of the dielectric support structure, which enables the plasma to implode across the resulting gap. As plasma stagnates on the reduced-diameter portion of the rod, the acceleration vector switches direction and eventually plasma is exploded radially outward. Therefore, the plasma structures that develop may be investigated under a variety of dynamics: non-imploding phase ($\mathbf{a} \sim 0$, $\mathbf{v} \sim 0$), implosion ($\mathbf{v} < 0$), stagnation ($\mathbf{a} > 0$, $\mathbf{v} < 0$), and explosion ($\mathbf{v} > 0$), where **a** and **v** are the acceleration and velocity vectors of the plasma-vacuum interface in the radial direction.

A particularly important question which is until now unexplored is whether, once a helical structure has developed during the non-imploding phase, it will persist during the vastly differing dynamics that occur during implosion, stagnation, and explosion stages. For the non-imploding liners of Chapter 4, it was found that both the seeded and unseeded helical structures persisted despite the orientation and magnitude of the applied axial magnetic field. In this chapter, we find that the helical structures generated early in time, when the liner acceleration and velocity are small (similar to the early-time non-imploding dynamics of the liners in Chapter 4), do in fact persist during the implosion, stagnation, and explosion stages, irrespective of the dynamics of the global magnetic field. An important consequence is that the helical pitch angle follows the simple geometric equation $\phi = m/kR$ for all stages of the discharge, where m, k, and R are the

azimuthal mode number, axial wavenumber, and radius of the helical instability. That is, the helical structure is a manifestation of discrete eigenmodes.

The observation that the helical modes persisted motivated the systematic investigation of the effects of the applied axial magnetic field on the azimuthal mode number, which may be found by re-arranging the above equation so that $m = \phi \cdot kR$. With no axial magnetic field, the $m = 0$ mode dominated. By applying an axial field, two important effects were discovered: (1) two dominant modes may co-exist (e.g., the $m = 0$ and $m = 1$ modes may develop and persist in different axial portions of the liner) and, (2) the azimuthal mode number progressively increases with the value of the applied axial magnetic field.

This chapter is divided into three sections. Section 5.1 discusses the implosion dynamics of the liner-plasma, using the original (non-magnetized) experimental hardware discussed in Chapter 3. This set of experiments demonstrated it is possible to implode an initially solid liner in cylindrical geometry with a sub-megaampere current by using a dumbbell shaped support structure. In Section 5.2, the effects of axial magnetic fields were investigated by modifying the experimental hardware to enable the use of Helmholtz coils. For these experiments, the fast framing camera was employed (in addition to the laser backlighter) to observe self-emission features on the surface of the liner-plasma. This enabled the azimuthal mode number to be identified. In Section 5.3, the Weis-Zhang-Lau analytic theory for calculating instantaneous instability growth rates in a conducting liner-plasma is used to corroborate the results of Section 5.2. To accomplish this, the effects of the liner-plasma acceleration were included.

5.1 Implosion Dynamics

In this section we analyze the dynamics of the cylindrical liner-plasmas in an imploding geometry. Three shots were performed in order to demonstrate that it is possible to implode an initially solid liner using a sub-megaampere current pulse. The main diagnostic was the 532 nm laser beam, split temporally (20 ns) and spatially into four beam paths that intersected the load on the same horizontal plane at 1.3° $\pm$ 0.2° intervals, as shown in Chapter 3 (Figure 3.6). This set of experiments was the first to be performed for the work of this thesis, and therefore did not utilize the fast-framing camera to obtain 12 images per shot. It did, however, include a shearing interferometer on one of the beam paths, which enabled simultaneous shadowgraphy and interferometry of the liner-plasma.

The surface of the foil was characterized using an atomic force microscope (AFM) and showed ~300 nm tall bumps (comparable to the foil thickness) and pits extending over ~30 μm (Figure 5.1); these persisted even when applying tension to the foil and are therefore inherent to the liner surface. These features are a likely seed for early time instability growth (such as the electrothermal instability), which once developed, may seed the MRT and MHD modes [PET12, PET13, PET14].

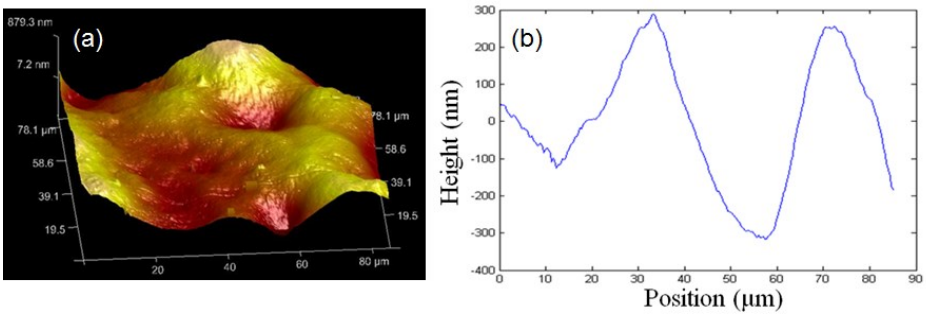

Figure 5.1. (a) AFM surface plot of 400 nm foil. (b) 2-D lineout highlighting changes in the surface topology.

The current traces for the three shots of this series are shown in Figure 5.2, which also compares the measured current to the PSpice circuit simulation for the LTD

generator [KIM09], shown in Figure 5.3. The traces are in overall agreement until nearly peak current, indicating that the constant value load-inductance estimate of 15 nH is valid until this time. After this time, the current traces fall below the predicted value, which may be understood by the inductance increase due to the imploding liner. In Steiner et al., [SYP16], this small difference was used to calculate the effective current carrying radius of an imploding cylindrical liner. For our analysis, however, the plot in Figure 5.2 is sufficient to demonstrate that the measured current traces are primarily governed by an RLC circuit, where the load resistance and any contact resistance due to the sliding support structure are minimal.

Shadowgraphs from the three unmagnetized shots are depicted in Figure 5.4 and include the outline of the initial position of the liner (dashed line) determined using a pre-shot image. The shadowgraphs are contrast enhanced and the plasma boundary is traced (solid line) using a boundary tracing algorithm, similar to that described in Chapter 4. In order to use the boundary tracing algorithm, dark areas due to beam non-uniformities, diffraction patterns, and interference fringes are manually voided as needed, and a local spatial averaging algorithm is applied to smooth out the plasma-vacuum boundary. This allows bulk plasma features to be traced while avoiding tracing spurious features such as interference fringes or beam non-uniformities. The interference fringes on the left side of Figure 5.4(d) are due to the shearing interferometer set up for this shot on this beam path.

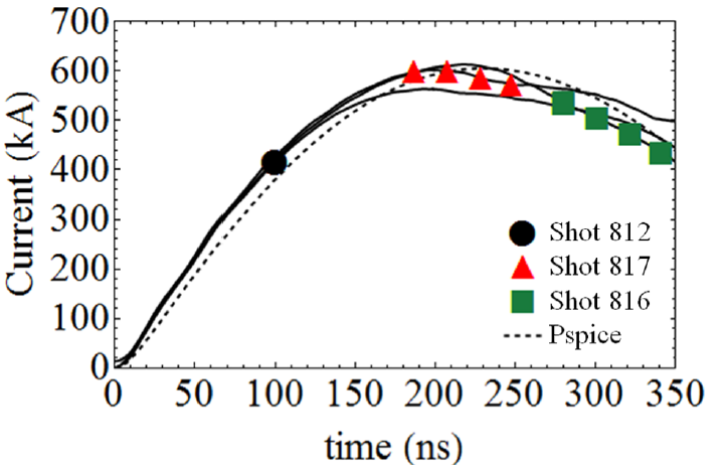

Figure 5.2. LTD current traces and shadowgraph timings for shots 812, 817, and 816. The PSpice simulated current trace is also plotted (dashed line).

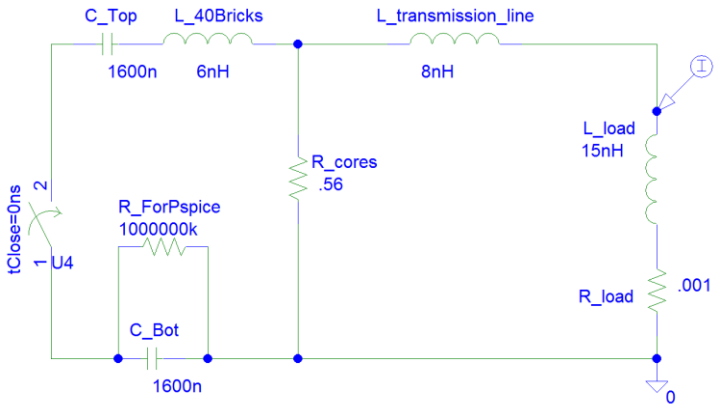

Figure 5.3. PSpice model used to simulate LTD current pulse. The impedance of the cores is approximated by a constant resistance, R_cores. The high value resistor R_ForPspice is required to avoid floating voltages in the PSpice simulation.

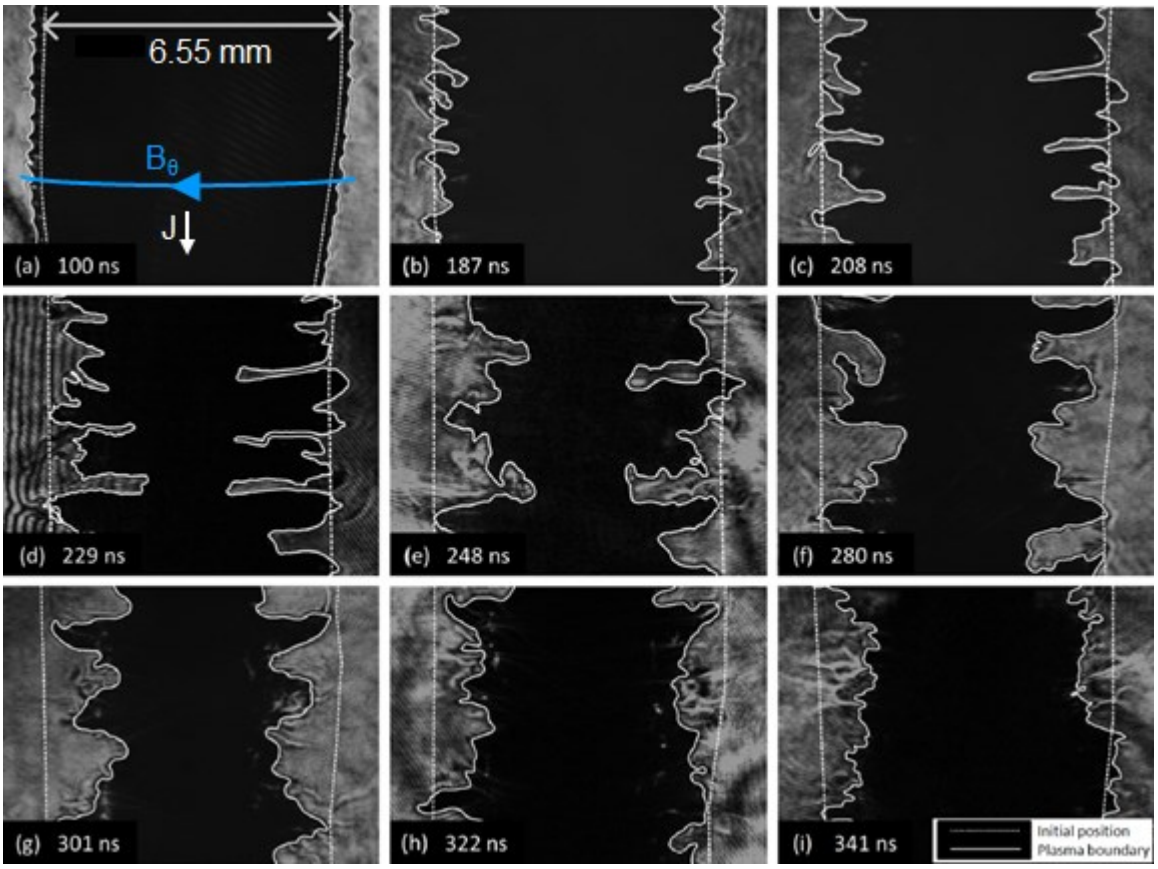

Figure 5.4. Boundary-traced shadowgraphs (aspect ratio 1:1) for unmagnetized shots 812 (a), 817 (b)-(e), and 816 (f-i), showing the four stages of plasma dynamics that occur during the discharge: expansion (a), implosion (b-d), stagnation (e) and (f), and re-expansion (g-i). The direction of the current density $\boldsymbol{J}$ and azimuthal magnetic field B_θ are indicated in (a).

The radius of the observable plasma is determined using the boundary tracing algorithm of Chapter 4 and is shown in Figure 5.5(a) for 13 shadowgraphs obtained from shots 812, 816, and 817. The average plasma radius R_{avg} is determined by averaging the radial extent of the plasma as a function of axial position over the region shown in Figure 5.5(b). The maximum plasma radius is determined for the left and right sides of the plasma and averaged to obtain the characteristic maximum radius R_{max}. A similar method is used to determine the characteristic minimum radius R_{min}. These results are compared to a 0-D implosion model which assumes the mass of the liner is located at a single radius

and calculates the trajectory from the $\boldsymbol{J} \times \boldsymbol{B}$ force for a current pulse $I(t)$, according to the equation

$$\frac{\hat{m}}{2\,\pi r(t)}\ddot{r}(t) = -\frac{B(t)^2}{2\mu} = -\frac{\mu I(t)^2}{8\,\pi^2 r(t)^2} \tag{5.1}$$

where $\hat{m}$ is the liner mass per unit length, r and $\ddot{r}$ are the radius and second time-derivative of the radius, μ is the magnetic permeability, and $B(t)$ is the magnetic field generated by the current flowing in the liner.

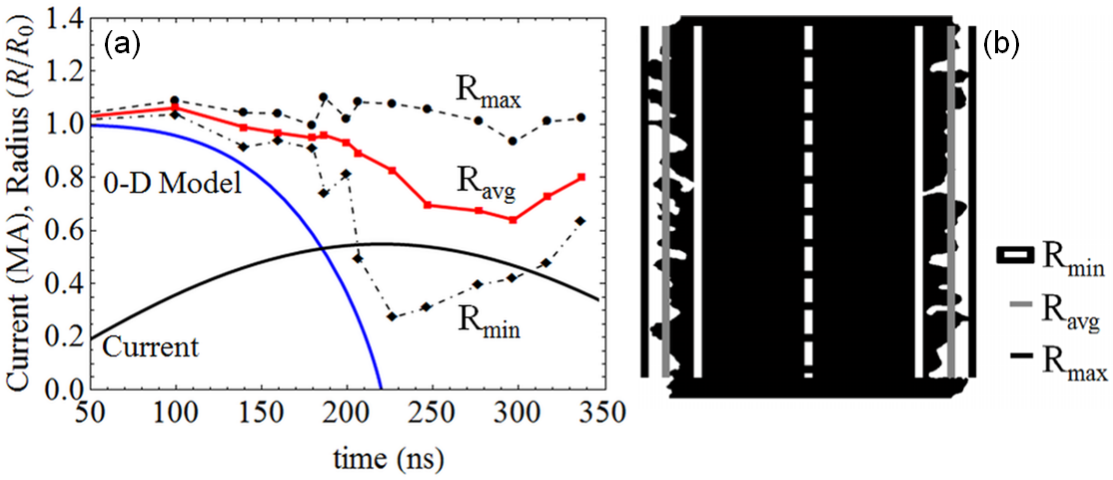

Figure 5.5. (a) Comparison of radii to 0-D implosion model using typical current trace. All radii are normalized to the initial liner radius. (b) Definition of radii obtained from shadowgraphs plotted in part (a), where R_{avg} is plasma radius averaged over liner length, and R_{max} and R_{min} are the average of the left and right maximum and minimum radii, respectively.

The plasma dynamics may be interpreted in four stages: expansion (Figure 5.4(a)), implosion (Figure 5.4(b-d)), stagnation (Figure 5.4(e-f)), and explosion (Figure 5.4(g-i)). During the first stage, the solid-state aluminum is unstable to the striation form of the electrothermal instability, which causes regions of the liner to heat faster than the bulk material. These regions are the first to ablate and couple into longer wavelength structures that seed the subsequent MHD and MRT instabilities, an effect which has been

observed in both HYDRA simulations of liners and experiments conducted at Sandia National Laboratories [PET12, PET13]. The shadowgraph at 100 ns (Figure 5.4(a)) shows small structures of wavelength 0.3-0.6 mm, characteristic of early time instabilities which were also observed on the same 400 nm foils in planar geometry [ZIE12]. In the second stage (Figure 5.4(b-d)), the magnetic pressure becomes large enough to drive the implosion so that the liner-plasma accelerates inward and is unstable to MRT in addition to the $m = 0$ sausage instability. Longer wavelength structures develop in the range of 0.5-1.5 mm, comparable to wavelengths observed in MRT experiments using 400 nm foils in planar geometry [ZIE12]. In the third stage (Figure 5.4(e-f)), the plasma has stagnated on the rod and is no longer accelerating inward. At this time the plasma is MRT stable but remains unstable to sausage modes. Longer, azimuthally correlated instability structures form with wavelengths ranging from 1.7-3.0 mm. At around 300 ns (Figure 5.4(g)), the final explosion stage begins as the magnetic pressure drops due to the decreasing current.

Comparison to the 0-D implosion model shows that the maximum and average plasma radii (R_{max} and R_{avg}) implode slower than the model predicts, while the minimum plasma boundary (R_{min}) shows better agreement. To interpret these results, one must keep in mind the limitations of the 532 nm laser backlighter, which is sensitive to mass trailing the implosion. For example, the shadowgraph in Figure 5.4(d) was taken around the 0-D predicted stagnation time (220 ns) and shows a striking resemblance to a fully imploded Al wire array reported in Lebedev et al. [LEB01], which shows necks where the plasma approaches the axis as well as plasma that remains at the initial radii. The complete implosion dynamics may be better understood using x-ray radiography to fully probe the plasma. This capability is currently being developed by employing x-pinches on the return current path.

While the outline of the initial positions of the liners in Figure 5.4(a-i) lacks up-down symmetry and is not perfectly cylindrical, these latter irregularities are of a large enough spatial scale (millimeter-scale) that they are unimportant to the development of the small scale perturbations that were observed early in time (Figure 5.4(a)). Likewise,

the inherent foil overlap (~7% of the total liner circumference) provides a seed to the very long wavelength $m = 1$ mode, which is similarly unimportant to the short wavelength perturbations observed during the implosion process. These statements stem from the fact that there is only one variation for the entire circumference and that the corresponding wavenumber $m/R = 1/R$ represents a very long wavelength perturbation. Nevertheless, all of these factors affect the azimuthal correlation for the longer wavelength structures, despite the overall cylindrical symmetry. For example, the bottom of the shadowgraphs in Figure 5.4(c-d) show a longer wavelength, azimuthally correlated structure whereas the top does not—this may be due to a random lack of correlation in the initial seed. As noted in Chapter 4 Section 4.1.4, the $m = 0$ and $m = 1$ modes have similar growth rates; therefore, if the initial seed favors the $m = 1$ mode, it will develop even in the absence of an axial magnetic field (see Figure 4.18).

5.1.1 Interferometry Analysis

The shearing interferometry data may be analyzed to measure the electron density as a function of radius. In order to accomplish this, the fractional fringe shift must first be determined by comparing the fringes formed in the presence of plasma to the fringes formed when no plasma is present. As discussed in Chapter 3, these two images are obtained by interfering the laser beam *with a beam-split duplicate of itself* during and post-shot (see Figure 3.9). The latter must be obtained post-shot (while the chamber is at vacuum pressure) and not pre-shot because the pre-shot liner blocks the portion of the laser beam incident upon this region. For the post-shot image, the liner and majority of the support structure have been completely disassembled, and are no longer in the beam path.

The fractional fringe shift at the edge of an instability bump for shot 817 was calculated using IDEA (Interferometric Data Evaluation Algorithms) [HIP04]. The procedure for this analysis is given in Appendix C. By mapping the positions in the IDEA lineout to the radii in the interferogram, the electron density may be estimated as a function of position. These data are plotted in Figure 5.6(c), which shows electron densities as high as $10^{19}/\text{cm}^3$ at the edge of the liner-plasma. This value is used to set a

lower-bound on the plasma density in the instability growth rate calculations in Section 5.3.

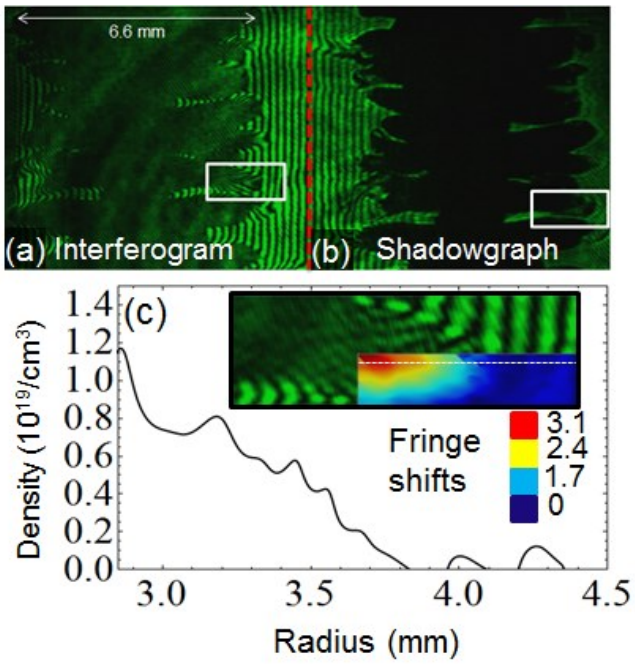

Figure 5.6. Shearing interferometry data for shot 817 (B_z = 0 T) using a simple air-wedge gap interferometer showing: (a) interferogram and, (b) shadowgraph. The boxed regions in (a) and (b) mark the same region of the plasma. (c) The electron density plotted as a function of radius for a sample lineout taken from the boxed region in (a). In (c), the boxed region is enlarged and the fringe shifts are superimposed on the interferogram.

5.2 Instability Mode Analysis

In this section, we investigate the effects of applied axial magnetic fields on the instability structures that develop in imploding liners. The main diagnostic for this set of experiments was the 12-frame shadowgraphy and self-emission imaging system, which enabled measurements of the self-emission striations as the plasma underwent implosion, stagnation, and explosion stages of the discharge. The axial magnetic fields applied were relatively small compared to the self-generated azimuthal magnetic field of the liner-plasma, which exceeded 40 T near peak current and liner compression. The axial magnetic field was systematically varied from B_z = 0.2-2.0 T in order to determine its effects on the azimuthal mode number. These details are outlined in Table 5.1.

Table 5.1. Summary of experimental data for imploding liners.

Shot	B_z (T)	Characteristic mode $\langle m \rangle$	I_{max} (kA)	Image Timing (ns)
1152[a]	0	…	550	84-184
1187	0	-0.1 ± 0.4	480	298-368
1188	0.2	0.3 ± 0.1	550	284-384
1166	0.5	0.9 ± 0.3	530	298-348
1168	0.8	0.9 ± 0.2	550	274-314
1172	1.1	1.8 ± 0.2	580	240-290
1169	1.6	1.4 ± 0.1	570	272-292
1158[b]	2	1.7 ± 0.2	…	308-389

[a]Striations not visible during the imaging window.
[b]Current trace not available.

A series of shadowgraphy images for liners with B_z = 0, 0.2, and 0.8 T is shown in Figure 5.7. The addition of an axial magnetic field resulted in strikingly different instability structures. The B_z = 0 T implosion developed azimuthally correlated self-emission structures that connected the instability bumps and necks on the left and right sides of the plasma (Figure 5.7(a)). Even a small axial magnetic field of B_z = 0.2 T destroyed this symmetry (Figure 5.7(b)). The larger field of B_z = 0.8 T appeared to have

the smallest amplitude structures, while the B_z = 0.2 T magnetized liner showed larger structures than the non-magnetized case. Intuitively, we would expect the progressively smaller instability structures with increasing applied axial magnetic field (see Equations (2.1) and (2.4)). This counterintuitive effect was due to the inner support structure diameter D, which varied for these shots (B_z = 0.8 T [s.1168] had the largest D = 1.5 mm, while B_z = 0.2 T [s.1188] had the smallest D = 1.2 mm), and due to different peak currents (see Table 5.1). Smaller inner support structure diameters allow the plasma to accelerate and develop instabilities over a longer distance, and larger peak currents result in a larger acceleration and higher MRT growth rate.

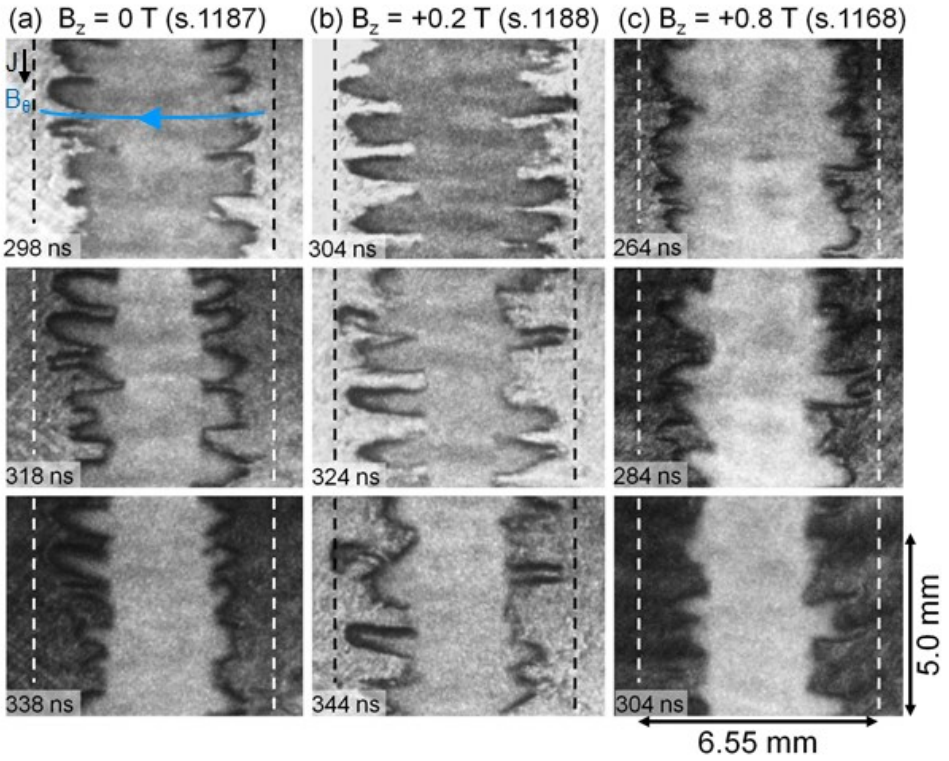

Figure 5.7. Series of shadowgraphy/self-emission images showing for: (a) B_z = 0 T, (b) B_z = 0.2 T, and (c) B_z = 0.8 T. For (a) and (b), the top two frames are during implosion and the bottom frame is during explosion. For (c), all frames show implosion. The direction of the current density $\boldsymbol{J}$ and azimuthal magnetic field B_θ are indicated in (a). The axial B field is in the +z direction.

5.2.1 Measurement Methodology

For each image, the wavelength (λ_{mean}) was determined by averaging the distances λ_i between the centers of all adjacent bumps, and the mean radius (R_{mean}) was determined by averaging the radii R_i for all distinguishable instability bumps, where R_i is the distance from the center of an instability bump (both vertically and radially, identified manually) to the **z**-axis, as shown in Figure 5.8. The uncertainties in the final measurements are estimated using the standard deviation. Note that the mean values λ_{mean} and R_{mean} are insensitive to the uncertainties in the individual measurements λ_i and R_i. In other words, the errors made in choosing an individual λ_i and R_i have little impact on the mean value. The mean plasma radius is plotted in Figure 5.9 for all shots, excluding shot 1158 (which had the largest support structure) in order to show the distinction between implosion (negative velocity) and explosion (defined here by positive velocity). Figure 5.9 also defines the stagnation phase, which begins when the acceleration changes sign and ends when explosion begins. Note that the implosion and explosion labels in Figure 5.9 were individually determined based on the plasma trajectory for the given shot.

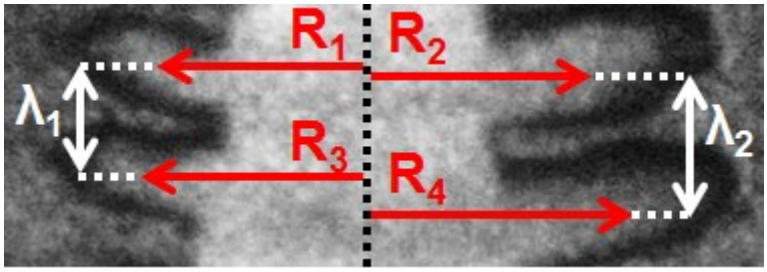

Figure 5.8. Methodology to determine plasma wavelength and radii. The final values are the mean of all wavelengths and radii, with uncertainties determined by the standard deviation.

To measure the striation angles, a region of interest was chosen near the center of the plasma to minimize curvature effects. For each column of pixels across this region, a vertical lineout was taken, where maxima and minima corresponded to bright and dark self-emission striations. The vertical position of each peak and valley was identified

horizontally across the region of interest using the tracking algorithm described in Chapter 4, Section 4.1.2. The self-emission peak and valley position data points were then fit using a linear regression, which gives the 2-D striation angle (note the 2-D striation is the planar projection of the 3-D helical structure). The 3-D striation angle was multiplied by $2/\pi$ to account for cylindrical geometry (see Equation (2.6)) [ATO16]. Pixels in the images were locally averaged over 10 to 20 pixels to facilitate tracking of bulk features (the value of each pixel was taken as the average of all pixel-values within a 10-20 pixel radius). The images in Figure 5.10(a) show the results of this procedure. The two main sources of uncertainty in each measurement were uncertainty in the liner z-axis (estimated at ± 1 degree, not included in Figure 5.12(a) below) and uncertainty in fitting the linear regression, which was small. A third source of uncertainty was the standard error for the distribution of the measured striation angles.

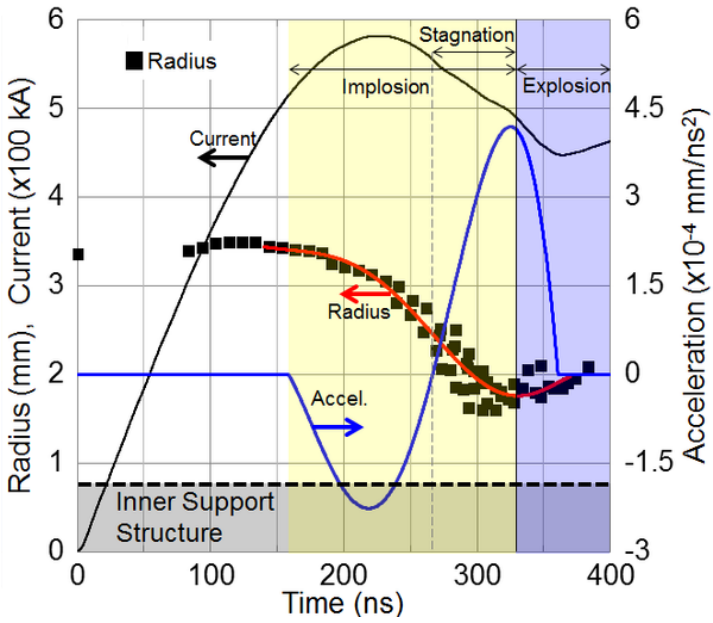

Figure 5.9. Measured current (s.1172), mean plasma radius, and polynomial fits to radius and acceleration. The mean radius is the average of the distances between all instability bump centers and the z-axis, and characterizes the plasma-vacuum interface.

5.2.2 Results and Discussion

As shown in Figure 5.10, negatively-angled striations formed for all axial magnetic fields tested from B_z = 0.2 to 2.0 T. According to the definitions in Chapter 2, these correspond to positive *m* modes, e.g. the striations point in the same general direction as the global magnetic field outside of the plasma structure. In Figure 5.11, the same striation features are tracked during the implosion stage (Figure 5.11(a)) and during the explosion stage (Figure 5.11(b)). The striation angles of these features were found to *increase* during the implosion stage, when the plasma radius was *decreasing*, and to *decrease* during the explosion stage, when the plasma radius was *increasing*. This observation supported the hypothesis that these structures were each due to a discrete helical mode that persisted throughout the discharge.

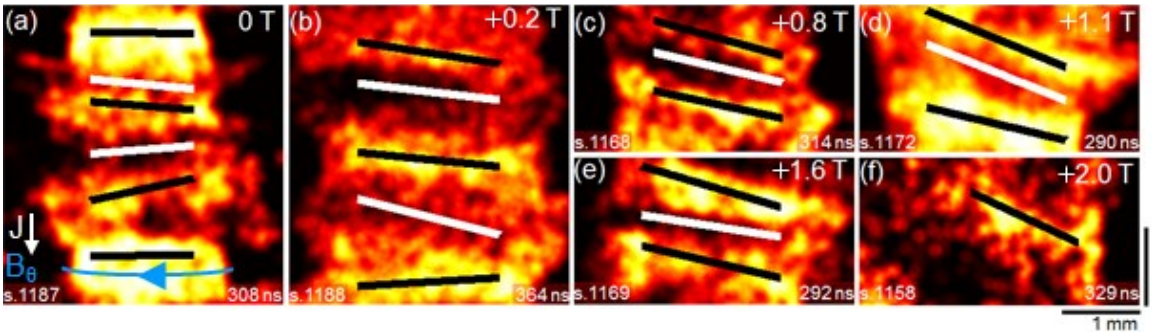

Figure 5.10. Self-emission images at 532 nm and measured striation lines. A tracking algorithm, together with a linear fit, are used to identify bright and dark self-emission peaks and valleys, denoted by the black and white lines, respectively. The direction of the current density ***J*** and azimuthal magnetic field B_θ are indicated in (a). The axial *B* field is in the +***z*** direction.

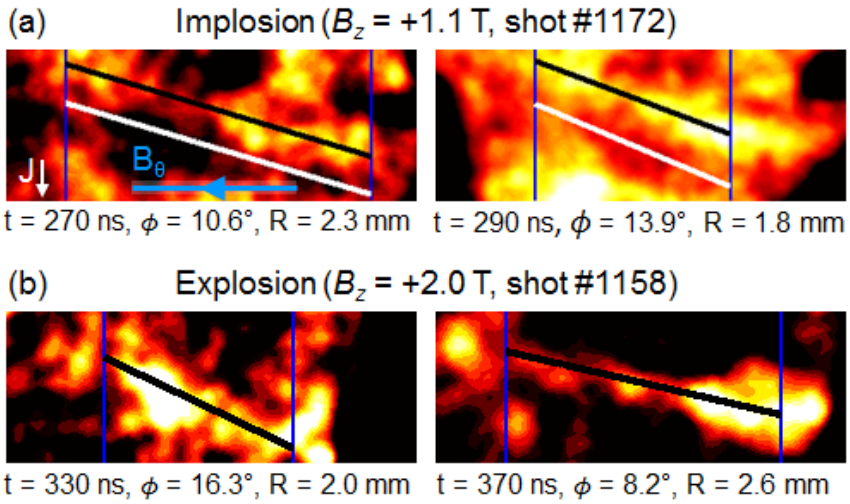

Figure 5.11. Self-emission striations for: (a) implosion and, (b) explosion data. The same bright and dark striations are tracked from image-to-image, and show an increase in striation angle during the implosion stage and decrease in striation angle during the explosion stage. The direction of the current density ***J*** and azimuthal magnetic field B_θ are indicated in (a). The axial B field is in the $+z$ direction.

To further test this hypothesis, we plotted the average measured striation angle against the helical pitch angle m/kR for axial fields of B_z = 1.1, 1.6, and 2.0 T (shots 1172, 1169, and 1158, see Table 5.1) assuming a single helical structure of mode m = 2 that is allowed to vary in radius and wavelength (Figure 5.12(a)). Setting m = 2 was valid because we analyzed only the earliest and subsequent image frames that had two clearly established intertwined helices (see Figure 5.13, which follows the procedure outlined in Chapter 4, Section 4.1.2). Once the azimuthal mode number was fixed, it was assumed to remain constant throughout the analysis. Figure 5.12(a) shows that the mean striation angle was equal to m/kR within uncertainty *during the evolution of the same shot and for all shots*, including both implosion and explosion data. Note that the striation angle *increased* with *decreasing* radius during implosion, and *decreased* with *increasing* radius during explosion, as shown in Figure 5.11. However, the striation angle could only be correctly predicted when taking into account variation in axial wavelength (which tended to increase in time) and by assigning an azimuthal mode of m = 2, which is consistent with the physical interpretation of two intertwined helices (see Figure 5.13).

The evolution of the striations could not be explained by the two intuitive notions that: (a) helical features are frozen into magnetic field lines, and (b) helical structures dynamically evolve to maximize MRT growth, i.e., to minimize magnetic field line bending. Both notions lead to the condition $\boldsymbol{k} \cdot \boldsymbol{B} = 0$, i.e., the helix striation angle is given by $\phi_B = B_z / B_\theta$ just outside the plasma at the time of measurement. The data showed no such trend, with the maximum angle predicted by B_z / B_θ in Figure 5.12(a) being less than 4 degrees while the measured angles ranged from 4-14 degrees. Such a deviation is even more evident in Awe et al. [AWE13, AWE14], where the angle predicted by B_z / B_θ is effectively zero, but the observed helix angle is 16-26 degrees. It is important to note that these calculations assume that: (1) the azimuthal magnetic field just outside the shadowgraphy boundary is given by a current-carrying column of radius R_{mean}, with no current losses within a smaller radius of the B-dot location in the transmission line (e.g., the measured B-dot current is equal to the current in the liner), and (2) the axial magnetic field is unchanged from its original applied value. Both of these assumptions could be tested experimentally, using diagnostics such as micro B-dots, Zeeman splitting, or Faraday rotation.

The fact that the observed helical structures agreed with the predicted pitch angle $\phi_h = m/kR$, despite a dynamically changing radius and axial wavenumber, indicated that there was a dominant helical mode that persisted throughout the discharge. This motivated our next systematic study of the dependency of azimuthal mode number on the axial magnetic field. For the unseeded liners used in this experiment, various azimuthal modes (m = 0, +1, +2) may co-exist and even merge as the system evolves. For these reasons, we may define a characteristic azimuthal mode number $\langle m \rangle$ as the average of all modes in the plasma for a given shot (and therefore B_z), determined using the following procedure. First, the mean of all modes observed in a single image is found by normalizing the mean striation angle by $1/kR$. These are the black data in Figure 5.12(b). For a given shot, the mean mode per image is averaged for all images of that shot to obtain $\langle m \rangle$: these are the red data in Figure 5.12(b). These values are summarized in Table 5.1 as a function of the external axial magnetic field, and are interpreted as follows.

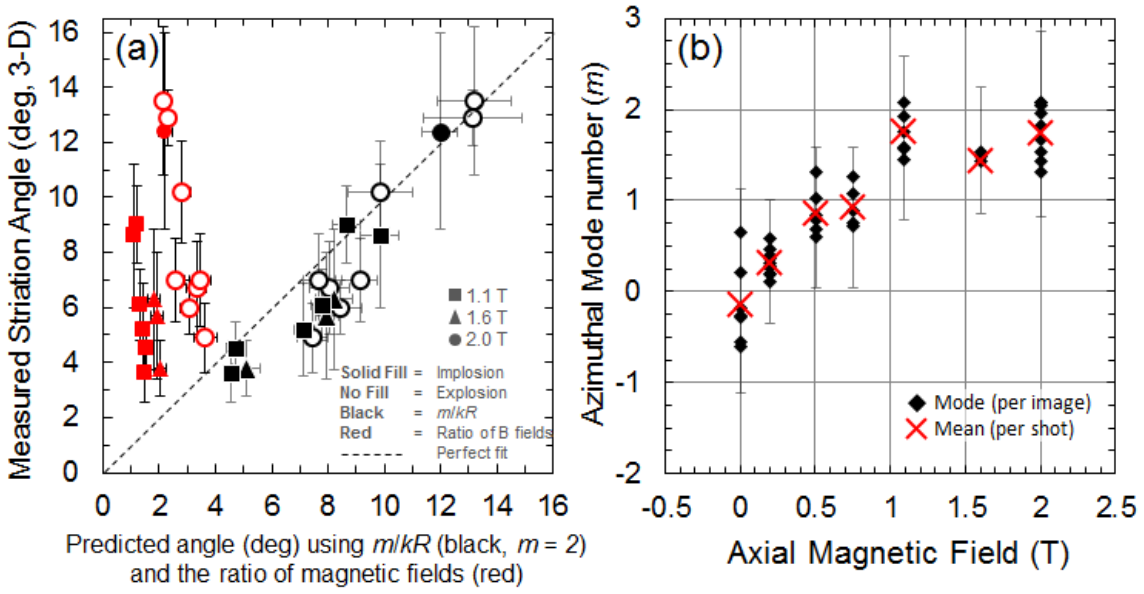

Figure 5.12. (a) Plot of measured striation angle against the angle predicted assuming a discrete helical mode with azimuthal mode $m = 2$ ($\phi_h = m/kR$, black), and with the predicted angle from the ratio of magnetic fields at time of measurement ($\phi_B = B_z/B_\theta$, red). The dashed line shows a perfect fit. (b) The azimuthal mode number, determined by dividing the measured striation angle by $1/kR$, plotted against the initial axial magnetic field. In (b), the tips of each vertical error bar represent the maximum and minimum values in the corresponding shot.

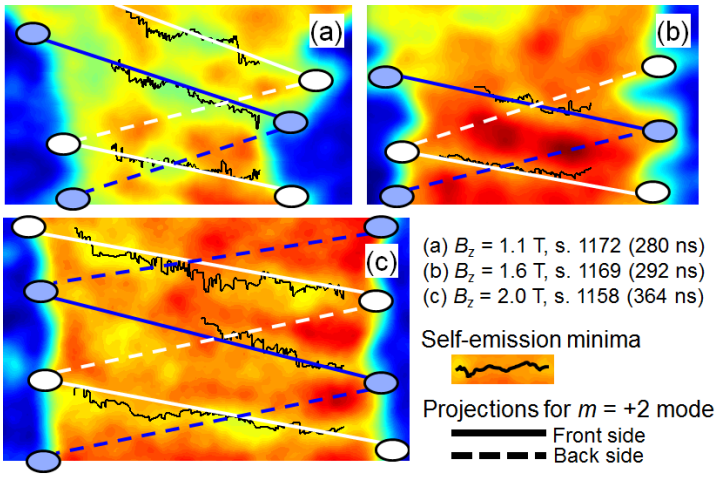

Figure 5.13. Identification of the $m = +2$ structure for the data in Figure 5.12(a), determined by comparing the projection of the $m = +2$ mode (blue and white lines) to the self-emission minima (black lines). Ovals indicate the location of instability bumps.

First, Figure 5.12(b) shows that the standard deviation in the data about $\langle m \rangle$ is small, meaning that: (1) the characteristic mode persisted throughout the discharge, despite the dynamically changing environment, and (2) there is a dominant m mode, *or at most two co-existing* m *modes*. Second, even a small axial magnetic field was able to excite helical modes that are not apparent in the unmagnetized data. The smallest value of $B_z = 0.2$ T was on the threshold for the appearance of helical modes, with both $m = 0$ and $m = +1$ modes co-existing in different axial regions of the liner (Figure 5.14(b) demonstrates how this co-existence is possible; however, the exact mode identification would require the location of the dark striations on the back side of the plasma). Our data strongly suggest that gradually increasing the axial magnetic field from zero to 0.5 T would simply change the relative importance between the $m = 0$ and $m = +1$ modes. When the axial magnetic field was increased to $B_z = 0.5$ and 0.8 T, only the $m = +1$ mode was dominant (Figure 5.12(b)). Further increasing the axial field to $B_z = 1.1$, 1.6, and 2.0 T, generated an $m = +2$ mode that overwhelmed the $m = +1$ mode. Note the two intertwined helices for the $m = +2$ mode, as shown in Figure 5.13, which was constructed after careful consideration. Finally, physical interpretations of the measured characteristic modes for various magnetic fields are shown in Figure 5.14.

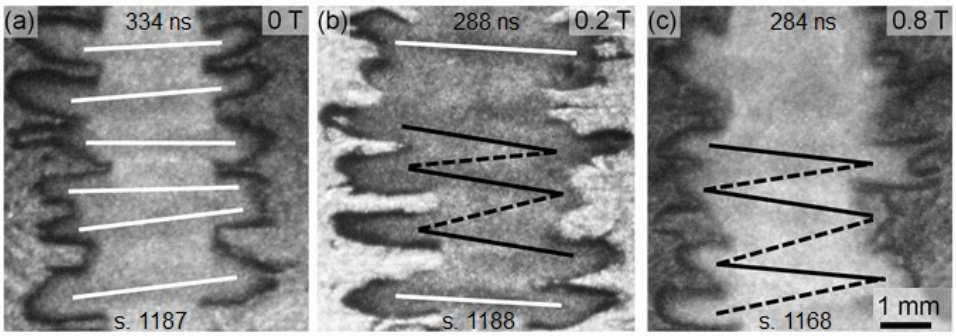

Figure 5.14. Shadowgraph images overlaid with the projection of the characteristic modes from Figure 5.12(b). Dark self-emission bands are used to connect the instability bumps on the front (solid lines). Dashed lines connect instability bumps on the back side, and are determined by assuming a similar angle is conserved from the front side. The white lines indicate azimuthally symmetric modes and the black lines indicate helically oriented modes.

5.2.3 Application of Weis-Zhang-Lau Instability Theory

To explore the dominance and persistence of helical modes, we once more used the Weis-Zhang-Lau theory [WZL15] to study the instantaneous sausage-MRT and helical-MRT growth rates via an ideal MHD, sharp boundary model. The instantaneous radius (and therefore acceleration) was determined by fitting a sixth order polynomial to the mean plasma radii in Figure 5.9 starting from 140 ns (160 ns for the start of acceleration). Prior to this start time, the bulk liner motion was small, so that the acceleration was assumed to be zero.

Figure 5.15 shows theoretical growth rates for B_z = 0, 0.2 and 2.0 T using a time-dependent axial wavelength model that approximately matches experimental parameters, λ_{mm}=0.2*(cosh[0.01*t_{ns}]). This model captures the wavelength of the structures that first appear at ~80 ns (~0.3 mm) and at ~200 ns (~0.8 mm). The hyperbolic cosine dependence was chosen because of the slow variation early in time (<150 ns) and rapid increase later in time as structures merge and wavelengths begin to double.

Interestingly, for B_z = 0 and 0.2 T, the m = 0 and m = 1 modes have nearly identical growth rates (the small differences are not resolvable in Figure 5.15, which shows the curves as being superimposed), despite the experiment showing azimuthal symmetry for B_z = 0 T and a departure from symmetry for B_z = 0.2 T. Increasing the field to B_z = 2.0 T showed a dramatic effect on the shape of these growth predictions: the m = 0, 1, and 2 modes are completely stabilized for nearly 100 ns. Among these modes, the m = 2 mode becomes the first to destabilize, followed by the m = 1 mode, and finally the m = 0 mode. This means that there is a window in time when the higher m modes are unstable and can freely grow while smaller m modes cannot (see also Figure 4.15(b,d)). This window exists for any nonzero axial field (with stronger effects for increasing B_z); during this time, the general helical shape of the higher m modes may be locked-in (perhaps even modes with $m \gg 2$). However, if smaller axial wavelength structures merge into larger axial wavelength structures, a common occurrence in RT or MRT, a high m mode may convert into a lower m mode. This mechanism was discussed in Chapter 4, Section 4.1.2 for helical mode merging in non-imploding liners. Figure 5.15

also shows the significant coupling of the classical sausage and helical modes (when there is no radial acceleration) to MRT (when there is radial acceleration [WZL15]). First, there is a dramatic increase in growth rate, and second, there is a reduction in the disparity between m = 0, 1, and 2 modes after t = 160 ns. This indicates that whatever structure has been seeded before this point will persist during the implosion phase; a conclusion consistent with our experimental results and those of Awe et al. [AWE13, AWE14].

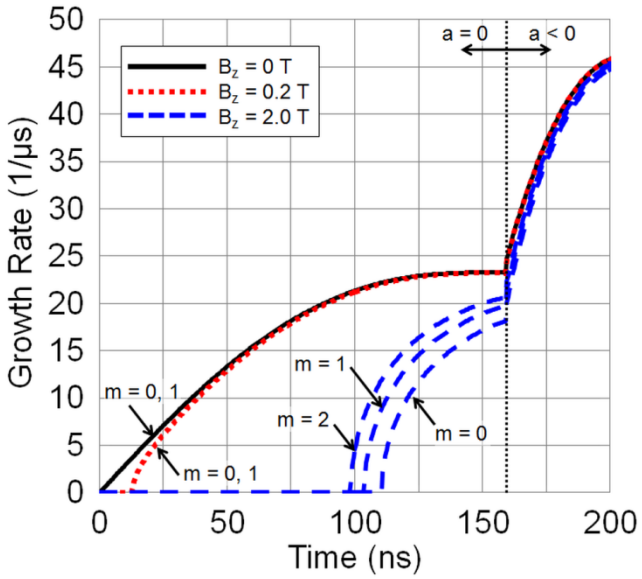

Figure 5.15. Growth rate calculations using Weis-Zhang-Lau theory for time-dependent experimental parameters (magnetic fields and radius). Estimated parameters were ablated liner-plasma thickness (500 μm) and mass density (4.5 kg/m^3). The wavelength varies according to $\lambda_{mm}=0.2\cdot(\cosh[0.01\cdot t_{ns}])$. Liner acceleration begins at 160 ns.

5.3 Summary

In this Chapter we have demonstrated that it is possible to implode an initially solid cylindrical liner with sub-megaampere current pulses using a simple dumbbell-shaped support structure. This enabled the plasma to implode over a distance of 1-2 mm, and permitted the coupling of MRT to the MHD modes. By tracking the self-emission structures throughout the implosion, stagnation, and subsequent explosion, we found that: (1) there is only 1, or at most 2, dominant azimuthal modes for each seeded axial magnetic field, (2) there is no sharp threshold in the axial magnetic field for the appearance of the helical modes, and (3) higher applied axial magnetic fields favor the development of higher order azimuthal (m) modes. The seeding of these azimuthal modes (including $m = 0$) by mechanisms such as electrothermal instability remains an outstanding issue.

CHAPTER 6
CONCLUSION AND FUTURE WORK

This thesis presented an experimental investigation of helical features on magnetized, ultrathin foil-plasmas driven by the 1-MA linear transformer driver at the University of Michigan. Three types of cylindrical liner loads were designed to investigate different aspects of helical instabilities, including: (1) pure MHD modes (defined as devoid of the acceleration-driven magneto-Rayleigh-Taylor instability, MRT) using a non-imploding geometry, (2) pure kink modes using a non-imploding, kink-seeded geometry, and (3) MRT-MHD coupled modes in an unseeded, imploding geometry. For each configuration, we applied relatively small axial magnetic fields of B_z = 0.2 - 2.0 T (compared to peak azimuthal fields of 30 - 40 T). The resulting liner-plasmas and instabilities were imaged using 12-frame laser shadowgraphy and visible self-emission on a fast framing camera, and the azimuthal mode number was carefully identified with a tracking algorithm of self-emission minima.

The development of sausage and helical instabilities was first investigated in non-imploding liners in order to minimize the effects of radial acceleration, and therefore minimize the effects of the magneto Rayleigh-Taylor instability. Both unseeded and kink-seeded liners were investigated in this non-imploding geometry. For the unseeded liners, when no axial magnetic field was applied, an m = 0 sausage instability developed. When a relatively small, pre-imposed axial field of 1.1 T was applied (compared to the peak azimuthal field of ~30 T), a smaller amplitude, m = +2 helical mode developed, consisting of two intertwined helical structures spiraling in the same sense of rotation as the global magnetic field. Despite the smaller amplitude, the experimental growth rates were surprisingly similar, with the unmagnetized liners exhibiting a slightly larger growth rate. These results were corroborated with analytic theory, which showed for an applied

axial magnetic field there is a window in time when helical modes are unstable but the sausage mode is completely stabilized, indicating that helical modes should develop.

Using a kink-seeded support structure for the non-imploding geometry, we explored the importance of the intrinsic modes relative to the seeded modes. We found that the plasma seeding dominates the natural instability modes of the plasma. Despite the magnitude and orientation of the applied axial magnetic field (B_z = -1.6 T, 0 T, +1.6 T), the same seeded plasma structure arose *and not* the intrinsic modes of the corresponding unseeded configuration. This enabled an investigation of the stability of the neutral, positive, and negative helical modes, where the sign of the mode is defined in Chapter 2 and determined by the sense of rotation of the plasma helix when compared to the global magnetic field. It was found that the applied axial field impacted the overall stability, with the negative m mode invoking the largest magnetic tension and thus being the more stable mode. The positive m mode was initially more stable than the neutral mode due to the addition of the axial magnetic field, but later in time developed a comparable instability amplitude.

An experimental platform was next developed to investigate liner implosions on the University of Michigan Linear Transformer Driver facility, enabling new physics to be explored where the liner-plasma implodes, stagnates, and subsequently explodes. The radial acceleration during the implosion stage enabled the magneto Rayleigh-Taylor instability to couple to the sausage and kink instabilities. The important question of whether the instability structures were due to a discrete helical mode or were tied to the global magnetic field was addressed by measuring the self-emission striation angles during the implosion, stagnation, and explosion stages of the discharge. Our experiments showed that the helical structures are manifestations of discrete eigenmodes, and that the pitch angle, ϕ, of the helix follows the simple geometric equation $\phi = m/kR$, from implosion to explosion, where m, k, and R are the azimuthal mode number, axial wavenumber, and radius of the helical instability. Thus, the pitch angle increases (decreases) during implosion (explosion) as R becomes smaller (larger). We found that one (or at most two) discrete helical mode(s) developed for magnetized liners, with no

apparent threshold on the applied axial magnetic field for the appearance of helical modes. Gradually increasing the applied axial magnetic field from zero changes the relative weight between the $m = 0$ and $m = 1$ modes. Once the discrete helical modes were identified, the azimuthal mode number $m = \phi \cdot kR$ was investigated by systematically varying the applied axial magnetic field. The results of this investigation demonstrated that higher applied axial magnetic fields yield higher order azimuthal mode numbers.

While important questions were answered concerning the development and persistence of helical instability modes, much work remains to fully understand their nature. Future investigations could include the effects of higher applied axial magnetic fields, driving the Helmholtz coils up to the maximum value for our capacitor bank, 5.5 T. Higher order modes may develop, which could be identified using the methodology presented in Chapter 4 and 5. Another important question is whether the axial magnetic field is delaying the formation of instability bumps. The analytic theory predicts that axial magnetic fields should delay the onset of helical modes, and that larger values of applied axial fields would additionally delay this onset time.

One of the reasons that pre-imposing the axial magnetic field enabled interesting physics was because the ratio of B_z/B_θ was initially large. New physics could be explored using helical return current paths so that the ratio B_z/B_θ is constant (until the liner implodes, which would cause B_θ to increase). This can potentially result in a larger axial magnetic field than the fields available using the Helmholtz coils, with the caveat that the value of the axial magnetic field early in time would be small. This type of system can be investigated for the non-imploding liners, kink-seeded liners, and imploding liners. The latter system is known as a dynamic screw pinch and its stability was analytically investigated by Schmit et al. [SCH16]. For this system, the external magnetic field lines rotate in time as the liner implodes, so that the magnetic field lines provide a stabilizing magnetic tension throughout the discharge. The results of these experiments could be directly compared to data of this thesis. Note that the screw pinch could provide an initial

seed to a helical instability by perturbing the magnetic field on the surface of the liner due to the helical return current path.

In Chapter 4, the concept of helical mode merging was introduced. This could be further investigated by seeding an $|m| = 2$ mode using a 3-D printed support structure, and then observing the saturation and merging to the larger wavelength $|m| = 1$ mode. This would enable an investigation of the cascade process that might have occurred in MagLIF liners, where an $m = +6$ helix observed by Awe et al. [AWE13, AWE14] may cascade into an $m = +1$ or +2 helix observed by Gomez et al. [GOM15] in the fuel during stagnation.

New diagnostics could be implemented. First, a front/back self-emission imaging system has already been developed in order to observe the full surface of the liner. This diagnostic has not yet been implemented for magnetized liner implosions, and would enable instability bumps to be connected completely around the liner using self-emission features. Second, direct measurements of the axial magnetic field near the liner are essential. This would enable an investigation of possible flux compression of the axial magnetic field. These measurements could be accomplished using diagnostics such as Faraday rotation, optical Zeeman splitting, and/or micro B-dots. Third, the imaging systems could be improved by implementing a 12-frame interferometry/shadowgraphy system, incorporating the air-wedge system described in Chapter 3, so that density measurements could be obtained throughout the entire discharge. Fourth, x-ray backlighting could be accomplished by using x-pinches on the return current path; this would enable probing of the dense liner-plasma and perhaps enable the observation of density perturbations due to helical instabilities, such as those observed by Awe et al. [AWE13, AWE14]. Fifth, a 4-frame XUV camera is currently being implemented on the MAIZE LTD; this system could perhaps enhance the visibility of self-emission striations. Finally, the 355 nm ultraviolet beam of the Nd:YAG laser could be implemented to probe structures deeper into the plasma.

APPENDIX A

APPLIED AXIAL MAGNETIC FIELD SYSTEM

A.1 Operating Procedure

The Helmholtz coils are driven by the same capacitor bank and triggering system used to drive the applied axial magnetic field for the Michigan Electron Long Beam Accelerator (MELBA). The two differences are: (1) the BNC box in the LTD control room is used to trigger the ignitron, and (2) the output of the ignitron is connected to the coil cables (see Figure A.1). To operate the coils, the MELBA interlocks must be set, and an operator must initiate the capacitor bank charging system in the MELBA control room. Simultaneously, an operator initiates the LTD triggering sequence. This is typically done as follows:

Preshot Procedure

1. The LTD oscilloscopes are set using Labview, but the LTD charge sequence is **not** initiated
2. The coil capacitor bank is set to 0.2 kV in the MELBA control room and charging is initiated.
3. Once charge is complete, a message is passed (through an instant messaging program) from the operator in the MELBA control room to the operator in the LTD control room.
4. The operator in the LTD control room triggers the LTD sequence, which triggers only the ignitron and **not** the LTD switches.
5. The oscilloscope B-dot trace is observed to determine whether the preshot was successful.

Shot Procedure

1. The LTD oscilloscopes are set using Labview. The LTD operator **waits until a message from the MELBA operator is sent** before charging the LTD capacitors.
2. The coil capacitor bank is set to the desired charging voltage (0.2 – 5 kV = 0.2 – 5.5 T) in the MELBA control room and charging is initiated.
3. Once charge is complete, a message is passed (through an instant messaging program) from the operator in the MELBA control room to the operator in the LTD control room.
4. The operator in the LTD control room initiates the LTD charge sequence.
5. The operator in the LTD control room triggers both the ignitron and the LTD switches.

A.2 Coil Configuration

The coil configuration is shown in Figure A.1. Figure A.1(a) shows the ignitron-to-coil connection. The 30 Ohm resistor was used for initial tests to reduce the strain on the coils and has since been shorted using a high voltage cable. The cable coils consist of two coaxial cables connected in parallel in order to reduce the coil resistance. For the initial coil tests, the current was measured using a Pearson coil on the return current braid that is connected to ground. The Pearson coil was removed for the higher voltage shots because its core saturated during the current rise, rendering the diagnostic unusable. In Figure A.1(b), the vacuum feedthrough system is shown, where the two coaxial cables A and B are the same cables in Figure A.1(a). The feedthrough is formed using quick-connect couplings on the LTD flange. Inside the chamber, cables A and B connect to the parallel-to-series hermetically sealed cable adaptor, which wires the parallel cables A and B to the series coaxial cables 1 and 2, shown in Figure A.1(c). A diagram of the coil setup is shown in Figure A.2, which shows a simplified parallel-to-series connection for the hermetically sealed adaptor. The coils are wired in series to ensure the same current is driven through the two coils.

The coil magnetic field was measured using a ~5 cm diameter B-dot. The B-dot was calibrated using a fast hall-effect probe. The calibration setup is shown in Figure A.3. The curves in Figure A.4 show the magnetic field signal from the calibrated, integrated B-dot signal along with the signal from the hall-effect probe. The B-dot signal is shown in red.

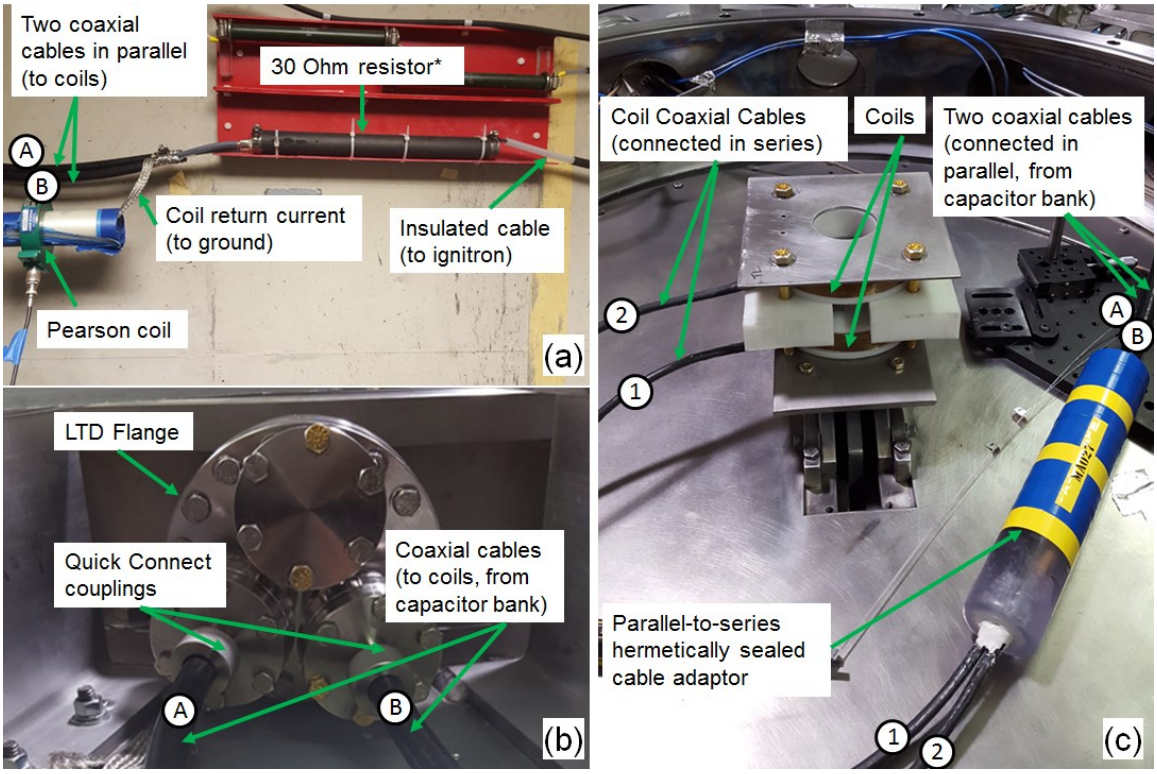

Figure A.1. (a) Coil cable configuration in capacitor bank room. (b) Vacuum feedthrough system for coil cables. (c) Coil system in chamber. Coaxial cables A and B are wired in parallel and are the same cables for all figures. Coaxial cables 1 and 2 are wired in series.

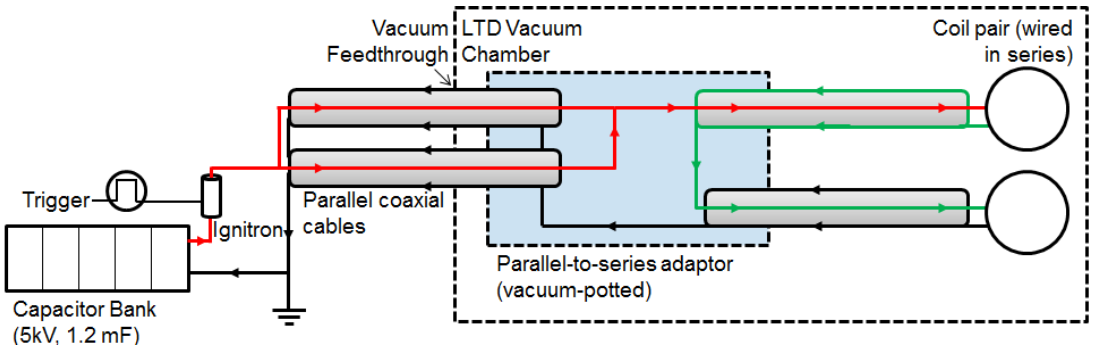

Figure A.2. Schematic for applied axial magnetic field coil system. The capacitor bank is charged from 0.2-5 kV, and is switched to the parallel coaxial cables using an ignitron. Inside the vacuum chamber, the vacuum-potted adaptor wires the parallel cables to two series cables, so that the coils are wound in series.

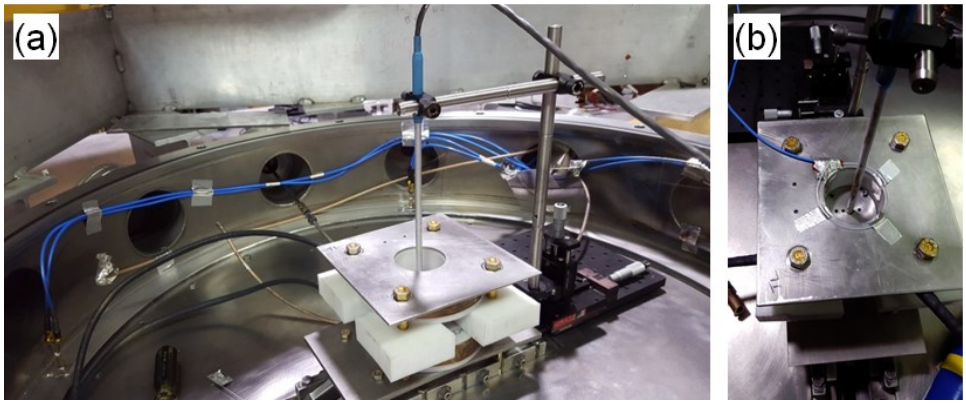

Figure A.3. (a) Coil testing configuration using fast hall-effect probe. (b) B-dot calibration configuration.

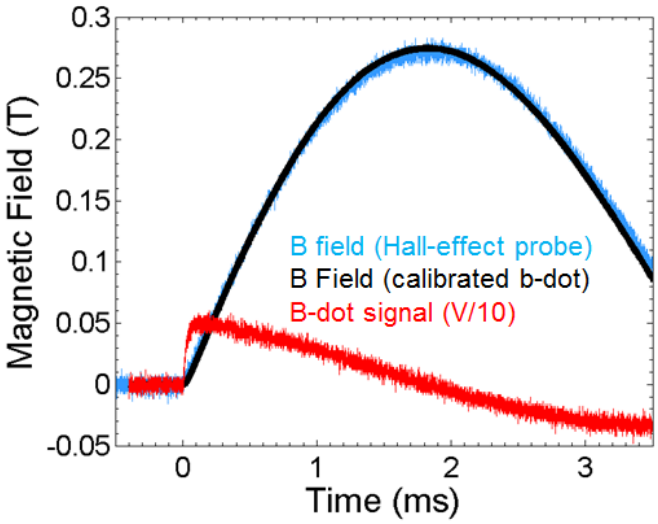

Figure A.4. Plot of the magnetic field measured using a fast hall-effect probe (blue) and the calibrated, integrated B-dot signal (black). The raw B-dot signal is shown in red.

A.3 Helmholtz Coil PSpice Circuit Model

The coil circuit model, shown in Figure A.5, was devised for our pulsed power bank and coil specifications from Rovang et al. [ROV14]. The specifications are slightly different than the coils we received from Sandia; however, they are sufficiently close to generate a suitable current trace to investigate the magnetic field diffusion in stainless and aluminum (the diffusion simulation results are presented in Chapter 3). The coil current is shown in Figure A.6. This is the current through a single winding (i.e. a single turn of the coil), which is used to drive the current through the two 80-turn coils in the Maxwell simulation presented in Chapter 3, Section 3.3.2.

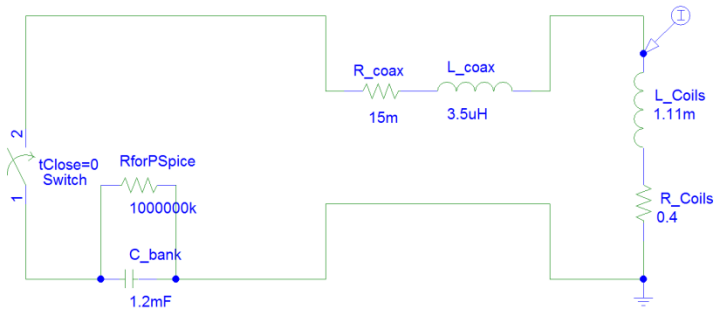

Figure A.5. PSpice circuit diagram for calculating current through Helmholtz Coil. Circuit parameters are obtained from Rovang et al. [ROV14].

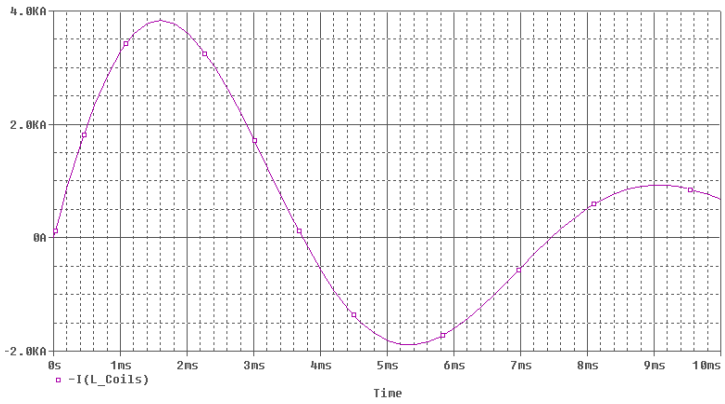

Figure A.6. Simulated PSpice current through a single coil turn. This current was used in ANSYS Maxwell to drive the two 80-turn Helmholtz coils in order to investigate the axial magnetic field diffusion.

APPENDIX B

PLASMA BOUNDARY TRACING ALGORITHMS

The measurements for instability amplitude and mean plasma radius in Chapter 4 and Chapter 5 were obtained by tracing the vacuum-plasma boundary. While this boundary may be somewhat subjective, a unique, consistent methodology was implemented for both diagnostics (shadowgraphy/self-emission and self-emission only). For each diagnostic, an algorithm was implemented in MatLab. An overview of these algorithms is presented below.

B.1 Shadowgraphy & Self-Emission Images

1) The images are rotated so that the liner is in the vertical direction using the preshot image as a guide.
2) The shadowgraphy boundary is manually traced in MS Paint using a thick white line so that edge of white line is adjacent to the outer black region (while a more rigorous method could be used to measure this boundary, the clarity of the black line indicates that these tracings are not unduly subjective).
3) The boundary is read using a MatLab script that finds position of the white line. This boundary is taken as the inside pixel of the white line (which corresponds to the outside of the dark shadowgraphy region).

The result of this procedure is shown in Figure 4.3, where the image in (a) shows the manually traced white line and the image in (b) shows the computer-read position in red.

B.2 Self-Emission Only

1) The images are rotated so that the liner is in the vertical direction using the preshot image (with laser backlighter) as a guide.
2) A blurring algorithm is applied in MatLab by averaging pixel values over ~5 pixels. This is done to smooth out irregularities in brightness.
3) A brightness boundary threshold is determined for each image
    a. For an image of size (*n, m*), *m* vertical lineouts are taken. The mean of these lineouts (i.e. the mean of all pixel values in a vertical line) results in an array called *jmean* of length *m*, which is a function of the horizontal position.
    b. A smoothing algorithm is applied over 100 pixels to *jmean.* The value of 100 was chosen to smooth out large-scale irregularities, but not so much to completely mix the black background and white/gray self-emission regions. The result is an array called *jsmooth* of length *m.*
    c. The brightness threshold is then set to 40% of maximum brightness value of *jsmooth.* This characterizes the maximum brightness of the overall self-emission image by excluding small and large scale irregularities.
4) For each vertical position (*n* values), the algorithm starts searching for the left/right boundary from the center of the image, moving outward and using the blurred image from Step 2. Once the pixel value drops below brightness level from Step 3(c), this horizontal position becomes left/right plasma boundary. The result is two arrays of *n* values (corresponding to left and right boundaries) which give the horizontal pixel position that corresponds to the 40% threshold.

The result of this procedure is shown in Figure 4.3(c).

APPENDIX C

INTEFEROMETRY DATA ANALYSIS

In this section we analyze the interferometry data of Chapter 5, Figure 5.6, reproduced below. Note that not all portions of the interferogram are suitable for analysis. Regions of the beam that are refracted outside of the system, absorbed, or attenuated, leave behind a "shadow," which may be seen in Figure 5.6(b). These regions tend to be at a smaller radius of the plasma, where the density and density gradients are sufficiently large to attenuate or refract laser light out of the imaging system. The regions which are useful for interferometry are located near the edges of the liner-plasma, where fringe shifts as high as 3.1 may be observed. A window was chosen (see the white box in Figure 5.6(a)) at the edge of one of the MRT-sausage bubbles to perform the following analysis.

Details on the method outlined here may be found in the IDEA user manual [HIP04]; they are summarized here. To perform the analysis, the following procedures must be applied separately to the reference (post-shot) and plasma (shot) images before performing the final fringe-shift count. First, unusable portions of the images must be *masked*; these portions are excluded in the analysis. Second, zero-padding must be added, which expands the image size to a power of two (this is required for performing the 2-D FFT). Then, the image is Fourier transformed using the *2-D FFT* algorithm. This data must be filtered by selecting a window which contains the frequency bandwidth of the fringes. The image is then back-transformed using the *Filtered Back-FFT to 2D Mod 2Pi* algorithm to obtain a filtered interferogram. The frequency space filtering and back-transforming are likely the most cumbersome steps, as they may require multiple attempts at masking the appropriate windows in FFT space in order to generate an acceptable filtered interferogram. The filtered interferogram may be compared to the original in order to determine whether the filtering was sufficient or excessive. The 2-D

phase-shift distribution is then obtained using the *2DScan Method* followed by *Unwrap with Step Function*. Once the phase-shift distributions are obtained for the reference and plasma images, the final 2-D fringe shift is obtained by subtracting the reference phase-shift from the plasma phase-shift using the *Subtract Image/2D-Data* function. The result of this procedure is shown in the insert in Figure 5.6(c), which shows fringe shifts with values up to 3.1.

A lineout of this data may be obtained and exported from IDEA. This data contains the path integral of the index of refraction of light of the light ray that has travelled through the plasma bubble [VES79],

$$\Phi = \int \mathrm{n}\, ds, \tag{C.1}$$

where Φ is the optical pathlength of the ray in the plasma, n is the index of refraction, and ds is the infinitesimal displacement along the light ray. To continue the analysis, the assumption must be made that the rays of light that travel through the plasma and are recorded by the imaging system are *refractionless*. While this may seem counterintuitive (we have previously discussed rays of light that are fully refracted out of the optical system due to gradients in the plasma), this *refractionless limit* makes the mathematics of the inversion analysis tractable. To reconcile this, let us separate the plasma into both refracted and refractionless regions, as shown in Figure C.1. We may then describe the optical pathlength in the refractionless region using the equation

$$\Phi(\mathrm{x},\mathrm{y}) = \int \mathrm{n}(x,y,z)\, dz, \tag{C.2}$$

where the ray of light is assumed to travel in the z-axis only, and the plasma column axis is in the y-direction, (see Figure C.1). Subtracting the reference pathlength from the plasma pathlength (this was done in IDEA using the S*ubtract Image* function) gives the optical pathlength difference

$$\Delta\Phi(\mathrm{x},\mathrm{y}) = \int [\mathrm{n}(x,y,z) - \mathrm{n}_0] dz = N\lambda, \tag{C.3}$$

where n_0 is the index of refraction of vacuum (equal to unity), N is the fringe shift, and λ is the wavelength of the laser light. This equation describes the position of the bright fringes in the interferogram, and must be inverted to obtain $\mathrm{n}(x, y, z)$, which in-turn gives information about the electron density in the plasma. To invert this equation, we must assume that the plasma is radially symmetric so that n = n(r), and that the index of refraction in the plasma image is unity at large radii. Equation (C.3) may then be expressed as

$$N(x) \cdot \lambda = 2 \int_x^\infty \frac{(\mathrm{n}-1) r dr}{(r^2 - x^2)^{1/2}}, \tag{C.4}$$

where the factor of two arises from the conversion to polar coordinates. This equation may be Abel inverted to obtain the function $f = \mathrm{n}(r) - 1$,

$$f = -\frac{\lambda}{\pi} \int_r^\infty \frac{(dN/dx) dx}{(x^2 - r^2)^{1/2}}. \tag{C.5}$$

Using the i = (1, L) discrete points from the fringe shift N data obtained from the IDEA lineout, this the function f may be expressed as

$$f_i = -\frac{2\lambda}{\pi \, \Delta r} \sum_{k=i}^{L-1} (N_{k-1} - N_k) \frac{\left[(k+1)^2 - i^2\right]^{1/2} - \left(k^2 - i^2\right)^{1/2}}{2k+1}, \tag{C.6}$$

where Δr is the physical distance between the L discrete points on the IDEA lineout data (typically equal to the size between pixels on the interferogram). Each f_i corresponds to the index of refraction at a given radius, which may be used to estimate the electron density at that radius using the index of refraction of plasma,

$$n_e = f_i / (-4.46 * 10^{-14} \lambda^2), \tag{C.7}$$

where λ is expressed in centimeters (λ = 5.32e-5 cm). By mapping the positions in the IDEA lineout to the radii in the interferogram, the electron density may be estimated as a function of position. This is shown in Figure 5.6(c), which shows electron densities as high as 10^{19}/cm^3, which may be measured at the edge of the plasma.

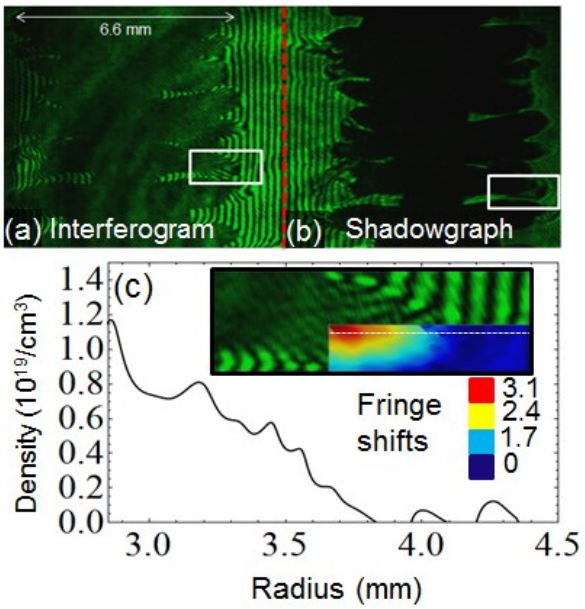

Figure 5.6 (reproduced). Shearing interferometry data for shot 817 (B_z = 0 T) using a simple air-wedge gap interferometer showing: (a) interferogram and, (b) shadowgraph. The boxed regions in (a) and (b) mark the same region of the plasma. (c) The electron density plotted as a function of radius for a sample lineout taken from the boxed region in (a). In (c), the boxed region is enlarged and the fringe shifts are superimposed on the interferogram.

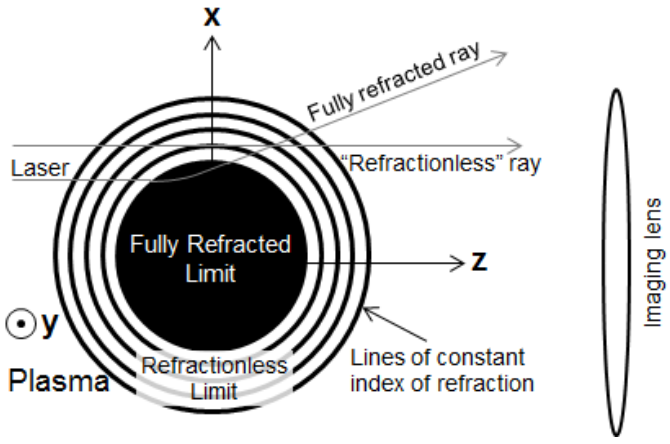

Figure C.1. Overview of interferometric analysis model. The plasma is separated into two distinct regions, (1) the fully refracted region, where laser light is fully refracted out of the imaging system (it may also be fully attenuated) and (2) the "refractionless" region, where laser light rays are assumed to undergo no refraction. The "refractionless" assumption enables the index of refraction inversion from interference fringes mathematically tractable.

BIBLIOGRAPHY

ATO16 L. Atoyan, D. A. Hammer, B. R. Kusse, T. Byvank, A. D. Cahill, J. B. Greenly, S. A. Pikuz, and T. A. Shelkovenko. “Helical plasma striations in liners in the presence of an external axial magnetic field”. *Physics of Plasmas* **23**, 022708 (2016).

AWE13 T. J. Awe, R. D. McBride, C. A. Jennings, D. C. Lamppa, M. R. Martin, D. C. Rovang, S. A. Slutz, M. E. Cuneo, A. C. Owen, D. B. Sinars, K. Tomlinson, M. R. Gomez, S. B. Hansen, M. C. Herrmann, J. L. McKenney, C. Nakhleh, G. K. Robertson, G. A. Rochau, M. E. Savage, D. G. Schroen, and W. A. Stygar. “Observations of Modified Three-Dimensional Instability Structure for Imploding z-Pinch Liners that are Premagnetized with an Axial Field”. *Physical Review Letters* **111**, 235005 (2013).

AWE14 T. J. Awe, C. A. Jennings, R. D. McBride, M. E. Cuneo, D. C. Lamppa, M. R. Martin, D. C. Rovang, D. B. Sinars, S. A. Slutz, A. C. Owen, K. Tomlinson, M. R. Gomez, S. B. Hansen, M. C. Herrmann, M. C. Jones, J. L. McKenney, G. K. Robertson, G. A. Rochau, M. E. Savage, D. G. Schroen, and W. A. Stygar. “Modifed helix-like instability structure on imploding z-pinch liners that are pre-imposed with a uniform axial magnetic field". *Physics of Plasmas* **21**, 056303 (2014).

BAI02 J. E. Bailey, G. A. Chandler, D. Cohen, M. E. Cuneo, M. E. Foord, R. F. Heeter, D. Jobe, P. W. Lake, J. J. MacFarlane, T. J. Nash, D. S. Nielson, R. Smelser, and J. Torres. “Radiation science using Z-pinch x rays”. *Physics of Plasmas* **9**, 2186 (2002).

BAI03 J. E. Bailey, P. Arnault, T. Blenski, G. Dejonghe, O. Peyrusse, J.J. MacFarlane, R.C. Mancini, M.E. Cuneo, D.S. Nielsen, and G.A. Rochau. “Opacity measurements of tamped NaBr samples heated by z-pinch X-rays". *Journal of Quantitative Spectroscopy and Radiative Transfer* 81.14 (2003).

BAI15 J. E. Bailey, T. Nagayama, G. P. Loisel, G. A. Rochau, C. Blancard, J. Colgan, Ph. Cosse, G. Faussurier, C. J. Fontes, F. Gilleron, I. Golovkin, S. B. Hansen, C. A. Iglesias, D. P. Kilcrease, J. J. MacFarlane, R. C. Mancini, S. N. Nahar, C. Orban, J.-C. Pain, A. K. Pradhan, M. Sherrill, and B. G. Wilson. "A higher-than-predicted measurement of iron opacity at solar interior temperatures", *Nature* **517**, 56-59 (2015).

BEL06 P. M. Bellan. *Fundamentals of Plasma Physics*. Cambridge, UK: Cambridge University Press, 2006.

BER14 G. Bertin, *Dynamics of Galaxies*, 2nd ed., Cambridge U. Press, New York (2014).

BIS58 S. Bishop, *Project Sherwood—The U.S. Program in Controlled Fusion*, Addison-Wesley Publishing Company, Reading, MA (1958).

BLE12 I. Blesener, B. Kusse, K. Blesener, J. Greenly, and D. Hammer. "Ablation and Precursor Formation in Copper Wire-Array and Liner Z-Pinches". *IEEE Transactions on Plasma Science* **40**, 3313–3318 (2012).

BUD90 A. B. Budko, M. A. Liberman, and A. L. Velikovich. "Suppression of Rayleigh-Taylor and bulk convective instabilities in imploding plasma liners and pinches". *Physics of Plasmas* **2,** 1159 (1990).

BUR15 G. C. Burdiak, S. V. Lebedev, F. Suzuki-Vidal, G. F. Swadling, S. N. Bland, N. Niasse, L. Suttle, M. Bennet, J. Hare, M. Weinwurm, R. Rodriguez, J. Gil and G. Espinosa. "Cylindrical liner Z-pinch experiments for fusion research and high-energy-density physics". *J. Plasma Physics*, **81**, 365810301 (2015).

BUR58 L. C. Burkhardt, R. H. Lovberg, G. A. Sawyer, and T. F. Stratton. "Stability Studies with Longitudinal Magnetic Field on a Straight Pinched Discharge". *Journal of Applied Physics* **29**, 964 (1958).

COM87 N. Comins and L. Marschall. "How do spiral galaxies spiral?". *Astronomy,* **15**, 7-23 (1987).

COV07 C. A. Coverdale, C. Deeney, A. L. Velikovich, R. W. Clark, Y. K. Chong, J. Davis, and J. Franklin. "Neutron production and implosion characteristics of a deuterium gas-puff Z pinch". *Physics of Plasmas* **14**, 022706 (2007).

CUN06 M. E. Cuneo, R. A. Vesey, G. R. Bennett, D. B. Sinars, W. A. Stygar, E. M. Waisman, J. L. Porter, P. K. Rambo, I. C. Smith, S. V. Lebedev, J. P. Chittenden, D. E. Bliss, T. J. Nash, G. A. Chandler, B. B. Afeyan, E. P. Yu, R. B. Campbell, R. G. Adams, D. L. Hanson, T. A. Mehlhorn, and M. K. Matzen, "Progress in Symmetric ICF Capsule Implosions and Wire-Array Z-Pinch Source Physics for Double-Pinch-Driven Hohlraums," *Plasma Physics and Controlled Fusion* **48**, R1 (2006).

CUN12 M. E. Cuneo, M. C. Herrmann, D. B. Sinars, S. A. Slutz, W. A. Stygar, R. A. Vesey, A. B. Sefkow, G. A. Rochau, G. A. Chandler, J. E. Bailey, J. L. Porter, R. D. McBride, D. C. Rovang, M. G. Mazarakis, E. P. Yu, D. C. Lamppa, K. J. Peterson, C. Nakhleh, S. B. Hansen, A. J. Lopez, M. E. Savage, C. A. Jennings, M. R. Martin, R. W. Lemke, B. W. Atherton, I. C. Smith, P. K. Rambo, M. Jones, M. R. Lopez, P. J. Christenson, M. A. Sweeney, B. Jones, L. A. McPherson, E. Harding, M. R. Gomez, P. F. Knapp, T. J. Awe, R. J. Leeper, C. L. Ruiz, G. W. Cooper, K. D. Hahn, J. McKenney, A. C. Owen, G. R. McKee, G. T. Leifeste, D. J. Ampleford, E. M. Waisman, A. Harvey-Thompson, R. J. Kaye, M. H. Hess, S. E. Rosenthal, and M. K. Matzen. "Magnetically Driven Implosions for Inertial Confinement Fusion at Sandia National Laboratories". *IEEE Transactions on Plasma Science* **40**, 3222 (2012).

CUR60 F. L. Curzon, A. Folkierski, R. Latham and J. A. Nation. "Experiments on the Growth Rate of Surface Instabilities in a Linear Pinched Discharge" *Proceedings of the Royal Society of London. Series A, Mathematical and Physical Sciences*, **257**, 1290 (1960).

FEY64 R. P. Feynman, *The Feynman Lectures on Physics*, Vol. 1, p. 7-7 (Addison-Wesley, 1964).

GIL09 R. M. Gilgenbach, M. R. Gomez, J. C. Zier, W. W. Tang, D. M. French, Y. Y. Lau, M. G. Mazarakis, M. E. Cuneo, M. D. Johnston, B. V. Oliver, T. A. Mehlhorn, A. A. Kim, and V. A. Sinebryukhov, *AIP Conference Proceedings* **1088**, 259 (2009).

GOM10 M. R. Gomez. "Experimental Examination of Plasma Formation and Current Loss in Post-Hole Convolutes". PhD thesis. University of Michigan, Ann Arbor, 2010.

GOM14 M. R. Gomez, S. A. Slutz, A. B. Sefkow , D. B. Sinars, K. D. Hahn, S. B. Hansen, E. C. Harding, P. F. Knapp, P. F. Schmit, C. A. Jennings, T. J. Awe, M. Geissel, D. C. Rovang, G. A. Chandler, G. W. Cooper, M. E. Cuneo, A. J. Harvey-Thompson, M. C. Herrmann, M. H. Hess, O. Johns, D. C. Lamppa, M. R. Martin, R. D. McBride, K. J. Peterson, J. L. Porter, G. K. Robertson, G. A. Rochau, C. L. Ruiz, M. E. Savage, I. C. Smith, W. A. Stygar, and R. A. Vesey. "Experimental Demonstration of Fusion-Relevant Conditions in Magnetized Liner Inertial Fusion". *Physical Review Letters* **113,** 155003 (2014).

GOM15 M. R. Gomez, S. A. Slutz, A. B. Sefkow, K. D. Hahn, S. B. Hansen, P. F. Knapp, C. A. Jennings. "Demonstration of thermonuclear conditions in magnetized liner inertial fusion experiments". *Physics of Plasmas* **22**, 056306 (2015).

HAR62 E. G. Harris. "Rayleigh Taylor Instabilities of a Collapsing Cylindrical Shell in a Magnetic Field". *Physics of Fluids* **5**, 1057 (1962).

HIP04 M. Hipp, J. Woisetschläger, P. Reiterer, and T.Neger. "Digital evaluation of interferograms", *Measurement* **36**, 53-66 (2004). See also: *www.optics.tugraz.at*

HUD65 R. H. Huddlestone and S. L. Leonard, *Plasma Diagnostic Techniques*, Academic Press, New York (1965).

INT04 T. Intrator, S. Y. Zhang, J. H. Degnan, I. Furno, C. Grabowski, S. C. Hsu, and W. J. Waganaar. "A high density field reversed configuration (FRC) target for magnetized target fusion: First internal profile measurements of a high density FRC". *Physics of Plasmas* **11**, 2580 (2004).

KIM09 A. A. Kim, M. G. Mazarakis, V. A. Sinebryukhov, B. M. Kovalchuk, V. A. Visir, S. N. Volkov, F. Bayol, A. N. Bastrikov, V. G. Durakov, S. V. Frolov, V. M. Alexeenko, D. H. McDaniel, W. E. Fowler, K. LeChien, C. Olson, W. A. Stygar, K. W. Struve, J. Porter, and R. M. Gilgenbach. "Development and tests of fast 1-MA linear transformer driver stages". *Physical Review ST Accelerators and Beams* **12**, 050402 (2009).

KIR95 R. C. Kirkpatrick, I. R. Lindemuth, and M. S. Ward. "Magnetized Target Fusion: An Overview" *Fusion Science and Technology* **27**, 201 (1995).

KON09 J. M. Koning, G. D. Kerbel, and M. M. Marinak, "The Hydra Magnetohydrodynamics Package". APS-DPP (2009).

LAU11 Y. Y. Lau, J. C. Zier, I. M. Rittersdorf, M. R. Weis, and R. M. Gilgenbach. “Anisotropy and feedthrough in magneto-Rayleigh-Taylor instability". *Physical Review E* **83**, 066405 (2011).

LAU76 Y. Y. Lau, C. C. Lin, and J. W.- K. Mark, “Unstable spiral modes in disk-shaped galaxies,” Proc. Nat. Acad. Sci. U. S. A.**73**, 1379 (1976).

LAU78 Y. Y. Lau and G. Bertin, "Discrete spiral modes, spiral waves, and the local dispersion relationship," Astrophys. J. **226**, 508 (1978).

LEB01 S. V. Lebedev, F. N. Beg, S. N. Bland, J. P. Chittenden, A. E. Dangor, M. G. Haines, K. H. Kwek, S. A. Pikuz, and T. A. Shelkovenko. “Effect of discrete wires on the implosion dynamics of wire array Z pinches”. *Physics of Plasmas* **8**, 3734 (2001).

LIN64 C. C. Lin and F. H. Shu, “On the spiral structures of disk galaxies,” Astrophys. J. **140**, 646 (1964).

MAR01 M. M. Marinak, G.Kerbel, N. Gentile, O. Jones, D. Munro, S. Pollaine, T. R. Dittrich, and S. W. Haan. “Three-dimensional HYDRA simulations of National Ignition Facility targets”. *Physics of Plasmas* **8**, 2275 (2001).

MAT65 J. W. Mather. “Formation of a High-Density Deuterium Plasma Focus”. *Physics of Fluids* **8**, 366 (1965).

MAT97 M. K. Matzen. "Z pinches as intense x-ray sources for high-energy density physics applications”. *Physics of Plasmas* **4**, 1519 (1997).

MAZ10 M. G. Mazarakis, W. E. Fowler, K. L. LeChien, F. W. Long, M. K. Matzen, D. H. McDaniel, R. G. McKee, C. L. Olson, J. L. Porter, S. T. Rogowski, K. W. Struve, W. A. Stygar, J. R. Woodworth, A. A. Kim, V. A. Sinebryukhov, R. M. Gilgenbach, M. R. Gomez, D. M. French, Y. Y. Lau, J. C. Zier, D. M. VanDevalde, R. A. Sharpe, and K. Ward. “High-Current Linear Transformer Driver Development at Sandia National Laboratories”. *IEEE Transactions on Plasma Science* **38**, 704 (2010).

MCB12 R. D. McBride, S. A. Slutz, C. A. Jennings, D. B. Sinars, M. E. Cuneo, M. C. Herrmann, R. W. Lemke, M. R. Martin, R. A. Vesey, K. J. Peterson, A. B. Sefkow, C. Nakhleh, B. E. Blue, K. Killebrew, D. Schroen, T. J. Rogers, A. Laspe, M. R. Lopez, I. C. Smith, B. W. Atherton, M. Savage, W. A. Stygar, and J. L. Porter. “Penetrating Radiography of Imploding and Stagnating Beryllium Liners on the Z Accelerator". *Physical Review Letters* **109**, 135004 (2012).

MCB13 R. D. McBride, M. R. Martin, R. W. Lemke, J. B. Greenly, C. A. Jennings, D. C. Rovang, D. B. Sinars, M. E. Cuneo, M. C. Herrmann, S. A. Slutz, C. W. Nakhleh, D. D. Ryutov, J.-P. Davis, D. G. Flicker, B. E. Blue, K. Tomlinson, D. Schroen, R. M. Stamm, G. E. Smith, J. K. Moore, T. J. Rogers, G. K. Robertson, R. J. Kamm, I. C. Smith, M. Savage, W. A. Stygar, G. A. Rochau, M. Jones, M. R. Lopez, J. L. Porter and M. K. Matzen. “Beryllium liner implosion experiments on the Z accelerator in preparation for magnetized liner inertial fusion”. *Physics of Plasmas* **20**, 056309 (2013).

ORE08 V. I. Oreshkin. “Thermal instability during an electrical wire explosion". *Physics of Plasmas* **15**, 092103 (2008).

PET12 Kyle J. Peterson, Daniel B. Sinars, Edmund P. Yu, Mark C. Herrmann, Michael E. Cuneo, Stephen A. Slutz, Ian C. Smith, Briggs W. Atherton, Marcus D. Knudson, and Charles Nakhleh. “Electrothermal instability growth in magnetically driven pulsed power liners". *Physics of Plasmas* **19**, 092701 (2012).

PET13 Kyle J. Peterson, Edmund P. Yu, Daniel B. Sinars, Michael E. Cuneo, Stephen A. Slutz, Joseph M. Koning, Michael M. Marinak, Charles Nakhleh, and Mark C. Herrmann. “Simulations of electrothermal instability growth in solid aluminum rods". *Physics of Plasmas* **20**, 056305 (2013).

PET14 Kyle J. Peterson, Thomas J. Awe, Edmund P. Yu, Daniel B. Sinars, Ella S. Field, Michael E. Cuneo, Mark C. Herrmann, Mark Savage, Diana chroen Kurt Tomlinson, and Charles Nakhleh. “Electrothermal Instability Mitigation by Using Thick Dielectric Coatings on Magnetically Imploded Conductors". *Physical Review Letters* **112**, 135002 (2014).

PIK01 S. A. Pikuz, V. M. Romanova, N. V. Baryshnikov, Min Hu, B. R. Kusse, D. B. Sinars, T. A. Shelkovenko, and D. A. Hammer. “A simple air wedge shearing interferometer for studying exploding wires”. *Review of Scientific Instruments* **72,** 1098 (2001).

ROU08 A. G. Rousskikh, V. I. Oreshkin, S. A. Chaikovsky, N. A. Labetskaya, A. V. Shishlov, I. I. Beilis, and R. B. Baksht. “Study of the strata formation during the explosion of a wire in vacuum”. *Physics of Plasmas* **15**, 102706 (2008).

ROV14 D. C. Rovang, D. C. Lamppa, M. E. Cuneo, A. C. Owen, J. McKenney, D. W. Johnson, S. Radovich, R. J. Kaye, R. D. McBride, C. S. Alexander, T. J. Awe, S. A. Slutz, A. B. Sefkow, T. A. Haill, P. A. Jones, J. W. Argo, D. G. Dalton, G. K. Robertson, E. M. Waisman, D. B. Sinars, J. Meissner, M. Milhous, D. N. Nguyen, and C. H. Mielke. "Pulsed-coil magnet systems for applying uniform 10–30 T fields to centimeter-scale targets on Sandia's Z facility". *Review of Scientific Instruments* **85**, 124701 (2014).

RYU00 D. D. Ryutov, M. S. Derzon, and M. K. Matzen. "The physics of fast Z pinches". *Rev. Mod. Phys.* **72** (2000).

SAF16 A. S. Safronova , V. L. Kantsyrev , M. E. Weller , V. V. Shlyaptseva , I. K. Shrestha , M. Y. Lorance , M. T. Schmidt-Petersen , A. Stafford , M. C. Cooper , A. M. Steiner , D. A. Yager-Elorriaga , S. G. Patel , N. M. Jordan, R. M. Gilgenbach , and A. S. Chuvatin. "Double and Single Planar Wire Arrays on University-Scale Low-Impedance LTD Generator". *IEEE Trans. Plasma Sci*. **44**, 432 (2016).

SAN96 T. W. L. Sanford, G. O. Allshouse, B. M. Marder, T. J. Nash, R. C. Mock, R. B. Spielman, J. F. Seamen, J. S. McGurn, D. Jobe, T. L. Gilliland, M. Vargas, K. W. Struve, W. A. Stygar, M. R. Douglas, M. K. Matzen, J. H. Hammer, J. S. De Groot, J. L. Eddleman, D. L. Peterson, D. Mosher, K. G. Whitney, J. W. Thornhill, P. E. Pulsifer, J. P. Apruzese, and Y. Maron. "Improved Symmetry Greatly Increases X-Ray Power from Wire-Array Z-Pinches". *Physical Review Letters* **77**, 5063 (1996).

SCH12 A. Schmidt, V. Tang, and D. Welch. "Fully Kinetic Simulations of Dense Plasma Focus Z-Pinch Devices". *Physical Review Letters* **109**, 205003 (2012).

SCH16 P. F. Schmit, A. L. Velikovich, R. D. McBride, and G. K. Robertson. "Controlling Rayleigh-Taylor Instabilities in Magnetically Driven Solid Metal Shells by Means of a Dynamic Screw Pinch". *Physical Review Letters* **117**, 205001 (2016).

SES17 SESAME database: http://www.lanl.gov/org/padste/adtsc/theoretical/physics-chemistry-materials/sesame-database.php

SEY11 C. E. Seyler and M. R. Martin. "Relaxation model for extended magnetohydrodynamics: Comparison to magnetohydrodynamics for dense Z-pinches". *Physics of Plasmas* **18**, 012703 (2011).

SHL14 V. V. Shlyaptseva, V. L. Kantsyrev, A. S. Safronova, A. A. Esaulov, I. Shrestha, M. E. Weller, G. C. Osborne, and S. F. Keim. “Gold planar wire array radiation sources at university scale generators and their applications”. *Int. J. Mod. Phys.: Conf. Ser.* **32**, 1460324 (2014).

SHU82 F. H. Shu, *The Physical Universe—An Introduction to Astronomy*, University Science Book, Mill valley, CA, (1982), p. 274.

SIL04 W. T. Silfvast, *Laser Fundamentals*, 2nd ed., Cambridge U. Press, Cambridge, UK (2004).

SIN10 D. B. Sinars, S. A. Slutz, M. C. Herrmann, R. D. McBride, M. E. Cuneo, K. J. Peterson, R. A. Vesey, C. Nakhleh, B. E. Blue, K. Killebrew, D. Schroen, K. Tomlinson, A. D. Edens, M. R. Lopez, I. C. Smith, J. Shores, V. Bigman, G. R. Bennett, B. W. Atherton, M. Savage, W. A. Stygar, G. T. Leifeste, and J. L. Porter. “Measurements of Magneto-Rayleigh-Taylor Instability Growth during the Implosion of Initially Solid Al Tubes Driven by the 20-MA, 100-ns Z Facility". *Physical Review Letters* **105**, 185001 (2010).

SIN11 D. B. Sinars, S. A. Slutz, M. C. Herrmann, R. D. McBride, M. E. Cuneo, C. A. Jennings, J. P. Chittenden, A. L. Velikovich, K. J. Peterson, R. A. Vesey, C. Nakhleh, E. M. Waisman, B. E. Blue, K. Killebrew, D. Schroen, K. Tomlinson, A. D. Edens, M. R. Lopez, I. C. Smith, J. Shores, V. Bigman, G. R. Bennett, B. W. Atherton, M. Savage, W. A. Stygar, G. T. Leifeste, and J. L. Porter. “Measurements of magneto-Rayleigh-Taylor instability growth during the implosion of initially solid metal liners”. *Physics of Plasmas* **18**, 056301 (2011).

SLU10 S. A. Slutz, M. C. Herrmann, R. A. Vesey, A. B. Sefkow, D. B. Sinars, D. C. Rovang, K. J. Peterson, and M. E. Cuneo. “Pulsed-power-driven cylindrical liner implosions of laser preheated fuel magnetized with an axial field". *Physics of Plasmas* **17**, 056303 (2010).

SPI85 R. B. Spielman, D. L., Hanson, M. A. Palmer, M. K. Matzen, T. W. Hussey, and J. M. Peek. “Efficient x-ray production from ultrafast gas-puff Z pinches”. *Journal of applied physics* **57**, 830 (1985).

SPI88 R. B. Spielman, C. Deeney, G. A. Chandler, M. R. Douglas, D. L. Fehl, M. K. Matzen, and J. F. Seamen. “Tungsten wire-array Z-pinch experiments at 200 TW and 2 MJ”. *Physics of Plasmas* **5**, 2105 (1998).

STE16 A. M. Steiner, “The Electrothermal Instability on Pulsed Power Ablations of Thin Foils”. PhD thesis. University of Michigan, Ann Arbor, 2016.

STY07 W. A. Stygar, M. E. Cuneo, D. I. Headley, H. C. Ives, R. J. Leeper, M. G. Mazarakis, C. L. Olson, J. L. Porter, T. C. Wagoner, and J. R. Woodworth. "Architecture of petawatt-class **z**-pinch accelerators" *Physical Review Accelerators and Beams* **10**, 030401 (2007).

STY15 W. A. Stygar, T. J. Awe, J. E. Bailey, N. L. Bennett, E.W. Breden, E. M. Campbell, R. E. Clark, R. A. Cooper, M. E. Cuneo, J. B. Ennis, D. L. Fehl, T. C. Genoni, M. R. Gomez, G.W. Greiser, F. R. Gruner, M. C. Herrmann, B. T. Hutsel, C. A. Jennings, D. O. Jobe, B. M. Jones, M. C. Jones, P. A. Jones, P. F. Knapp, J. S. Lash, K. R. LeChien, J. J. Leckbee, R. J. Leeper, S. A. Lewis, F.W. Long, D. J. Lucero, E. A. Madrid, M. R. Martin, M. K. Matzen, M. G. Mazarakis, R. D. McBride, G. R. McKee, C. L. Miller, J. K. Moore, C. B. Mostrom, T. D. Mulville, K. J. Peterson, J. L. Porter, D. B. Reisman, G. A. Rochau, G. E. Rochau, D. V. Rose, D. C. Rovang, M. E. Savage, M. E. Sceiford, P. F. Schmit, R. F. Schneider, J. Schwarz, A. B. Sefkow, D. B. Sinars, S. A. Slutz, R. B. Spielman, B. S. Stoltzfus, C. Thoma, R. A. Vesey, P. E. Wakeland, D. R. Welch, M. L. Wisher, and J. R. Woodworth. "Conceptual designs of two petawatt-class pulsed-power accelerators for high-energy-density-physics experiments". *Physical Review Accelerators and Beams* **18**, 110401 (2015).

SYP16 A. M. Steiner, D. A. Yager-Elorriaga, S. G. Patel, N. M. Jordan, R. M. Gilgenbach, A. S. Safronova, V. L. Kantsyrev, V. V. Shlyaptseva, I. Shrestha, and M. T. Schmidt-Petersen. "Determination of plasma pinch time and effective current radius of double planar wire array implosions from current measurements on a 1-MA linear transformer driver". *Physics of Plasmas* **23**, 101206 (2016).

VAL14 J. C. Valenzuela, G. W. Collins IV, D. Mariscal, E. S. Wyndham, and F. N. Beg. "Study of instability formation and EUV emission in thin liners driven with a compact 250 kA, 150 ns linear transformer driver". *Phys. Plasmas* **21**, 031208 (2014).

VES79 C. M. Vest, *Holographic Interferometry*, John Wiley & Sons, New York (1979).

WEI14 M. R. Weis, P. Zhang, Y. Y. Lau, I. M. Rittersdorf, J. C. Zier, R. M. Gilgenbach, M. H. Hess, and K. J. Peterson. "Temporal evolution of surface ripples on a finite plasma slab subject to the magneto-Rayleigh-Taylor instability". *Physics of Plasmas* **21**, 122708 (2014).

WEI15 M. R. Weis, "Magneto-Rayleigh-Taylor Instability: theory and simulation in planar and cylindrical pulsed power targets". PhD thesis, University of Michigan, Ann Arbor (2015).

WZL15 M. R. Weis, P. Zhang, Y. Y. Lau, P. F. Schmit, K. J. Peterson, M. Hess, and R. M. Gilgenbach. “Coupling of sausage, kink, and magneto-Rayleigh-Taylor instabilities in a cylindrical liner". *Physics of Plasmas* **22**, 032706 (2015).

YAG15 D. A. Yager-Elorriaga, A. M. Steiner, S. G. Patel, N. M. Jordan, Y. Y. Lau and R. M. Gilgenbach. “Technique for fabrication of ultrathin foils in cylindrical geometry for liner-plasma implosion experiments with sub-megaampere currents”, *Review of Scientific Instruments*, **86**, 113506 (2015).

YAG16a D. A. Yager-Elorriaga, P. Zhang, A.M. Steiner, N.M. Jordan, Y.Y. Lau, and R.M. Gilgenbach, “Seeded and unseeded helical modes in magnetized, non-imploding cylindrical liner-plasmas”. *Physics of Plasmas* **23**, 101205 (2016).

YAG16b D. A. Yager-Elorriaga, P. Zhang, A. M. Steiner, N. M. Jordan, P. C. Campbell, Y. Y. Lau, and R. M. Gilgenbach. “Discrete helical modes in imploding and exploding cylindrical, magnetized liners”. *Physics of Plasmas* **23**, 124502 (2016).

ZIE10 J. C. Zier. “Ablation Dynamics and Instabilities of Metallic Plasmas Generated Using Mega-ampere-scale Current Drivers”. PhD thesis. University of Michigan, Ann Arbor, 2010.

ZIE12 J. C. Zier, R. M. Gilgenbach, D. A. Chalenski, Y. Y. Lau, D. M. French, M. R. Gomez, S. G. Patel, I. M. Rittersdorf, A. M. Steiner, M. Weis, P. Zhang, M. Mazarakis, M. E. Cuneo, and M. Lopez. “Magneto-Rayleigh-Taylor experiments on a MegaAmpere linear transformer driver". *Physics of Plasmas* **19**, 032701 (2012).